



University of Kerbala

College of Science

Department of Chemistry

**Preparation and Characterization of $\text{MoFe}_2\text{O}_4 / \text{Al}_2\text{O}_3$
Nanocomposites for Photocatalytic of Indigo Carmine Dye**

A Thesis

Submitted to the Council of the College of Science/University of Kerbala

**as a Partial Fulfillment of the Requirements for the Degree of Master of
Science in Chemistry**

By

Mohammed Ali Hameed

B.Sc. in Chemistry (2013) / Wasit University

Supervised by

Prof. Dr. Luma Majeed Ahmed

2024 AD/ 1

1445 AH

بِسْمِ اللَّهِ الرَّحْمَنِ الرَّحِيمِ

﴿ يَا أَيُّهَا الَّذِينَ آمَنُوا إِذَا قِيلَ لَكُمْ تَفَسَّحُوا فِي
الْمَجَالِسِ فَافْسَحُوا يَفْسَحِ اللَّهُ لَكُمْ ۗ وَإِذَا قِيلَ
انشُرُوا فَانشُرُوا يَرْفَعِ اللَّهُ الَّذِينَ آمَنُوا مِنْكُمْ
وَالَّذِينَ أُوتُوا الْعِلْمَ دَرَجَاتٍ ۗ وَاللَّهُ بِمَا تَعْمَلُونَ
خَبِيرٌ ﴾

صدق الله العظيم

سورة المجادلة الآية 11

Dedication

To my father's and brother's souls (may God have mercy on them)

To my mother, may Allah protect her

To my beloved wife, and children

To all friends and lovers

To my supervisor

To all science students

I dedicate this study

Mohammed

Acknowledgments

Initially, I want to thank the almighty Allah for giving me strength and guidance throughout my entire life and during this work in particular.

I would like to deliver my deepest gratitude to my supervisor,

Prof. Dr. Luma Majeed Ahmed, for her dedication, encouragement, and outstanding scientific support during the whole work.


Also, I want to thank all faculty members of the Department of Chemistry in the College of Science at the University of Kerbala, for their worthless support of the work.

Finally, I thank my wife, who was the main supporter in completing my scientific career, as well as everyone who supported me even with a word

Mohammed

Supervisor Certification

I certify that this thesis was prepared by **Mohammed Ali Hameed** my supervision at the Chemistry Department, College of Science, University Karbala, as a partial requirement for the degree of Master of Science in Chemistry.

Signature: 

Name: **Dr. Luma M. Ahmed**

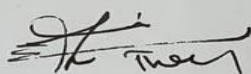
Title: **Professor**

Date: / / 2024

Report of the Head of Chemistry Department

According to the recommendation presented by the Chairman of the Postgraduate Studies Committee, I forward this thesis for discussion.

Signature:



Head of Chemistry Department: **Prof. Dr. Thaer Mahdi Madlool Al-Rammahi**

Address: **University of Kerbala / College of Science**

Date: **4 / 1 / 2024**



Kerbala University
Science College




Asst. Prof. Dr. Thaer M. M. Al-Rammahi
Head of Chemistry Department

Examination Committee Certification

We, the examining committee, certify that we have read this thesis "Preparation and Characterization of $\text{MoFe}_2\text{O}_4/\text{Al}_2\text{O}_3$ Nanocomposites for photocatalytic of Indigo Carmine Dye" and examined the student (Mohammed Ali Hameed) in its contents and that in our opinion, it is adequate as a thesis for the degree MSc. of science in chemistry.

(Chairman)

Signature: 


Name: Dr. Eman Talib Kareem

Title: Professor

Address: University of Kerbala / College of Science

Date: / / 2024

(Member)

Signature: 

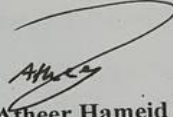
Name: Dr. Hazim Yahya Mohammed Ali

Title: Professor

Address: University of Babylon / College of Science for Women

Date: / / 2024

(Member)

Signature: 

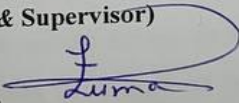
Name: Dr. Atheer Hameid Odda

Title: Assist. Professor

Address: University of Kerbala / college of medicine

Date: / / 2024

(Member & Supervisor)

Signature: 

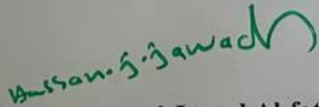
Name: Dr. Luma Majeed Ahmed

Title: Professor

Address: University of Kerbala / College of Science

Date: / / 2024

Approved by the council of the College of Science in its session No. in / / 2024

Signature: 

Name: Dr. Hassan Jameel Jawad Al-fatlawy

Title: Professor

Address: University of Kerbala - Dean of College of Science

Date: / / 2024

Abstract

This work consists of three main parts: **The first part** illustrates the synthesis of spinel Molybdenum Ferrite (MoFe_2O_4) nanoparticles, *via* the hydrothermal method using two types of surfactant: anionic is sodium dodecyl sulfate (SDS) and cationic is cetramide (CT) as a template and stabilizer. The Molybdenum Ferrite -Alumina ($\text{MoFe}_2\text{O}_4/\text{Al}_2\text{O}_3$) nanocomposites, was prepared by incorporating the spinel MoFe_2O_4 with synthesis Al_2O_3 by ultrasonic waves technique, which is a simple, fast, environmentally beneficial technique.

Part two includes the characterization of the prepared MoFe_2O_4 , synthesis Al_2O_3 , and their nanocomposites, using the techniques of FT-IR, XRD and SEM-EDX. The FT-IR spectra showed the tetrahedral and octahedral locations of molybdenum, and iron for all the catalysts prepared. The XRD analysis confirmed the spinel MoFe_2O_4 , synthesis Al_2O_3 , and their nanocomposites are successfully prepared with nano-sizes. The mean crystal size for synthesis MoFe_2O_4 catalysts increase after incorporating with Al_2O_3 . SEM analysis indicated the shape of prepared spinel MoFe_2O_4 in the presence of anionic SDS-surfactant, which found to be like-caviar, and its composite with Al_2O_3 is like-grains, while the shape of the spinel MoFe_2O_4 in the presence of cationic CT -surfactant and its composite with alumina are nanoplate and like-Popcorn nanoparticles, respectively. The shape of Al_2O_3 is occurred like-brain cells. Based on EDX spectra, the elements Fe, Mo, Al, and O demonstrate. The band-gaps (Bg) determined using Tauc equation, the Bg ranges of all samples are proved their photocatalysts with ranged 2.78 eV to 4.44 eV.

The pH of point of zero charge (pH_{zpc}) was determined for all samples using titration method under purged nitrogen, and found the ranged from 1.6 to 5.9. The pH_{zpc} range of synthesis MoFe_2O_4 catalysts elevate after synthesis of

composites. The quantum yields (Φ) of de-colorization IC dye with studied photocatalysts are found less than 1.

Part three focuses on the ability and evaluates the effectiveness of the MoFe_2O_4 , Al_2O_3 , and its nanocomposites on the de-colorization of indigo carmine IC dye. The effect of various factors on the photo decolorization of indigo carmine IC dye utilizing photocatalysts in the presence of SDS and CT surfactants were illustrated. Temperature and initial pH are two of these parameters. The best initial pH is occurred equal to 5.3.

The thermodynamic parameters were calculated using the Eyring-Polanyi equation, the equation of Arrhenius, and the Gibbs equation. The photoreactions with using MoFe_2O_4 in presence CT-surfactant and its composite are an exothermic, spontaneous reaction and less random. On the contrary, the photoreactions with using MoFe_2O_4 in presence SDS-surfactant is endothermic more random and nonspontinuous, and its composite are an exothermic, spontaneous reaction and less .

Table of Contents

Contents		Page
Abstract		II
Contents		III
List of Tables		V
List of Figures		IX
List of Abbreviations and Symbols		XIII
CHAPTER ONE : INTRODUCTION		
1.1.	General Introduction	1
1.2.	Advanced Oxidation Process (AOPs)	2
1.3.	Semiconductors and Synthesized Nanophotocatalysts	3
1.4.	The Synthesized Spinal (MoFe_2O_4) Nanophotocatalyst	6
1.5.	Synthises Al_2O_3 as photocatalysts	8
1.6.	Surfactants	10
1.7.	The Effect of Surfactant Type	12
1.7.1.	Anionic Surfactant as a Sodium Dodecyl Sulfate (SDS)	12
1.7.2.	Cationic Surfactant as a Cetrimide (CT)	13
1.8.	Dyes	14
1.8.1.	Indigo Carmine (IC)	14
1.9.	Photocatalytic Decolorization of Dyes	16
1.10.	Literature Review	18
1.11.	The Aim of The Work	20

CHAPTER TWO: EXPERIMENTAL		
2.1.	Chemicals	26
2.2.	Instruments	28
2.3.	Set of Synthesized Nanophotocatalyst Reactors	29
2.4.	Synthesis of MoFe ₂ O ₄ nanoparticles in the presence of surfactants	29
2.5.	Synthesis of Nanocomposites	31
2.6.	Characterization of Synthesized Nanophotocatalyst	33
2.6.1.	FT-IR Spectral Analysis	33
2.6.2.	XRD Analysis	33
2.6.3.	High Resolution-Scanning Electron Microscopy (HR-SEM) Studies	34
2.6.4.	Energy Dispersive X-ray (EDX) Analysis	34
2.6.5.	Bandgap Energy Measurements	34
2.7.	Determination of zero Point charge (pH _{zpc})	35
2.8.	The calibration curve of Indigo Carmine IC dye	36
2.9.	Photocatalytic de-colorization reaction of Indigo Carmine IC dye	37
2.10.	Light Intensity Measurements	39
2.11.	Activation Energy	40
2.12.	Thermodynamic Parameters	40
2.13.	The quantum yield	41
CHAPTER THREE: RESULTS AND DISCUSSION		
3.1.	Synthesis of synthesized Nanometrials	
3.2.	Characterization Synthesized Nanophotocatalysts	42

3.2.1.	The (FT-IR) Spectra of Synthesized Nanophotocatalysts	42
3.2.2.	X-ray diffraction Patterns (XRD) analysis	47
3.2.3.	SEM Analysis	50
3.2.4.	EDX Analysis	54
3.2.5.	Measurement of Band Gap Energy	56
3.2.6.	The pH Point of zero charge(pH_{zpc})	57
3.3.	Photocatalytic Reaction of Indigo Carmine IC dye	58
3.3.1.	Effect of Parameters on Photocatalytic Reaction of Decolorization of Indigo Carmine IC Dye	59
3.3.1.1.	The effect of nanophotocatalyst doses	60
3.3.1.2.	Effect of Initial pH	61
3.3.1.3.	Effect of Temperature	72
3.4.	Quantum Yield of Photo-decolorization of Indigo Carmine (IC)	87
3.5.	Suggested Decolorization Mechanism of Indigo Carmine (IC)	88
3.6.	Conclusion	91
3.7.	Future Works	92
3.8.	References	94

<i>No.</i>	<i>List of Tables</i>	<i>Page</i>
1.1	Physiochemical properties of MoFe ₂ O ₄ Crystals	7
1.2	Physiochemical properties of synthesised Al ₂ O ₃ Crystals	10
1.3	The classified of surfactants with common used and examples	11
2.1	Sources and purities of the used chemicals	26
2.2	Instruments and tools, company and places that are used in this study	27
2.3	Indigo Carmine IC dye calibration curve data	36
3.2	FT-IR spectra are used to assign bands and their corresponding wavenumbers	46
3.2	Estimation of the p <i>H</i> _{pzc} for MoFe ₂ O ₄ Nanoparticles and their Nanocomposites in Presence of CT or SDS-Surfactant, Using Simplified "Titration Method"	59
3.3	The change of the ln(C ₀ /C _t) with irradiation time at pH of Indigo Carmine IC Dye by MoFe ₂ O ₄ with the Presence of the CT-Surfactant	62
3.4	The Variation of (PDE%) with Times Irradiation at Different Initial pH of Indigo Carmine IC Dye by MoFe ₂ O ₄ with the Presence the CT-Surfactant	63
3.5	(a) ln(C ₀ /C _t) Varying with Times Irradiation at Various Initial pH of Indigo Carmine IC dye by Synthesis Al ₂ O ₃	64
3.6	The Variation of ln (PDE%) with Times Irradiation at Different Initial pH of Indigo Carmine IC dye by Synthesis Al ₂ O ₃	65
3.7	The change of the ln(C ₀ /C _t) with irradiation time at pH of Indigo Carmine IC Dye by Nanocomposites with the Presence of the CT-Surfactant	66
3.8	The Variation of (PDE%) with Times Irradiation at Different Initial pH of Indigo Carmine IC Dye by Nanocomposites with the Presence of the CT-Surfactant	67

3.9	(a) $\ln(C_0/C_t)$ Varying with Times Irradiation at Various Initial pH of Indigo Carmine IC Dye by MoFe_2O_4 with the Presence of the SDS-Surfactant	69
3.10	The Variation of (PDE%) with Times Irradiation at Different Initial pH of Indigo Carmine IC Dye by MoFe_2O_4 with the Presence of the SDS-Surfactant	70
3.11	The change of the $\ln(C_0/C_t)$ with irradiation time at pH of Indigo Carmine IC dye by Nanocomposites with the Presence of the SDS-Surfactant	71
3.12	The Variation of (PDE%) with Times Irradiation at Different Initial pH of Indigo Carmine IC dye by Nanocomposites with the presence of the SDS-Surfactant	72
3.13	Activation Energies and Thermodynamic Functions for Decolorizing Indigo Carmine IC Dye calculate the Spinal MoFe_2O_4 in the Presence of CT-Surfactant, Al_2O_3 Synthesis, and Nanocomposites.	73
3.14	The change of the $\ln(C_0/C_t)$ with irradiation time at temperatures of Spinal MoFe_2O_4 with the Presence of the CT-Surfactant <i>Via</i> Synthesized Nanophotocatalyst De-colorization of Indigo Carmine Dye	75
3.15	The Variation of (PDE%) with Times Irradiation at Different Temperatures of Spinal MoFe_2O_4 with the Presence of the CT-Surfactant <i>Via</i> Synthesized Nanophotocatalyst De-colorization of Indigo Carmine IC Dye	75
3.16	The $\ln(C_0/C_t)$ Variation with Times Irradiation at Various Temperatures of Synthesis Al_2O_3 <i>Via</i> Synthesized Nanophotocatalyst De-colorization of Indigo Carmine Dye	77
3.17	The Variation of (PDE%) with Times Irradiation at Different Temperatures of Synthesis Al_2O_3 <i>Via</i> Synthesized Nanophotocatalyst De-colorization of Indigo Carmine IC dye	78
3.18	The change of the $\ln(C_0/C_t)$ with irradiation time at temperatures of Nanocomposites with the Presence of CT-Surfactant <i>Via</i> Synthesized Nanophotocatalyst De-colorization of Indigo Carmine Dye	80

3.19	The Variation of (PDE%) with Times Irradiation at Different Temperatures of Nanocomposites with the Presence of the CT-Surfactant <i>Via</i> Synthesized Nanophotocatalyst De-colorization of Indigo Carmine IC Dye	80
3.20	Calculated the Spinal MoFe_2O_4 in the Presence of SDS-Surfactant, Al_2O_3 Synthesis, and Nanocomposites , Activation Energies and Thermodynamic Functions for Decolorizing Indigo Carmine IC Dye	82
3.21	The change of the $\ln(\text{Co}/\text{Ct})$ with irradiation time at temperatures of Spinal MoFe_2O_4 with the Presence of the SDS-Surfactant <i>Via</i> Synthesized Nanophotocatalyst De-colorization of Indigo Carmine Dye	83
3.22	The Variation of (PDE%) with Times Irradiation at Different Temperatures of Spinal MoFe_2O_4 with the Presence of the SDS-Surfactant <i>Via</i> Photocatalytic De-colorization of Indigo Carmine IC Dye	84
3.23	The change of the $\ln(\text{Co}/\text{Ct})$ with irradiation time at temperatures Nanocomposites with the Presence of the SDS-Surfactant <i>Via</i> Photocatalytic De-colorization of Indigo Carmine Dye	85
3.24	The Variation of (PDE%) with Times Irradiation at Different Temperatures of Nanocomposites in the Presence of SDS-Surfactant by Photocatalytic De-colorization of Indigo Carmine IC Dye	86
3.25	Values Quantum Yields of all Synthesized Nanophotocatalyst for Decolorization Indigo Carmine IC Dye	88

<i>No.</i>	<i>List of Figures</i>	<i>Page</i>
1.1	Schematic diagram of the most applications for advanced oxidation processes as a ·OH source	2
1.2	Schematic illustration of the main reactions taking place on a bulk or a nano photosemiconductor under light irradiation	4
1.3	Photocatalytic mechanism using a photosemiconductor b) Types of recombination Processes	5
1.4	Crystal structure of spinel-type oxide consisting of tetrahedral (T_d) A and octahedral (O_h) B	6
1.5	The 3D molecular structure of Alumina	9
1.7.1	Chemical structure of sodium dodecyl sulfate (SDS)	13
1.7.2	Chemical Structure of Cetrimide (CT)	13
1.8	Diagram depicts the degradation mechanism of dye on the catalyst's surface	17
2.1	Homemade photo reactor contents from the wooden box (1), High-pressure mercury lamp(400W) (2), vacuum fan (3) 500 cm ³ Pyrex glass beaker (4), Teflon bar (5), and magnetic stirrer (6)	29
2.2	Schematic digram of Molybdenum Ferrite nanoparticles synthesis in presence positive and negative surfactant by hydrothermal method	31
2.3	Schematic diagram for the Nanocomposites Synthesis steps	33
2.5	Schematic digram for steps of determining the point of zero charge of Synthesized Nanophotocatalyst samples	35
2.6	(a) Spectrum of UV-visible absorption for IC dye (b) Calibration curve of Indigo Carmine at various dye concentrations at 1-50 ppm	37
3.1	FT-IR spectrum of the spinal $MoFe_2O_4$ Nanoparticles in presence the SDS-	43

	Surfactant	
3.2	FT-IR spectrum of Al ₂ O ₃ synthesis	44
3.3	FT-IR spectrum of Nanocomposites in presence the SDS-Surfactant	44
3.4	FT-IR Spectrum of Inverse Spinal MoFe ₂ O ₄ Nanoparticles in the Presence of CT-Surfactant	45
3.5	FT-IR spectrum of Nanocomposites in presence the CT-Surfactant	46
3.6	XRD pattern of (a) MoFe ₂ O ₄ (b) Al ₂ O ₃ (c) Nanocomposites prepared in presence the SDS-Surfactant	48
3.7	XRD pattern of (a) MoFe ₂ O ₄ (b) Al ₂ O ₃ (c) Nanocomposites prepared in presence the CT-Surfactant	50
3.8	SEM Images of MoFe ₂ O ₄ nanoparticles in presence the SDS-Surfactant	51
3.9	SEM Images of synthesis Al ₂ O ₃	51
3.10	SEM Images of Nanocomposites in presence the SDS-Surfactant	52
3.11	SEM images of a) MoFe ₂ O ₄ Nanoparticles b) Nanocomposites in presence the CT-Surfactant	53
3.12	EDX spectra of (a) MoFe ₂ O ₄ Nanoparticles, (b) Al ₂ O ₃ and (c) Nanocomposites with presence the SDS-surfactant	55
3.13	EDX Spectra of (a) MoFe ₂ O ₄ Nanoparticles, (b) Al ₂ O ₃ and (c) Nanocomposites with the Presence of CT-Surfactant	56
3.14	The band gap as an direct a) The spinal MoFe ₂ O ₄ Nanoparticles (b) Al ₂ O ₃ Synthesis and (c) Nanocomposites as an indirect in presence the SDS-surfactant	57
3.15	The band gap as an direct a) Spinal MoFe ₂ O ₄ Nanoparticles (b) Al ₂ O ₃ Synthesis and (c) Nanocomposites as an Indirect in the presence of CT-Surfactant	58

3.16	The pH_{PZC} of (a) $MoFe_2O_4$ (b) Nanocomposites (c) Al_2O_3 at Different pH Values in the Presence of SDS-Surfactant	60
3.17	The pH_{PZC} of (a) $MoFe_2O_4$ (b) Nanocomposites (c) Al_2O_3 at Different pH Values in the Presence of CT-Surfactant	60
3.18	(a) The change of the $\ln(Co/Ct)$ with irradiation time at pH solutions of spinal $MoFe_2O_4$,(b) Relationship between the (k_{app}) and the different pH solution of spinal $MoFe_2O_4$, (c) Effect the different pH solution of spinal $MoFe_2O_4$ on (PDE%) with the presence of CT-Surfactant	64
3.19	(a) The change of the $\ln(Co/Ct)$ with irradiation time at pH solutions of Synthesis Al_2O_3 , (b) Relationship between the (k_{app}) and the different pH solution of Synthesis Al_2O_3 , (c) Effect the different pH solution of spinal $MoFe_2O_4$ on (PDE%) efficiency	66
3.20	(a) The change of the $\ln(Co/Ct)$ with irradiation time at pH solution of Nanocomposites ,(b) Relationship between the (k_{app}) and the different pH solution of Nanocomposites , (c) Effect the different pH solution of Nanocomposites on (PDE%) efficiency with the presence of CT-Surfactant	68
3.21	(a) The change of the $\ln(Co/Ct)$ with irradiation time at pH solutions of spinal $MoFe_2O_4$,(b) Relationship between the (k_{app}) and the different pH solution of spinal $MoFe_2O_4$, (c) Effect the different pH solution of spinal $MoFe_2O_4$ on (PDE%) efficiency with the presence of SDS-Surfactant	71
3.22	(a) The $\ln(Co/Ct)$ Variation with Irradiation time at various pH solution of Nanocomposites ,(b) Relationship between the (k_{app}) and the different pH solution of Nanocomposites , (c) Effect the different pH solution of Nanocomposites on (PDE%) efficiency with the presence of SDS-Surfactant	73
3.23	(a) The $\ln(Co/Ct)$ Variation with Irradiation time at various temperatures of spinal $MoFe_2O_4$ (b) Effect of the different temperature of spinal $MoFe_2O_4$ on (PDE%) efficiency with the presence of CT-Surfactant	77
3.24	(a) Eyring–Polanyi plot $\ln(k_{app}/T)$ VS. $1000/T$ (b) Arrhenius plot by spinal	78

	MoFe ₂ O ₄ <i>via</i> Synthesized Nanophotocatalyst de-colorization of Indigo Carmine IC Dye	
3.25	(a) The ln(Co/Ct) Variation with Irradiation time at various temperatures of Synthesis Al ₂ O ₃ (b) Effect of the different temperature of Synthesis Al ₂ O ₃ on (PDE%)	79
3.26	(a) Eyring–Polanyi plot ln (k _{app} /T) VS.1000/T (b) Arrhenius plot by Synthesis Al ₂ O ₃ <i>via</i> Synthesized Nanophotocatalyst de-colorization of Indigo Carmine IC Dye	79
3.27	(a) The ln(Co/Ct) Variation with Irradiation time at various temperatures of Nanocomposites (b) Effect of the different temperature of Nanocomposites on (PDE%) efficiency with the presence of CT-Surfactant	81
3.28	(a) Eyring–Polanyi plot ln (k _{app} /T) VS.1000/T (b) Arrhenius plot by Nanocomposites with the presence of SDS-surfactant <i>via</i> Synthesized Nanophotocatalyst de-colorization of Indigo Carmine IC dye	82
3.29	(a) The ln(Co/Ct) Variation with Irradiation time at various temperatures of spinal MoFe ₂ O ₄ (b) Effect of the different temperature of spinal MoFe ₂ O ₄ on (PDE%) efficiency with the presence of SDS-Surfactant	84
3.30	(a) Eyring–Polanyi plot ln (k _{app} /T) VS.1000/T (b) Arrhenius plot by spinal MoFe ₂ O ₄ <i>via</i> Synthesized Nanophotocatalyst de-colorization of Indigo Carmine IC dye	85
3.31	(a) The ln(Co/Ct) Variation with Irradiation time at various temperatures of Nanocomposites (b) Effect of the different temperature of Nanocomposites on (PDE%) efficiency with the presence of SDS-surfactant	87
3.32	(a) Eyring–Polanyi Equation plot ln (k _{app} /T) VS.1000/T (b) Arrhenius Equation plot by Nanocomposites with the presence of SDS-surfactant <i>via</i> Synthesized Nanophotocatalyst de-colorization of Indigo Carmine IC dye	89
3.33	The Relation of the Quantum Yield of Indigo Carmine dye with samples	89

	studied in the presence of SDS-surfactant at pH 5.3, Temperature 293.15 K	
3.34	The Relation of the quantum yield of Indigo Carmine dye with samples studied in the presence of CT-surfactant at pH 5.3, Temperature 293.15 K	90
3.35	Schematic Diagram of the photocatalytic system, hydroxyl radical-mediated to decolorization and degradation of IC Dye	91

List of Abbreviations and Symbols	
Abbreviations and Symbols	The Meaning
A_{accepte}	Acceptor species
Abs	Absorbance
AOPs	Advanced Oxidation Processes
Bg	Band gap
CB	Conduction Band
C_o	The Initial concentration of the Dye at the dark reaction
C_t	The Initial concentration of the Dye after irradiation
CT	Cetrimide
D	Doner species
e^-	Anionic Electron
E_a	Activation Energy
EDX	Energy Dispersive X-Ray Spectroscopy
E_g	Energy Gap

eV	Electron Volt
FTIR	Fourier Transformation Infrared
FWHM	Full Width half –maximum
h^+	Cationic Hole
HOMO	Highest Occupied Molecular Orbital
IC	Indigo Carmine
I_0	Light Intensity
ISC	Intersystem crossing
JCPDS	Joint Committec on Powder Diffraction Standards
k	Wave Factor
$k_{app.}$	Apparent Rate constant
D	Mean Crystallite Size
LUMO	Lowest Occupied Molecular Orbital
PDE	Photo decolourization Efficiency
RGO	Reduced graphene oxide
RhB	Rodamin B
ROS	Reactive Oxygen Species
SC	Semiconductor
SDS	Sodium Dodecyl Sulfate
T	Temperature
UV-A	Ultra Violet light in the Range from 315 to 380 nm

VB	Valance Band
XRD	X-Ray Diffraction
α	Absorbance Coefficient
β	Full Half-Maximum Intensity Width(FWHM) in Degrees
θ	Bragg Angle
λ	Wavelength in nm

CHAPTER ONE

Introduction

1.1. General Introduction

The ecological environment of people and other living things has been severely impacted by organic contaminants in groundwater, which has increased interest in wastewater treatment methods. Most methods applied to remove or degrade such as adsorption [1]. Fenton and photofenton [2], [3], photolysis [4], and photocatalysis [5], [6]. The photocatalytic process is one of the promising effluent treatment technologies. Which could remove or degrade the organic toxic pollutants using an environment-friendly and efficiently [7], [8], hence, many scientists are devoted to developing new photocatalysts with high efficiency to address the challenges of water pollution [9], [10], Semiconductor photocatalyst, especially visible light-driven photocatalysts have received significant attention because visible light radiation occupies half of the total solar energy on earth [11]. Thus, designing and implementing high-efficiency, low-cost, and stable photocatalysts driven by visible light is highly desirable for practical application. So there are a variety methods to remove dyes from wastewater due to their toxicity and danger, including adsorption, photocatalysis, photodegradation, membrane filtering, oxidation, and irradiation [12].

1.2. Advanced Oxidation Process (AOPs)

AOPs are one of the most recent technologies, which have the potential to transform organic pollutants into harmless elements including carbon dioxide (CO_2), H_2O , and mineral salts [13]. This approach is useful since it avoids the need for further by product separation in an aqueous solution [14], [15]. The term (AOPs) refers to a group of procedures that frequently make use photon oxidizing species such as hydroxyl-radicals ($\cdot\text{OH}$), which have a high in situ-produced oxidation potential ($E_o = 2.8 \text{ V}$) and then kick off a chain of processes that break down big molecules into smaller, less hazardous pieces. As shown in

Figure (1-1), the AOPs technique produces hydroxyl radicals ($\cdot\text{OH}$) in a variety of ways [16], [17].

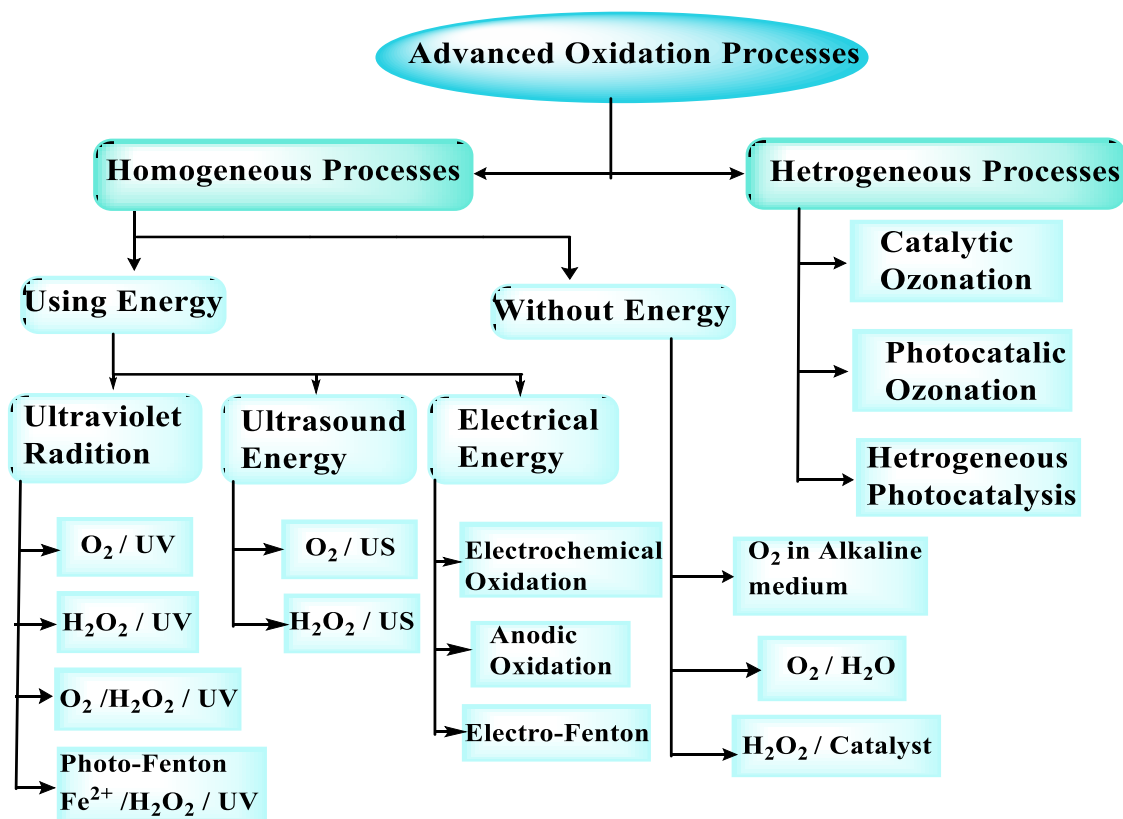


Figure (1-1). Schematic diagram of the most applications for advanced oxidation processes as a $\cdot\text{OH}$ source [18].

AOPs are declared to be capable and effective ways for pollutant elimination, however a novel methodology must be developed to safeguard human health and the environment from the harmful consequences of water contamination. AOPs techniques have evolved as a very inexpensive process that may be useful for removing pollutants from soil and water resources and turning them into toxic-free compounds [19]. They are increasingly being reported as a highly effective wastewater treatment solution for getting rid of contaminants with a high chemical constancy or low biodegradability [20]. Although these techniques are effective at removing pollutants that have high chemical persistence, complete mineralization is said to be substantially more expensive.

The technique can thus be used with other biological therapy techniques to reduce expenses [21]. Although the last approach to industrial wastewater treatment is intriguing, the discussion that follows only covers AOPs.

1.3. Semiconductors and Synthesized Nanophotocatalysts

Semiconductors (SCs) are solids with electrical conductivity ratings that can be crystalline or amorphous with band gap (Bg) ranged from 0.5 eV to 5 eV. The values of the intermediate states, which lie between a metal and an insulator, can be changed by altering the impurity, temperature, quantum dot size, or illumination. Understanding the properties of SC requires knowledge of the electrical conductivity band theory. At absolute zero Kelvin, the valence band of a semiconductor is filled with all of its electrons, while the conductive band is devoid of electrons. The band gap is the area that exists between the conductive band and the valence band [22],[23]. When the Bg between 1.1 to 5 eV the semiconductors are called photoconductors or photocatalysts[5]. The photocatalyst can be classified depended on position of fermi level to n-type(Fermi level is close to the conductive band) and p-type(Fermi level is close to the valance band) [24]. Based on Figure (1-2), the electrons (e^-) in valence band will travel to the conduction band when a photocatalyst is exposed to light with energy equal to (or greater than) the band gap energy, leaving a hole (h^+) in the valence band (step I). Step II: The electron-hole pairs may combine once more, releasing the input energy as a heat and having no chemical consequence. However, if the electrons and holes go to the surface of the photocatalyst, they can participate in redox reactions with adsorbed species such oxygen, water, and organic or inorganic species (steps III and IV) [25], [26]. The major reactions responsible for the cationic photocatalytic effect are interfacial redox reactions of electrons and holes that are generated upon bandgap excitation, despite the fact that the physics underlying the parting of charge carriers varies

with different applications and the surface-electronic structure of the photocatalyst [27], [28].

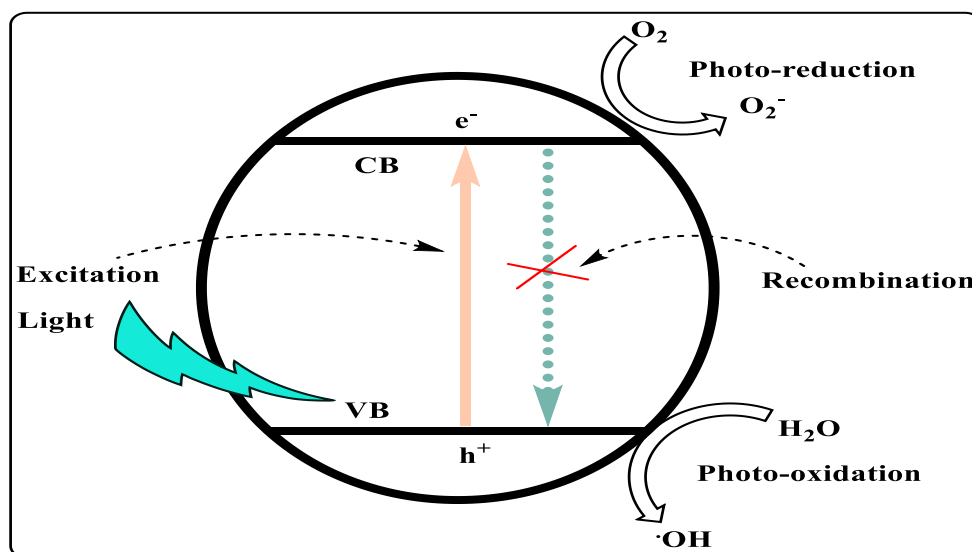


Figure (1-2) Schematic illustration of the main reactions taking place on a bulk or a nano photosemiconductor under light irradiation.

The following steps that might be described above could be briefly expressed :

Light absorption	$SC + h\nu \rightarrow SC^*$	Step I
Recombination	$e^-_{CB} + h^+_{VB} \rightarrow \text{heat}$	Step II
Reduction reaction	$A + e^-_{CB} \rightarrow A^-$	Step III
Oxidation reaction	$D + h^+_{VB} \rightarrow D^+$	Step IV

Where, A is acceptor, D is donor

However, these redox processes are the fundamental mechanism of photocatalytic processes. Valence band (VB) holes are crucial components that stimulate the oxidative breakdown of environmental contaminants in photocatalytic decolorization [29]. When the holes and water interact, an oxidation process known as valence band oxidation results in the formation of the hydroxyl radical ($\cdot\text{OH}$) as a very active oxidant with an oxidation potential

of 2.8 V. Surface pollutants may be quickly targeted by $\cdot\text{OH}$ and transformed into H_2O and CO_2 . The organic contaminants are broken down in water by photocatalysis has been widely addressed in the literature [29], [30], [31]. In the photocatalysis process, the surface species that function as traps by adsorbing them on the photo-catalyst surface increase with increasing in the photocatalyst's efficiency, whereas the main component that lowers efficiency is photo electron-hole recombination, there are three important recombination routes exist [31],[32]. Firstly direct recombination occurs when a photoelectron in a conducting band falls into an empty state in the valance band and, by electrostatic attraction, joins a photo hole, secondly due to the surface species' capacity to collect photogenerated charge carriers (photo-electron-holes) and performs chemical reaction, surface recombination has a reduced likelihood Finally, because the recombination centers are at lattice sites transition within the bulk of the crystal and transition beyond the initial ground state, recombination at recombination centers (volume recombination) is highly likely [22], as shown in Figure (1-3).

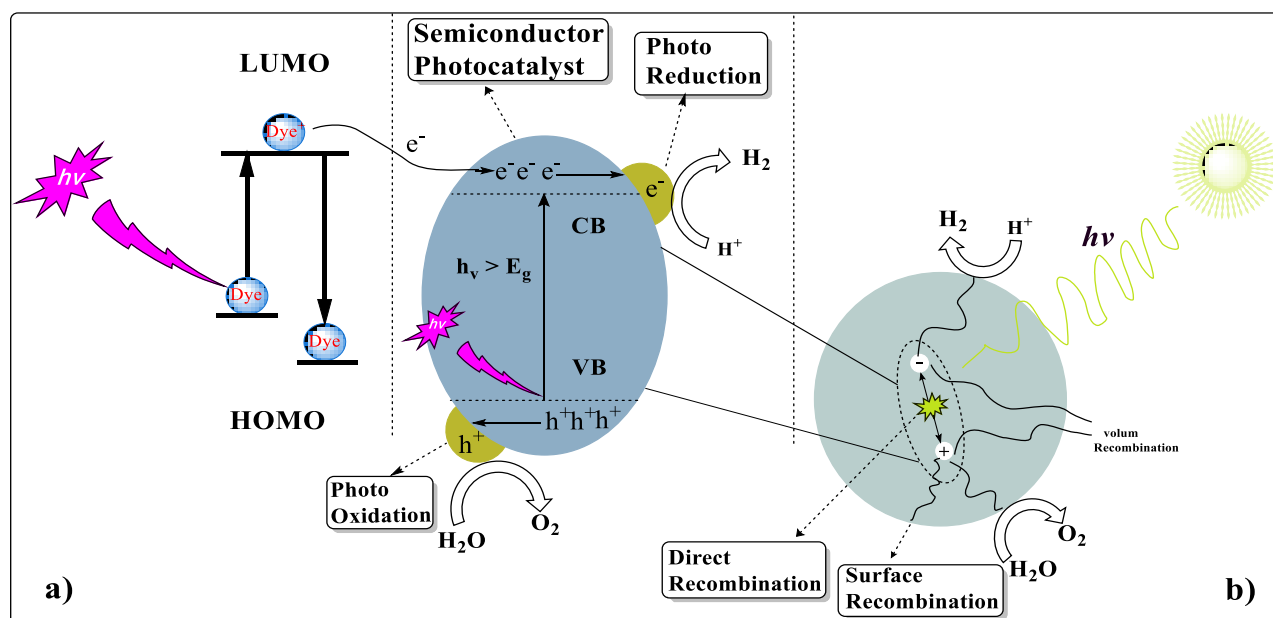


Figure (1-3). a) Photocatalytic mechanism using a photosemiconductor b) Types of recombination Processes. (Modified from References [33], [34]).

1.4. The Synthesized Spinel (MoFe_2O_4) Nanophotocatalyst

The spinel semiconductor is having a formula AB_2O_4 , where the ions A^{2+} and B^{3+} have tetra (A) and octa [B] voids. [35], [36]. Due to their electrical resistance and magnetic characteristics when utilized as high-frequency devices, ferrite composites are receiving increased attention [37]. Chemical substitution can be used to change the magnetic and electric properties [38]. Although n-type (SC) make up the majority of spinel-type Fe_3O_4 , p-type conduction can also be achieved by substituting high valence ions like $\text{Mo}^{3+/4+}$, Ti^{4+} , and Ge^{4+} [39]. MoFe_2O_4 is one of the p-type spinel magnetites that is gaining attention from researchers [40]. The inverse spinel structure of MoFe_2O_4 is composed of half of the Fe ions at tetrahedral (T_d) A sites and the remaining Fe and Mo ions at octahedral (O_h) B sites Figure (1-4).

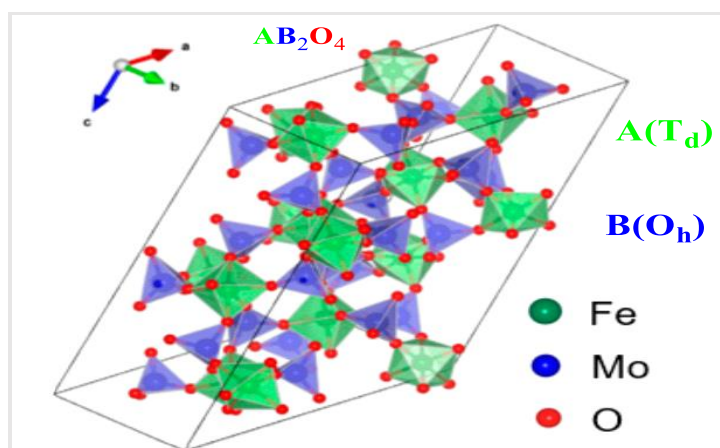
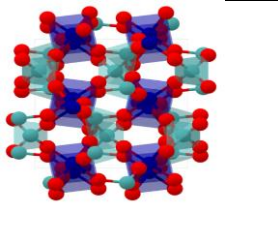
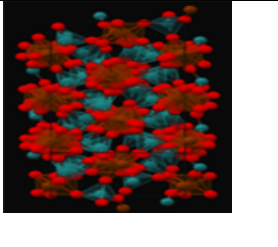
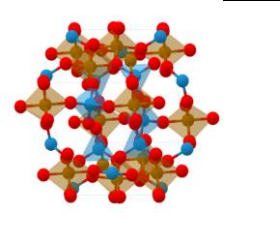


Figure 1-4. Crystal structure of spinel-type oxide consisting of tetrahedral (T_d) A and octahedral (O_h) B [41].

Spinel nanoferrites are effective for a variety of oxidations of organic compounds in wastewater due to their photocatalytic capabilities also strong interest in biomedical applications [42], [43]. Molybdenum ferrites typically exhibit an anion selectivity barrier and poor solvency, which make them resistant to corrosion in sour environments [44], [45]. The spinel Molybdenum Ferrite (MoFe_2O_4) is regarded as one of the most important materials because of

its exceptional redox characteristics, low cost, and thermal and chemical durability [46]. Molybdenum Ferrite (MoFe_2O_4) is a significant n-type binary metal oxide semiconductor that has drawn increasing attention in the fields of industrial catalysis, lithium/sodium batteries, supercapacitors, and gas sensors due to its excellent redox properties, catalytic activity, and chemical stability compared to corresponding single metal oxides [47], [48]. There is relatively little evidence between (MoFe_2O_4) morphologies with photocatalytic capabilities. However, considering prospective applications with large-scale in daily life, it is not advised due to the high cost of UV light during the photocatalytic processes. Visible light illumination (400 nm) is mostly regarded as a low-cost light source [49], [46]. Therefore, efficiently utilizing the abundant and natural solar energy, various attempts have been made to promote photocatalysts with narrow band gaps by visible light illumination. Sol-gel, co-precipitation, solid-state reactions, hydrothermal, and solvothermal processes have all been used to create (MoFe_2O_4) powder [50]. Because it is crucial to the performance of the photocatalyst, the control of the Mo/Fe ratio and structure has received good attention; however, the morphological control of the (MoFe_2O_4) structure has received little research [51], [52]. In the table (1-1), some of the key characteristics of MoFe_2O_4 crystals are shown.

Table (1-1). Physiochemical properties of MoFe_2O_4 Crystals.

Crystalline Structure type	Orthorhombic	Monoclinic	Triclinic
Crystal structures			

Lattice Constant (Å)	a = 9.46 b = 9.55 c = 13.18	a = 16.18 b = 9.52 c = 16.24	a = 6.93 b = 8.66 c = 10.38
Stability	Stable	Metastable	less Stable
Color	Brown Powder	Brown Powder	Brown Powder
Band gap	Direct (2.66 eV)	Direct(2.50 eV)	Direct(2.43 eV)
Density	3.30 g·cm ⁻³	3.32 g·cm ⁻³	3.63 g·cm ⁻³
Possible Oxidation States	Mo ⁶⁺ ,Fe ³⁺ ,O ²⁻	O ²⁻ ,Mo ⁶⁺ ,Fe ³⁺	O ²⁻ ,Fe ³⁺ ,Mo ⁶⁺
Application	Nanophotocatalyst	Nanophotocatalyst	Nanophotocatalyst
Ref.	[53]	[54]	[55]

1.5. Synthesis Al₂O₃ as photocatalysts

Aluminum oxide (Al₂O₃) nanoparticles are utilized in a variety of adsorbent and catalyst applications, such as the adsorption of catalysts in the manufacturing of polyethylene, hydrogen peroxide, and as a selective adsorbent for numerous compounds, such as arsenic and fluoride, as well as the removal of sulfur from gas streams. Due to its hardness, chemical inertness, high melting point, non-volatility, and resistance to oxidation and corrosion, aluminum oxide materials are widely utilized in ceramics, refractories, and abrasives [56],[57]. Alumina's significance as a catalyst or catalytic support for several chemical processes has also been well acknowledged [58]. According to Figure (1-5), aluminum oxide are chemical formula Al₂O₃. In the fields of mining, ceramics, and materials science, it is sometimes referred to as alumina or aloxite. Anhydrous Al₂O₃ comes in two different forms: α-Al₂O₃ and γ-Al₂O₃. Alpha-Al₂O₃ is indefinitely metastable at low temperatures and stable at high

temperatures. It may be made by heating Al_2O_3 or any hydrous oxide to temperatures exceeding 1000°C . It naturally occurs as the mineral corundum. Al_2O_3 is tough, resistant to hydration, and to acid assault.

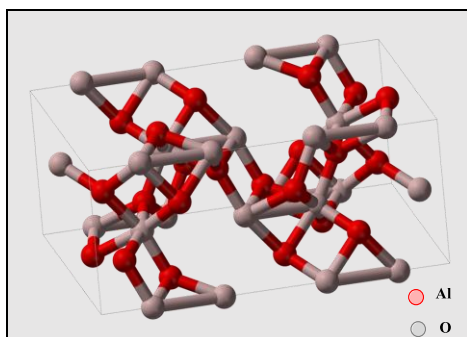
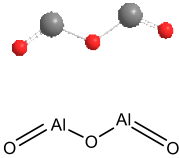
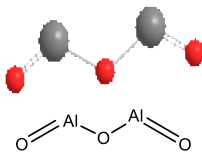


Figure (1-5). The 3D molecular structure of Alumina [57].

Due to their advantageous textural qualities and inherent acid-base properties, aluminas are often employed as catalyst supports. For example, in the automotive and petroleum sectors, γ -alumina, which has a crystalline structure and a huge surface area, is frequently utilized as catalysts, catalytic supports, and adsorbents. Large-surface-area alumina supports with the appropriate acidic-basic surface characteristics can frequently lead to improved catalytic performance. Aluminum oxide is an insulating substance with band gap energies exceeding 5 eV [59]. By modifying the amount of flaws on its surface, the energy in this gap may be decreased to as little as 2.5 eV, previous studies have shown that the transformed surface might be thought of as a new phase with distinct characteristics connected to novel surface chemistry and chemical activity [60]. It is important to note that the band gap value varies on the synthesis process, It is well known that various metastable polymorphs of Al_2O_3 exist (transition aluminas phases such as γ , η , δ , θ , and χ) except the thermodynamically stable form of α - Al_2O_3 (corundum) [61]. Table (1-2).

Table (1-2). Physiochemical properties of synthises Al₂O₃ Crystals.

Type	α -Al ₂ O ₃	γ -Al ₂ O ₃
Crystal structures		
Color	white powder	white powder
Stability	Stable	Stable
Band gap	Indirect 4.42 eV	Direct 5.85 eV
Lattice Constant (Å)	a = 11.79 b = 2.91 c = 5.62	a = 4.81 b = 4.81 c = 13.12
Density	3.63 g·cm ⁻³	3.87 g·cm ⁻³
Appllication	Catalyst or catalytic support	Catalyst or catalytic support
Ref.	[62]	[63]

1.6. Surfactants

Surfactants are chemical compounds that decrease the surface tension or interfacial tension between two liquids, a liquid and a gas, or a liquid and a solid. It is important to note that well-structured photocatalysts can promote electronic transfer, improve optical absorption, and improve photocatalytic performance by having a core-shell structure, uniform spherical structure, and hierarchical multilayer structure [64], [65]. In the synthesis of photocatalysts, surfactants, an amphiphilic substance with hydrophilic and hydrophobic groups,

have been shown to be an effective shape-directing agent, primarily by controlling their overall shape by adsorbing surface active molecules on various crystal faces of the nucleation center [66]. The kinds of surfactants can be classified to four types according to the table (1-3) [67].

Table (1-3). The classified of surfactants with common used and examples [68], [69],[70]

Types	Info.	Examples and used
Cationic surfactants	These molecules contain at least one hydrophobic hydrocarbon chain bonding with a positively charged nitrogen atom, or other alkyl groups.	-Cetrimide (CT), Quaternary ammonium compound (QAC), and Cetyltrimethylammonium bromide (CTAB) -Used in detergents, fabric softeners, and hair conditioners.
Anionic surfactants	The hydrophobic part of the molecule is mostly an alkyl chain, alkylphenyl ether or alkylbenzene bonding carboxyl, sulphate, sulphonate, or phosphate.	-Sodium dodecyl sulphate (SDS), Sodium lauryl sulphate (SLS), and Stearic acid (SA). -Used in pharmaceutical formulations to increase the efficiency of the active ingredients by direct binding to the drug
Amphoteric surfactants	They are dependent on the pH. This molecules can changed its charge from net cationic to anionic from low to high pH, with zwitterionic behaviour at intermediate pH	-Amine oxide (AO) -Used in textile industry as anti-static agents, in rubber industry as foam stabilisers and polymerisation catalysts, and in deodorant bars as antibacterial agents
Nonionic	The hydrophobic part of nonionic surfactants is mostly an alkylated phenol derivative, fatty acid, or long-chain linear alcohol, but the hydrophilic part is mostly an ethylene oxide chain of various lengths.	-Fatty acid ethoxylate (FAE), Alcohol ethoxylate (AE), and hexamethylenetetramine (HMTA) -Used as emulsifiers, wetting agents, and foam stabilisation agents.

However, the mechanism of the surfactant-assisted synthesis of photocatalysts is slightly different with different Synthesis methods. Therefore, we summarize the mechanism in combination with the synthesis method and analyze them by the reaction process reported in literature. Surfactant-assisted such as SDS, CT and CTAB, etc. There are four types of surfactants

1.7. The Effect of Surfactant Type

The type impact of surfactant is important in the synthesis of photocatalysts and has been utilized to influence the form of these catalysts. The charge, shape, hydrophobic chain length, and functional groups of surfactants are the major factors that determine the kind of surfactants [71]. There are two main and most common types of surfactants.

1.7.1 Anionic Surfactant as a Sodium Dodecyl Sulfate (SDS)

Sodium dodecyl sulfate (SDS or NaDS), commonly known as sodium laurilsulfate or sodium lauryl sulfate (SLS), is an anionic surfactant that belongs to the alkyl sulfates surfactants family. An artificial organic molecule (salt) with an amphiphilic structure, organosulfate with a tail chain made up of 12 carbon atoms and the chemical formula a $\text{CH}_3(\text{CH}_2)_{11}\text{SO}_4\text{Na}$ figure (1-6) [72]. Sodium dodecylsulphate SDS, like other surfactants, contains an amphiphilic molecule with both hydrophilic and hydrophobic moiety, due to its chemical, physicochemical, and utilitarian qualities, is widely employed for both basic research as well as industrial applications. This anionic surfactant was used in several personal care items, including toothpaste, detergents, and synthesis goods [72], [73].

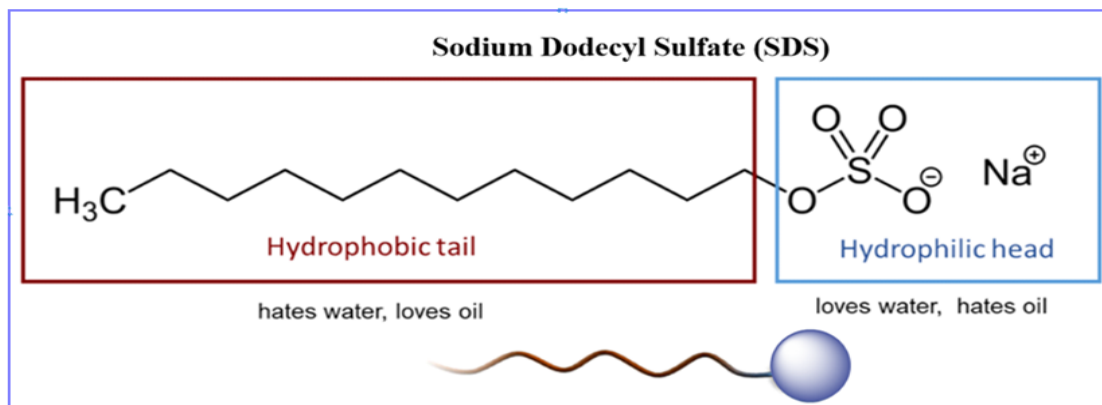


Figure (1-6). Chemical structure of sodium dodecyl sulfate (SDS).

1.7.2. Cationic Surfactant as a Cetrimide (CT)

Cetrimide (CT) is a three-cationic surfactant, dodecyl-, tetradecyl-, and hexadecyltrimethylammonium bromides, which are mixed to create cationic surfactants. By weight, tetradecyltrimethylammonium bromide constitutes the bulk of the combination and serves as the only surfactant [74]. CT is a cationic charge on the micelle surfaces in an aqueous solution caused by the cationic surfactant. Because phosphate (PO_4^{3-}) ions and micelles are attracted to one another electrostatically, the anionically charged PO_4^{3-} ions join with the surfaces of the cationically charged micelles to create a network structure. The network gradually transforms into rod-shaped micelles, which then serve as the nucleation center. Figure (1-7).

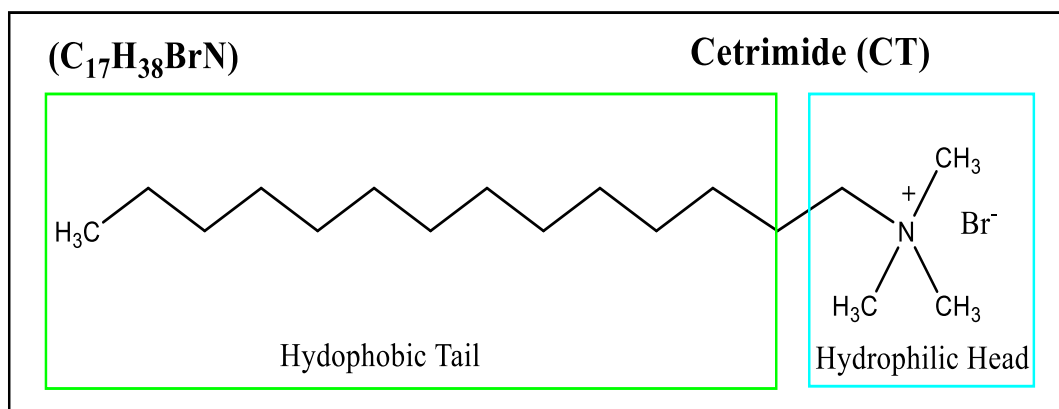


Figure (1-7). Chemical structure of Cetrimide (CT).

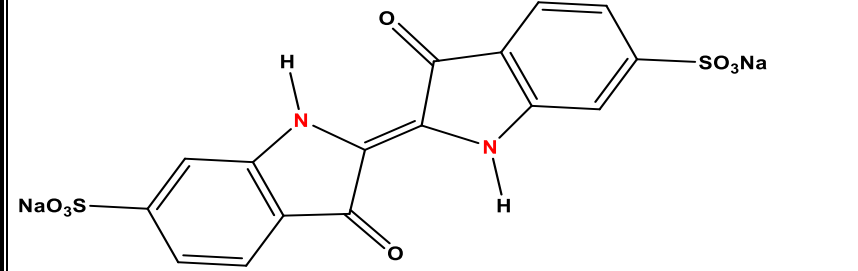
1.8. dyes

Many different industries, including the textile, paper, plastic, food, printing, cosmetic, and pharmaceutical sectors, employ dyes extensively. The majority of dyes are organic compounds with complicated aromatic structures and a range of functional groups [75]. However, some colors emitted from industrial effluents into receiving streams are sources of water pollution. The majority of dyes and the byproducts of their degradation are highly toxic, mutagenic, carcinogenic, and allergenic, the environment's unfitness for humans and aquatic life, which is brought on by the dyes in water effluents, causes chronic and acute illnesses [76], [77]. The majority of the dye molecules are soluble in water and may be stable to heat and light. It may be seen with the naked eye since its light has wavelengths between 400 and 800 nm. The degradation of dyes in wastewater can be accomplished through a variety of biological, chemical, and physical processes, including photolysis, adsorption, chemical precipitation, sonochemical degradation, and electrochemical precipitation because dyes typically have a complex structure and altered stability [78], [79]. Moreover, according to their chemical makeup, dyes may also be divided into categories such as xanthenes, heterocyclic, nitro, stilbene, phthalocyanine, indigoid, polymethine, and anthraquinone [80].

1.8.1. Indigo Carmine (IC)

Indigotin or indigo carmine (IC) is one of the most widely used synthetic dyes. Although it was formerly made from a plant of the genus *Indigofera*, it is nonetheless harmful to the environment. This dye is mixed with Patent Blue V to turn food blue. These two shades of blue are used in coatings, pharmaceuticals as dye of drug capsol, ice cream, and confectionery [81]. Although indigo carmine may be created naturally by the indigo sulfonation process, indigo is often also created synthetically through the fusion of the

chemical N-phenyl glycine in a solution of sodamide, sodium hydroxide, and potassium hydroxide while being compressed by ammonia. Consequently, indigo carmine should be regarded as a man-made food dye [82]. According to current knowledge, dye molecules consist of a mixture of unsaturated organic compounds with auxochromes acting as color binders with fibers and chromophores acting as color transporters [83]. This chromophore group imparts color to a molecule. Unsaturated organic molecules including aromatic hydrocarbon compounds and their derivatives, phenolic compounds and their derivatives, and nitrogen-containing hydrocarbon compounds all play a role in the synthesis of colors in a molecule. Because indigo carmine is poisonous to rats, pigs, and people, it can have an adverse effect on the aquatic environment. Waste containing this substance must be handled to reduce or remove its detrimental effects on biota due to its toxicity to nature [84]. The treatment and eradication of color from textile waste can be accomplished using a variety of conventional methods, including glass, chemical, and biological processes, membrane purification, chemical precipitation, adsorption, electrochemical degradation, advanced oxidation processes (AOPs), and others [85]. The chemical structure of Indigo Carmine dye is illustrated and some of the properties in the scheme (1-2).



IUPAC name	disodium;2-(3-hydroxy-5-sulfonato-1H-indol-2-yl)-3-oxoindole-5-sulfonate
Molecular formula	$C_{16}H_8N_2Na_2O_8S_2$
Molecular weight	466,36 g/mol ⁻¹
Synonym	Acid Blue 74 λ _{max} = 600 nm
Class	Indigoid

Scheme (1-2). Chemical structure of indigo carmine (IC) and some important properties [86].

1.9. Photocatalytic Decolorization of Dyes

Currently, the formation of Reactive Oxygen Species (ROS) by One of the most efficient dye decolorization processes is photocatalysis, organic ligands, and metal-organic ligand complexes are examples of organic-colored compounds [87]. Photodecolorization is an abiotic decolorization process in the aquatic environment [88]. In recent years, a great deal of study has been done to remove these pollutants using optical catalysts, and it has been concluded that a photocatalytic decolorization process is an ecologically friendly technology that does not result in secondary pollution. During the exposure to light, photocatalysts and electron-hole pairs were formed, and they are now helping to the process of speeding up dye decolorization [89]. Additionally, to remove chlorinated phenolic chemicals, incredibly secure and efficient photocatalytic

technologies are used under certain parameters, such as temperature, pressure, and concentration. Usually, the photocatalytic process's by-products are harmless or just mildly harmful [90]. Direct photo-decolorize in aquatic environments, analogous to dye degradation, is an important pathway for pesticide deterioration [91]. In conclusion, photo-decolorization includes procedures like photochemical mineralization, photopriming, and microbiological photo-inhibition [92]. Thus, Heterogeneous photocatalysis offers a highly efficient means of addressing environmental issues [93]. It paved the way for the development of innovative semiconductor photocatalysts capable of photochemical activity. The high rate of recombination of photogenerated electron-hole pairs made during the photo decolorization process, however, hampers effective de-colorization. The dye degradation procedures were performed as shown in Figure (1–13) under light [46].

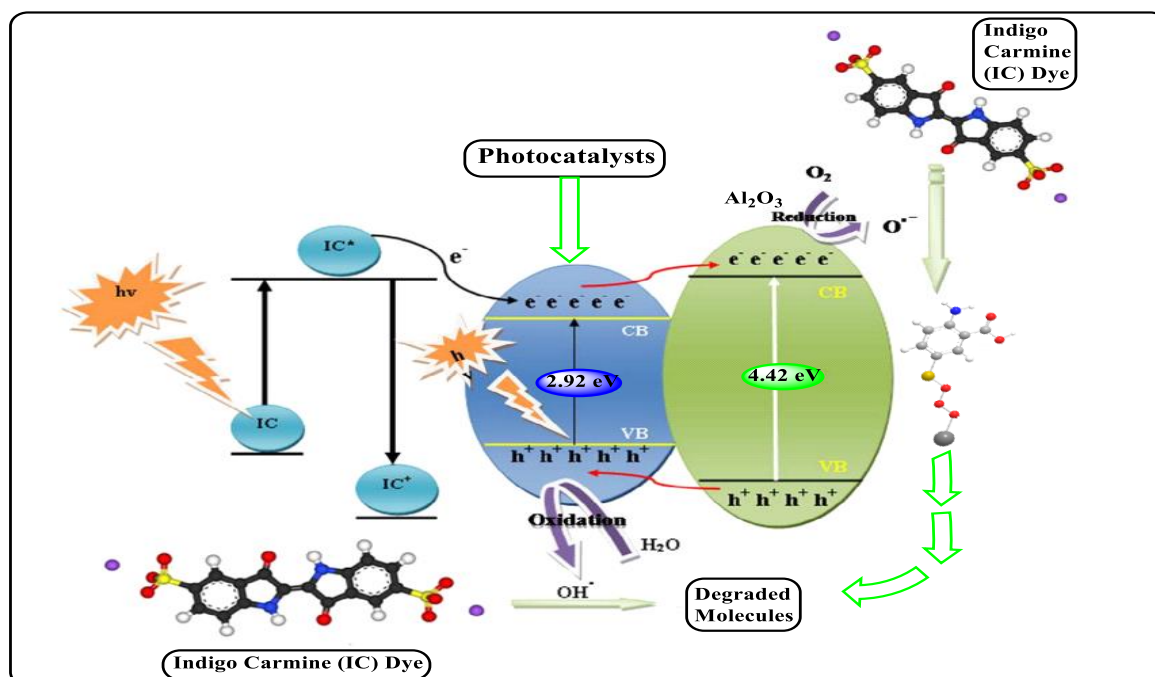


Figure (1-8). Diagram depicts the degradation mechanism of dye on the catalyst's surface (Modified from Ref.) [94]).

1.10. Literature Review

There are a several of studies research on the Synthesis of Spinel MoFe_2O_4 and their nanocomposites. **In 2017** Jintao Li and co-workers [95],synthesized $\text{MoO}_3/\text{MoFe}_2\text{O}_4$ heterostructure nanomaterials by Hydrothermal method and findings the surface of the MoO_3 nanobelts was evenly covered with MoFe_2O_4 nanoparticles. At the ideal working temperature of $250\text{ }^\circ\text{C}$, the $\text{MoO}_3/\text{MoFe}_2\text{O}_4$ nanocomposites demonstrated improvement sensing responsiveness and selectivity to toluene vapor compared to bare MoO_3 nanobelts.

In 2018 Shuang Zou and co-workers [96], used polyvinyl pyrrolidone (PVP) as a surfactant, the hydrothermal technique was used to create the MoFe_2O_4 nanoparticles. The findings showed that monoclinic nanocrystals with an average size of 50 nm made up the MoFe_2O_4 nanoparticles. The MoFe_2O_4 nanoparticle-based sensor performs well at detecting gases, particularly acetone. Acetone greatly outperformed other gases in terms of responsiveness. At the sensor's ideal working temperature of $340\text{ }^\circ\text{C}$, the responses to 1 ppm and 100 ppm acetone were 2.45 and 24.7, respectively.

In 2019 Tsukasa Katayama and co-workers [41] employed the Pulsed laser deposition (PLD) to effectively create high-quality MoFe_2O_4 epitaxial films that show p-type conductivity and room-temperature ferrimagnetismThe outcome demonstrates that films with cation-vacant spinel structures displaying n-type conductivity are created by utilizing the MoFe_2O_6 target even under reductive deposition circumstances, in contrast to films with spinel MoFe_2O_4 epitaxial films obtained by employing the MoFe_2O_4 target.

In 2020 Adel A Ismail and co-workers [46], developed unique green approach to create mesoporous $\text{Ag}_2\text{O}/\text{MoFe}_2\text{O}_4$ nanocomposites for tetracycline (TC) photodegradation under visible light irradiation. The procedure was based

on a straightforward sol-gel route with the presence of nonionic surfactant. Compared to the bulk material that is typically manufactured, the resulting $\text{Ag}_2\text{O}/\text{MoFe}_2\text{O}_4$ has a higher surface area thanks to its 2D mesoporous structure. On the mesoporous MoFe_2O_4 surface, Ag_2O Nanoparticles with a particle size of 3 nm are evenly distributed in a spherical shape.

In 2022 P. Santhoshkumar and co-workers [97], reported the Glycerol was used to facilitate the Synthesis of iron molybdate ($\text{Fe}_2(\text{MoO}_4)_3$) materials, and a variety of physicochemical methods were used to corroborate the materials' structural and chemical composition. It breakdown of Congo red and methylene blue, attaining 91% and 96% .

In 2023 Selvam Thulasi and co-workers [98], made the MoFe_2O_4 /reduced graphene oxide (RGO) nanocomposites using a straightforward hydrothermal method, and it was utilized to create highly effective dye-sensitized solar cells (DSSCs).

In the same year 2023, Lian Chang and co-workes [99], created the MoFe_2O_4 using environmentally friendly method. It used to eliminate RodanminhB (RhB) *via* peroxymonosulfate activation. Results from UV-vis and XPS experiments showed that the high valence Mo(VI) was the active center that started the nonradical-dominated pathway.

1.11. The aim of the work

This work includes many aims:

1. The bare spinel Molybdenum ferric nanoparticles were prepared by the hydrothermal method in the presence of two types of surfactant (cationic and anionic).
2. The Nanocomposites from spinel Molybdenum ferrite and synthesis Alumina were Prepared using indirect ultrasonic waves as a friendly method.
3. The fourier transform infrared (FT-IR), X-ray diffraction(XRD), Scan Electronic Microscope(SEM), Energy Dispersive X-rays(EDX), Zeropoint charge (pH_{ZPC}) and band gap (Bg) were used to identify .
4. Studied the photoactivity of prepared MoFe_2O_4 , synthesis Al_2O_3 , and their prepared Nanocomposites by measuring the effects of the following parameters on decolorized of Indigo Carmine dye:
 - a. Dose of photocatalyst samples
 - b. Temperature.
 - c. Initial pH Solution.

CHAPTER TWO

Experimental

2.1. Chemicals

All chemicals and materials that used in this study are of chemical market and used without purification as showned in Table (2-1)

Table (2-1): Sources and purities of the used chemicals

No.	Chemicals	Company supplied	Purity and percentage
1.	Hydrochloric acid (HCl) (38.0-36.5) %	J.K. Baker, Netherlands.	(98-99%)
2.	1,10- Phenanthroline (C ₁₂ H ₈ N ₂)	Seelze, Hannover, Germany: Riedel-De-Haen AG.	(99.97) %
3.	potassium oxalate (K ₂ C ₂ O ₄ .H ₂ O)	Seelze, Hannover, Germany: Riedel-De-Haen AG.	(99.98) %
4.	Sulphuric acid (H ₂ SO ₄)	CDH, India	(99.99) %
5.	Nitrogen (N ₂)	BDH	(99.99)%
6.	Cetrimide (CT) C ₁₇ H ₃₈ BrN	CDH, India	96-101%
7.	Alumina (Al ₂ O ₃)	Merck, Switzerland	98-99.9%
8.	Absolute Ethanol (C ₂ H ₅ OH)	Chem.lab, Belgium.	99.9%
9.	Indigo Carmine (IC) dye (C ₁₆ H ₈ N ₂ Na ₂ O ₈ S ₂)	CDH, India.	99.9%
10.	Sodium Dodecyl Sulfate (SDS) NaC ₁₂ H ₂₅ SO ₄	CDH, India	99.9%
11.	Sodium hydroxide (NaOH)	USA-based Sigma Chemical Company	99.98%

12.	Potassium chloride (KCl)	BDH	99.99%
13.	Potassium hydroxyl (KOH)	Merck, Switzerland	99.99%
14.	Sodium molybdate ($\text{Na}_2\text{MoO}_4 \cdot 2\text{H}_2\text{O}$)	Sigma cheml co. USA.	99%
15.	Iron (III) sulfate hydrate ($\text{Fe}_2(\text{SO}_4)_3 \cdot \text{H}_2\text{O}$)	Evans, Mf-Dica, England	(99.98) %
16.	Ferric nitrate ($\text{Fe}(\text{NO}_3)_3 \cdot 9\text{H}_2\text{O}$)	Sigma cheml co. USA.	99%

2.2. Instruments

All Instruments and tools are used in this study was shown in Table (2-2).

Table (2-2). Instruments and tools, company and places that are used in this study

No.	Instrument	Company	Place
1.	Double-beam-UV-Visible spectrophotometer	AA-1800, Shimadzu, Japan.	University of Kerbela, College of Science, Dep. chemistry
2.	Fourier-transform infrared spectroscopy (FTIR)	FT-IR-8400S, Shimadzu, Japan	University of Kerbela, College of Science, Dep. chemistry
3.	Magnetic Stirrer for Hotplates	Heido MrHei Standard, Germany	University of Kerbela, College of Science, Dep. chemistry
4.	Oven	Memmert, Germany	University of Kerbela, College of Science, Dep. chemistry
5.	pH meter with digital display	Singapore 2100 OAICTON	University of Kerbela, College of Science, Dep. chemistry
6.	Scanning Electron Microscopy (SEM), Energy-dispersive X-ray	(kyky EM) 320.,	Alkhora Company, Iraq

	spectroscopy (EDX)	USA	Baghdad – Alyarmook
7.	Sensitive balance	BL 210 S, Sartorius Germany	University of Kerbela, College of Science, Dep. chemistry
8.	Single-beam-UV-Visible Spectrophotometer	Spectro SC, LaboMed, Inc	University of Kerbela, College of Science, Dep. chemistry
9.	Steeliness steel Teflon tube autoclave	TOPT-HP100 TOPTION UNITED KINGDOM	University of Kerbela, College of Science, Dep. chemistry
10.	The centrifuge	Germany-Hettich Universal II	University of Kerbela, College of Science, Dep. chemistry
11.	Ultrasonic bath	DAIHAN Scientific, Korea.	University of Kerbela College of Science, Dep. chemistry
12.	UV(A) source ,High-Pressure Mercury Lamp (400W)	China of Radium.	University of Kerbela, College of Science, Dep. chemistry
13.	X-ray diffraction	Rigaku-Ultima IV	Ministry of Science and Technology .Iraq

2.3. Set of Synthesized Nanophotocatalyst Reactors

The photocatalytic reactor unit shown in figure (2-1) was utilized for all photocatalyst studies.

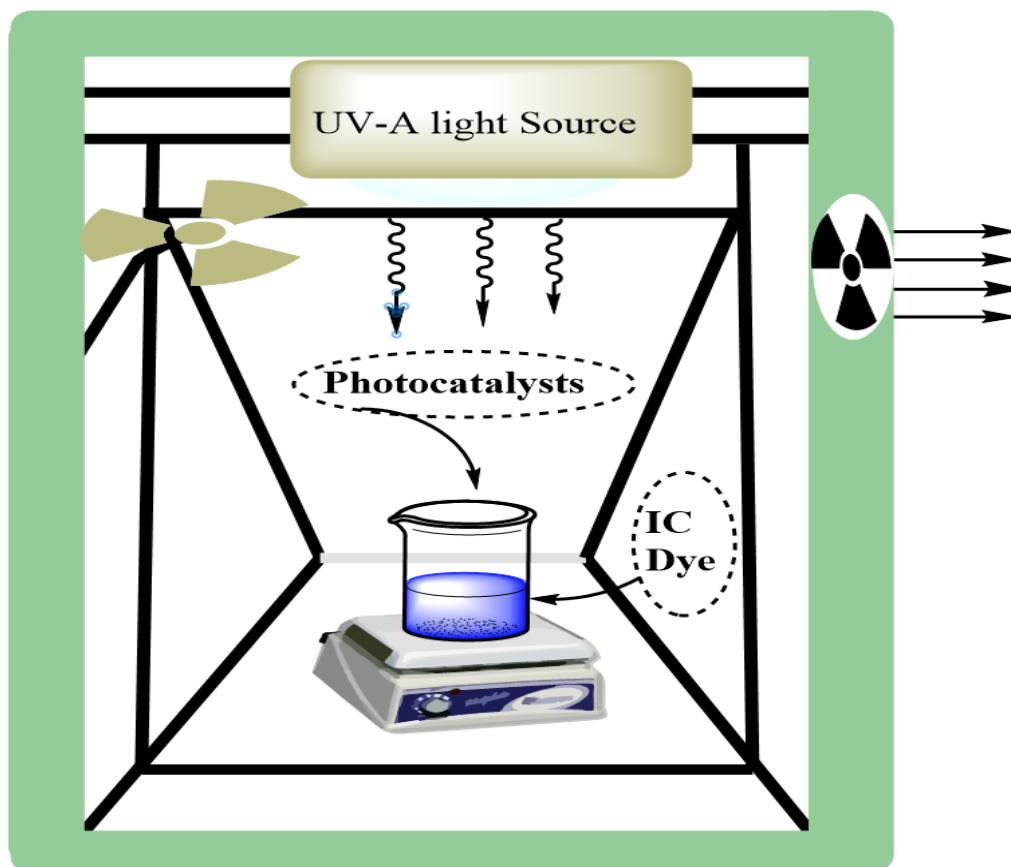
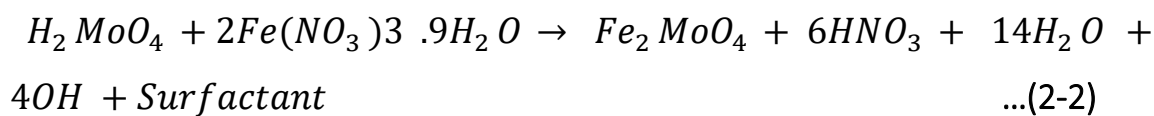
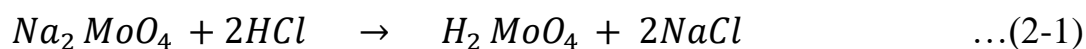


Figure (2-1): Homemade photo reactor contents from the wooden box (1), High-pressure mercury lamp(400W) (2), vacuum fan (3) 500 cm³ Pyrex glass beaker (4), Teflon bar (5), and magnetic stirrer (6).

2.4. Synthesis of MoFe₂O₄ nanoparticles in the presence of surfactants

Bare MoFe₂O₄ nanoparticles were prepared in presence the surfactant by a facile hydrothermal method. In a typical synthesis, 2.828 g Ferric Nitrate (Fe(NO₃)₃·9H₂O) was dissolved in 35 mL distilled water, and 0.846 g sodium molybdate (Na₂MoO₄·2H₂O) a dissolve separately, in 10 mL of HCl and 25 mL of distilled water. The Na₂MoO₄ solution was step by step added into the

$\text{Fe}(\text{NO}_3)_3$ solution with vigorous stirring at room temperature, as the equation (2-1 and 2-2)



Then 0.5g of surfactants (Sodium Dodecyl Sulfate (SDS) or Citermide (CT) was added separately. After stirring for 15 minutes, the resulting yellow mixture was put in a 100 mL Teflon-lined autoclave. The autoclave was then sealed and maintained at 180°C for 5 h. Subsequently, the autoclave was cooled to room temperature for 2 h. After filtration, the obtained solid sample that light and dark brown color was washed with distilled water and then ethanol several times to ensure all the amounts of cationic ions of precursor salts and humidity were removed. The figure (2-2) depicts the entire process of preparing Molybdenum Ferrite.

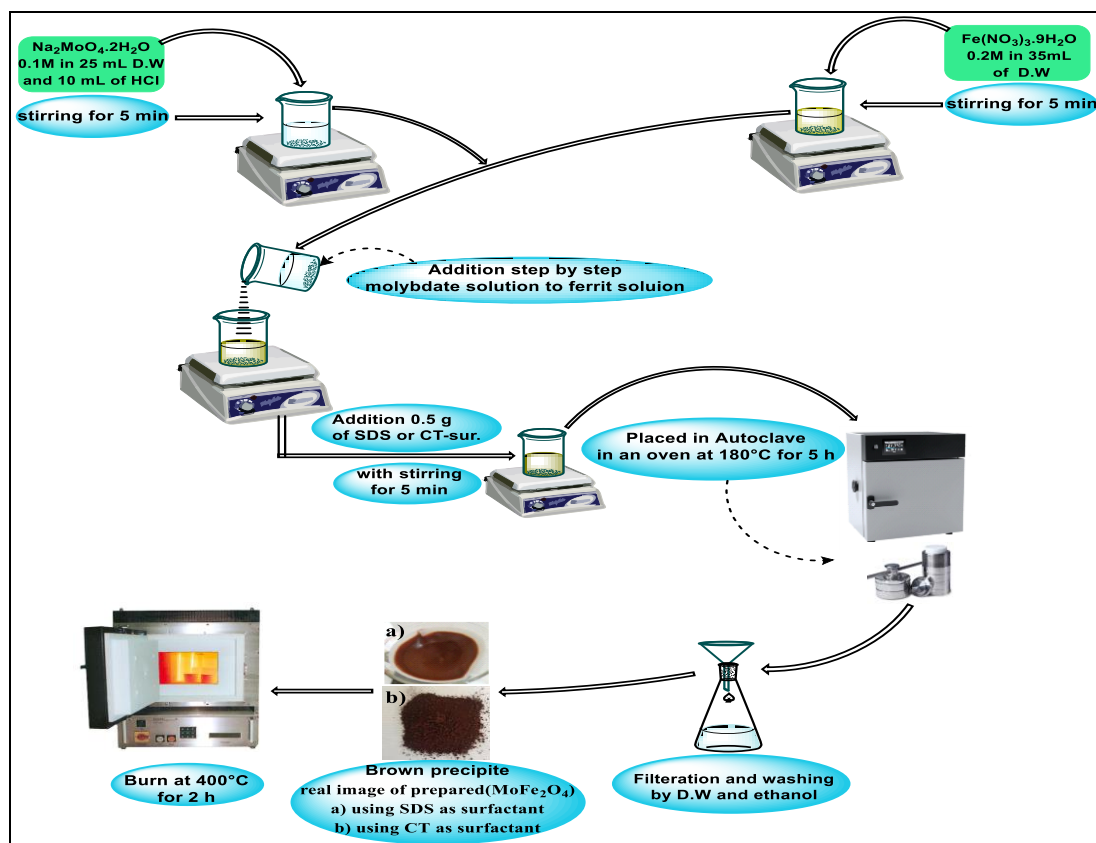


Figure (2-2). Schematic digram of Molybdenum Ferrite nanoparticles synthesis in presence positive and negative surfactant by hydrothermal method.

This precipitate was light thrown and brown in precence SDS and CT, to dry using silica gel inside a desiccator overnight. The MoFe_2O_4 sample was finally obtained after grinding the dry precipitate to a uniform powder. The steps of MoFe_2O_4 synthesis using the hydrothermal method. The proposed method for utilizing a surfactant during the production of molybdenum ferrite.

2.5. Synthesis of Nanocomposites

The 1:2 ratio was prepared from MoFe_2O_4 : Al_2O_3 nanocomposites in the presence of CT and SDS-surfactant, as w/w ratio using ultrasonic wave separately. The MoFe_2O_4 solution and Al_2O_3 solution were dispersed for 2h at 75 °C using ultrasonic waves at 65 kHz. The MoFe_2O_4 solution was gradually added to the Al_2O_3 solution and went on for 2h at 75 °C to perform the binding

process between MoFe_2O_4 and Al_2O_3 . The precipitate that brown light with CT-surfactant and brown dark with SDS-surfactant of nanocomposites was filtered and washed with water and ethanol, then stored overnight in a desiccator. The steps of the composite are explained in Figure (2-4). According to equation 2-3, the suggested chemical equation for the binding of MoFe_2O_4 with Al_2O_3 nanoparticles was obtained:

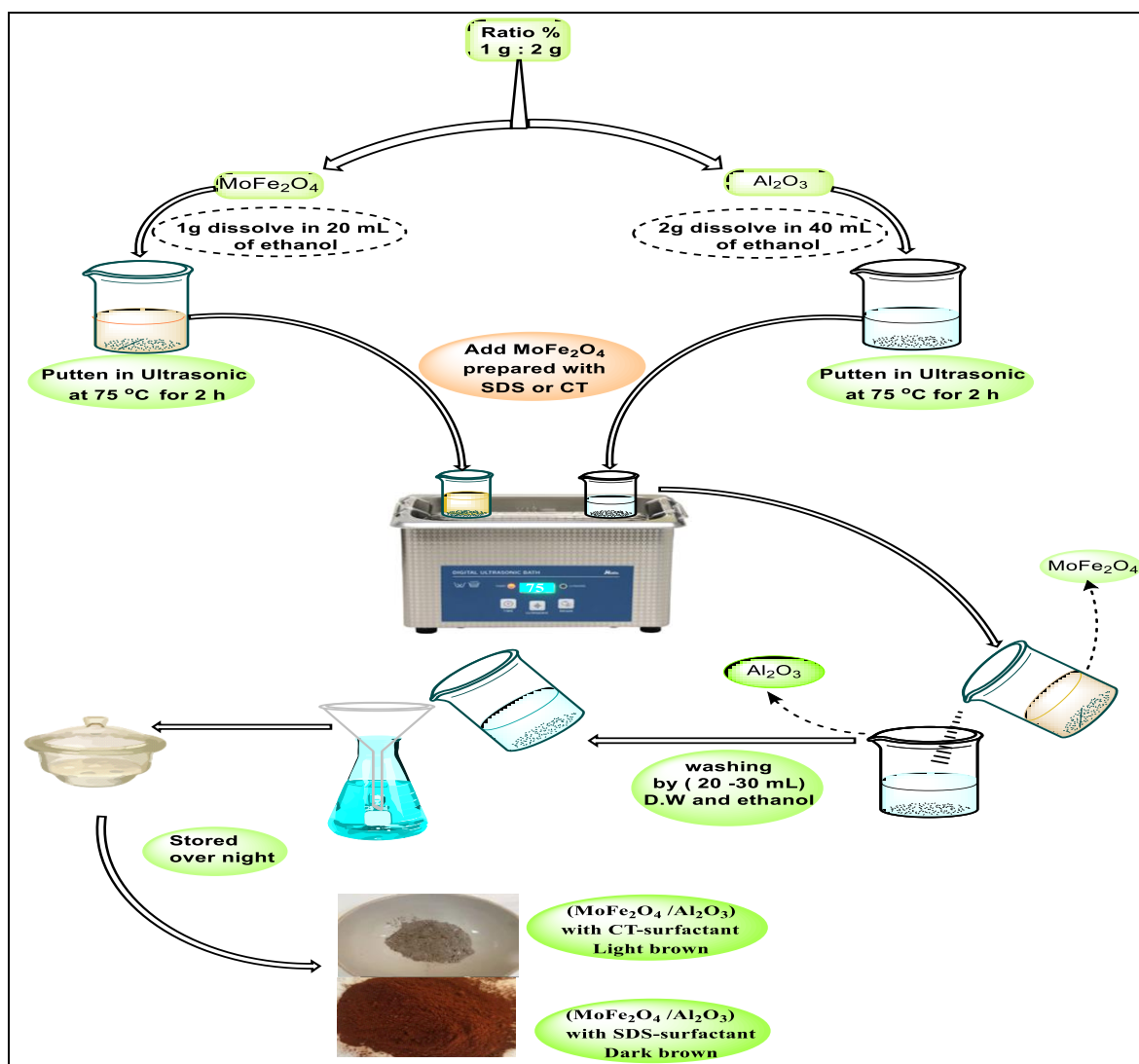
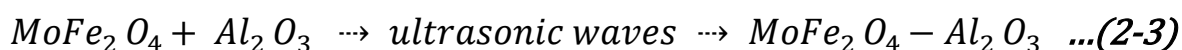


Figure (2-3). Schematic diagram for the Nanocomposites Synthesis steps.

2.6. Characterization of Synthesized Nanophotocatalyst

2.6.1. FT-IR Spectral Analysis

The FT-IR spectral of Synthesized Nanophotocatalyst samples the CsI powder is used to obtain in the range (250 - 4000 cm^{-1}) utilizing (FT-IR Spectroscopy, Shimadzu).

2.6.2. XRD Analysis

An X-ray diffraction (XRD) pattern is widely used to determine the crystalline form of Synthesized Nanophotocatalysts, which are primarily inorganic solid materials that are typically crystals [100]. XRD is considered to be a good method for determining the properties of crystal substances and their constituent parts, whether in the form of a thin coating of crystal or powder. The strength of a diffracted beam, which depends on how much of the corresponding crystalline substance is present, affects how well Scherrer's equation may be used, to use the XRD data, calculate the mean crystallite size (D) [2],[3].

$$D = \frac{k \lambda}{\beta \cos \theta} \quad \dots (2 - 4)$$

Here: k is the dimensionless Scherrer shape constant (used in the range of 0.89-0.94), λ is the wavelength of Cu k α (used in the range of 0.15406 nm), β is the intensity width of the full half-maximum (FWHM), This must be changed to radians by multiplying by ($\pi/180$), and 2θ is the Bragg diffraction angle.

2.6.3. HR-SEM (High-Resolution Scanning Electron Microscopy) Studies

High-resolution scanning electron microscope (HR-SEM) analysis (FEI Nova Nano SEM 450 FESEM-USA) was used to analyze the nanostructure and surface morphology of a prepared MoFe_2O_4 , nano-composite surfaces (Nanocomposites) samples, and synthesis Al_2O_3 .

2.6.4. Energy Dispersive X-ray (EDX) Analysis

By using energy dispersive X-ray (EDX) analysis, the elemental and percentage element compositions of the as-synthesized MoFe_2O_4 , Al_2O_3 , and nanocomposites were validated.

2.6.5. Bandgap energy measurements

Direct and indirect band gap energy was measured in (eV) for all Synthesized Nanophotocatalyst samples using a UV-visible spectrophotometer to determine the absorbance coefficient (α) from absorbance (A) and thickness (I) for all samples using the equation (2-5). Using the Tauc equation (2-6) [4,5].

$$\alpha = (2.3026 A)/(I) \quad \dots (2 - 5)$$

$$\alpha h\nu^m = k(h\nu - E_g) \quad \dots (2 - 6)$$

Where the Planck's constant, h , is equal (6.63×10^{-34} J sec), the light frequency, ν , is equal to (C/λ), here, where C , is the speed of light, which is $2.998 \times 10^8 \text{ ms}^{-1}$, A is the optical constant, and m is always equal to 1/2 in a direct transition and 2 in an indirect transition.

2.7. Determination of zero Point charge(pH_{zpc})

The pH of zero point charge(pH_{zpc}) was determined for all samples. The titration method was adopted, and the technique was an easy method to determine the pH_{zpc} of the studied materials. The data of pH_{zpc} of the Synthesized Nanophotocatalysts give information about the attraction and repulsion between catalysts and dye. Titration was carried out using 0.3 g of prepared Synthesized Nanophotocatalyst sample powder with 100 mL from three different ionic strengths solutions (0.001, 0.01 and 0.1 M KCl). The solution by N_2 was purged into the system to expel CO_2 contamination for 30

minutes. The initial pH was determined using a pH meter before addition. The KOH titrant solution was used to carry out the titration by adding 1mL every 3 min, using the three concentrations (0.1, 0.01, and 0.001M) to change the ionic strength of solutions in the presence of the Synthesized Nanophotocatalysts prepared separately. The values of the change in the pH after using this solution were measured. The process of adding the KOH is repeated until the change in the pH value is stable, as shown in figure (2-5). After the completion of the titration process, The zero point charge (zpc) was determined by locating the common point of intersection of the titration ionic strength curves at different pH [105].

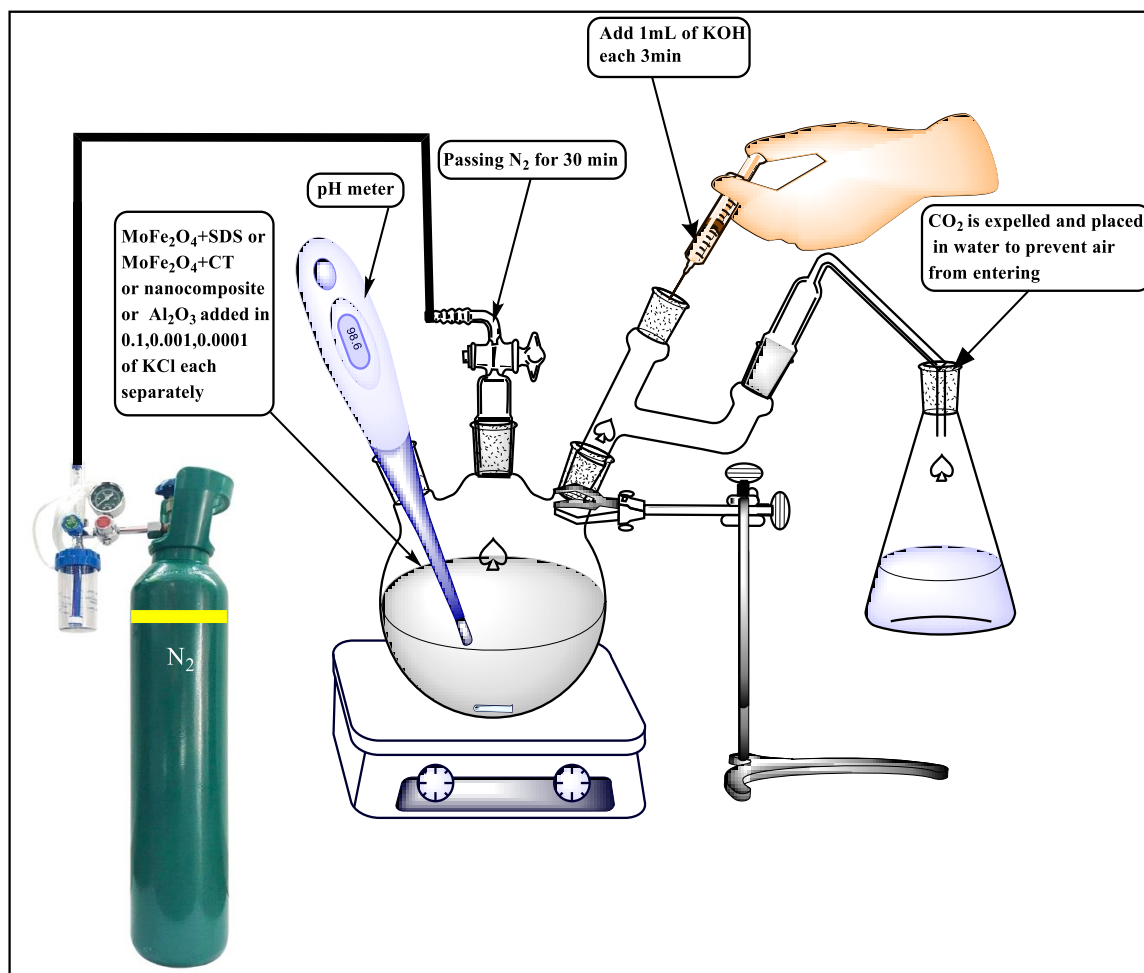


Figure (2-5) Schematic diagram for steps of determining the point of zero charge of Synthesized Nanophotocatalyst samples.

2.8. The calibration curve of Indigo Carmine IC dye

To create the calibration curve, a series of standard indigo carmine IC dye solution solutions ranging from 1 to 50 ppm were prepared. At the wavelength (600 nm), the absorbance of these concentrations was measured. Data from Tables (2-3) demonstrated a relationship between concentration and absorption, as explained in Figure (2-6).

Table (2-3). Indigo Carmine IC dye calibration curve data

<i>C/ppm</i>	<i>Abs.</i>
1	0.0847
5	0.2383
10	0.4561
20	0.9153
30	1.3438
40	1.6519
50	1.9652

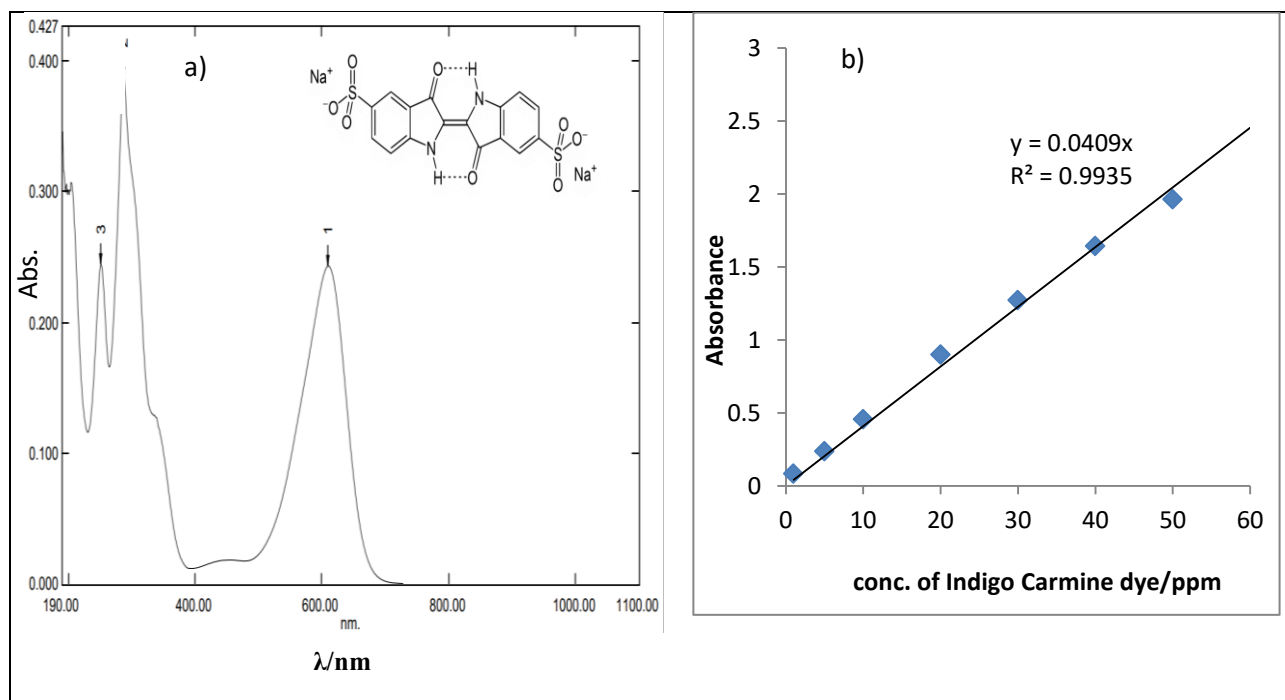


Figure (2-6). (a) Spectrum of UV-visible absorption for indigo carmine IC dye (b) Calibration curve of Indigo Carmine at various dye concentrations at 1-50 ppm.

2.9. Photocatalytic de-colorization reaction of Indigo Carmine IC dye

The exam the activity of Synthesized Nanophotocatalysts (MoFe_2O_4 , Nanocomposites and synthesis (Al_2O_3) materials, the photo reaction was performed using the homemade photo-reactors unit , as shown in figure (2-1). UV-A irradiation source in the photo-reactors unit was used a high-pressure mercury lamp (400W, $\lambda = 365 \text{ nm}$) in these experiments. 100 mL of 25 ppm from Indigo Carmine dye solution was mixed with synthesized nanophotocatalysts. The solution produced required 15 minutes of magnetic stirring to reach an equilibrium adsorption state. Periodically, the produced was exposed to UV-A light with light intensity equal to $3.195 \times 10^{-7} \text{ enstine s}^{-1}$. After that, 3 mL aliquots were taken out every 10 minutes for up to 100 minutes of irradiation intervals. Centrifuging the obtained twice for 15 minutes at 4000

rpm was used to remove all fine Synthesized Nanophotocatalyst particles. The absorbance of the dye solution was determined at 600 nm Using UV-visible spectroscopy. The residue dye was found depending on the calibration curve in Figure (2-4). The Langmuir-Hinshelwood model may be used to calculate the rate constant of apparent reaction (k_{app}) for low dye concentrations with time intervals (t), based on equation (2-7). The photo-decolorization efficiency of dye was calculated using equation (2-8) [5].

$$\ln \left(\frac{C_0}{C_t} \right) = k_{app}t \quad \dots(2-7)$$

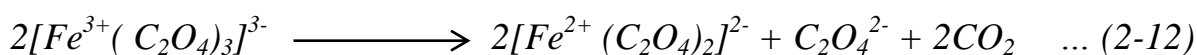
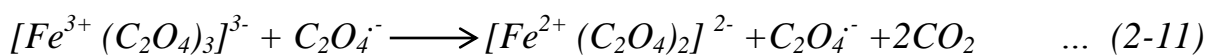
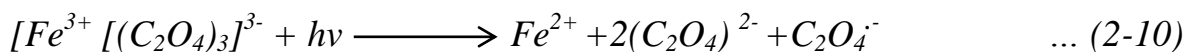
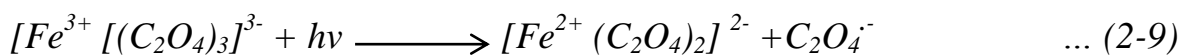
$$PDE \% = \frac{(C_0 - C_t)}{C_0} \times 100 \quad \dots(2-8)$$

Here: C_0 , the initial concentration of IC and C_t , the concentration of IC, after 't' minutes respectively.

2.10. Light Intensity Measurements

The chemical actinometric approach was used to determine the light intensity of the UV-light light source used in this investigation [106]. A precise 100 mL of the actinometric solution was exposed to the UV-A light of the photoreactor. Under the illumination of a UV-A lamp, 40 mL of 0.15 M $Fe_2(SO_4)_3 \cdot H_2O$, 50 mL of 0.45 M $K_2C_2O_4 \cdot H_2O$, and 10 mL of 0.05 M H_2SO_4 were combined under ambient oxygen to make the actinometric solution. The resulting solution, $K_3[Fe(C_2O_4)_3 \cdot H_2O]$ was produced as a yellowish-green color complex after radiation exposure. To evaluate the actinometric complex and gauge the light intensity, 3 mL of the irradiation solution must be centrifuged (4000 rpm in 10 minutes) at regular intervals of (5, 10, and 15) minutes. Exact 0.5 mL of (1%) 1, 10-phenanthroline was added to 2.5 mL of filtered solutions at different times. The reddish-orange complex was obtained and the absorbance can be read at 10 nm.

An explanation of the processes and reactions that occurred is given in the equations that follow [107].



Additionally, the light intensity (I_0) was estimated using the following formulae [108].

$$\text{Moles of } Fe^{2+} = \frac{V_1 \times V_3 \times A_{(510 \text{ nm})}}{V_2 \times l \times \epsilon_{(510 \text{ nm})} \times 10^3} \quad \dots (2-13)$$

$$I_0 = \frac{\text{moles of } Fe^{2+}}{\Phi_\lambda \times t} \quad \dots (2-14)$$

$$I_0 = 3.195 \times 10^{-7} \text{ Einsteine s}^{-1}$$

Where: $V_1 = 100$ mL is the total of irradiation volume, $V_2 = 2.5$ mL is volume of irradiation solution, $V_3 = 3$ mL is a summation of adding the volumes of the irradiation solution (2.5 mL) and the 1, 10-phenanthroline solution (0.5 mL), the length of the optical path (1 cm), A_{510} represents the average absorbance of ferrio-xalate solution after different times of internal irradiation, a mixture of 1,10-phenonethroline, (the molar absorptivity $\epsilon = 1.045 \times 10^4 \text{ L mol}^{-1} \text{ cm}^{-1}$), the quantum yield is ($\Phi_\lambda = 1.2$), and (t) is the time irradiation average (10 min).

2.11. Activation Energy

The Arrhenius equation was used to calculate the apparent activation energy (E_a) of photocatalytic de-colorization of the photoreaction. The apparent activation energy of the photo decolorization process of IC dye was calculated using the graph's linear to the Arrhenius Equation (2-15) [109].

$$\ln k_{app} = \frac{-E_a}{RT} + \ln A \quad \dots(2-15)$$

Where: R is a constant gas equal to $8.314 \text{ J mol}^{-1} \text{ K}^{-1}$, k_{app} is an apparent constant rate, T is the temperature of the reaction, and A is a frequency constant.

2.12. Thermodynamic Parameters

The thermodynamic parameters can affect the kind and direction of this photoreaction. It was discovered using the Eyring-Polanyi equation equation (2-16) [110], and the Gibbs equation (2-17) are used for calculate the values of change enthalpy (ΔH^\ddagger), change entropy (ΔS^\ddagger), and free energy (ΔG^\ddagger), respectively[111].

$$\ln \left(\frac{k_{app}}{T} \right) = \frac{-\Delta H^\ddagger}{RT} + \left(\ln \left(\frac{k_B}{h} \right) + \frac{\Delta S^\ddagger}{R} \right) \quad \dots (2 - 16)$$

$$\Delta G^\ddagger = \Delta H^\ddagger - T\Delta S^\ddagger \quad \dots (2 - 17)$$

In this equation, k_{app} is the apparent rate constant, T is the reaction's temperature, k_B is the Boltzmann constant, which is equal to $(1.382 \times 10^{-23} \text{ J K}^{-1})$, R is the gas constant, which is equal to $(8.314 \text{ J mol}^{-1} \cdot \text{K}^{-1})$, and h is the Plank constant, which is equal to $(6.63 \times 10^{-34} \text{ J.s})$.

2.13. The quantum yield

The quantum yield is a measure of the photocatalytic reaction's efficiency and is based on how many molecules of the probe dye disintegrate for each photon that is absorbed [112], [113]. The following equation may be used to determine the quantum yield (Φ) in the presence of a UV-A lamp: k_{app} (in sec^{-1}) of the pseudo-first-order of the photodecolorization of the Indigo Carmine (IC) dye with light intensity (I_0) $_{\lambda}$ incident light intensity at specific wave length in Enstine $\text{L}^{-1} \text{s}^{-1}$ [114], [115].

$$\Phi = \frac{k_{app}}{2.303 I_0 \varepsilon l} \quad \dots (2 - 18)$$

Here: ε is the molar absorptivity of Indigo Carmine (IC) dye ($84.469 \text{ mol}^{-1} \text{ L cm}^{-1}$) and l is the path length term of the cell (cm).

CHAPTER THREE

Results and Discussion

3.1. Synthesis of synthesized Nanometrials

After using hydrothermal method to synthesize of two spinel MoFe_2O_4 nanophotocatalysts one in presence of positive surfactant (CT) and other in presence negative surfactant (SDS) and given brown and light brown powder respectively, the nanocomposites were synthesis by combined them with alumina using indirect ultrasinic waves. The charecterizations such as FT-IR, XRD, SEM, EDX, ZPC, and Bg can be invistgated to prove the synthesis of these nanophotocatalysts are really happend.

The step of adding the surfactant during the hydrothermal technique is essential because it acts as a stabilizer agent, a template and capping agent at the same time, preventing the hydrolysis of metal by water and ensuring that MoFe_2O_4 Nanoparticles morphology develops uniformly. Additionally, the surfactant is crucial to ensuring that the produced nano-compound is stabilized during the storage procedure[102], [116].

3.2. Characterization Synthesized Nanophotocatalysts

There are many important analysis can be perfomed.

3.2.1. FT-IR Spectra of Synthesized Nanophotocatalysts

In order to analysis the samples and gain an understanding of chemical bonds, FT-IR analysis was performed. The measured spectral span ranged from 250 to 4000 cm^{-1} . The FT-IR spectra of MoFe_2O_4 Nanoparticles the presence of the SDS-Surfactant, Al_2O_3 synthesis, and Nanocomposites nanocomposites , are shown in Figures (3-1 to 3-3). The observed peak at 1624.12 cm^{-1} is related to the Mo-O-Mo stretching vibration of molybdenum molecules, as well as the peak at 3429.55 cm^{-1} is attributed to the O-H stretching vibration due to the adsorption of H_2O from the environment [117], [118]. The vibrational bands between 705.97 and 837.13 cm^{-1} were stretching vibrations of the Mo-O bonds at nonequivalent tetrahedral positions, and vibrational bands in the region

435.93 to 478.36 cm^{-1} were attributable to the FeO_6 octahedra. Moreover, the weak and narrow band at 1114.89 cm^{-1} were assigned to Fe-O-Mo [119].

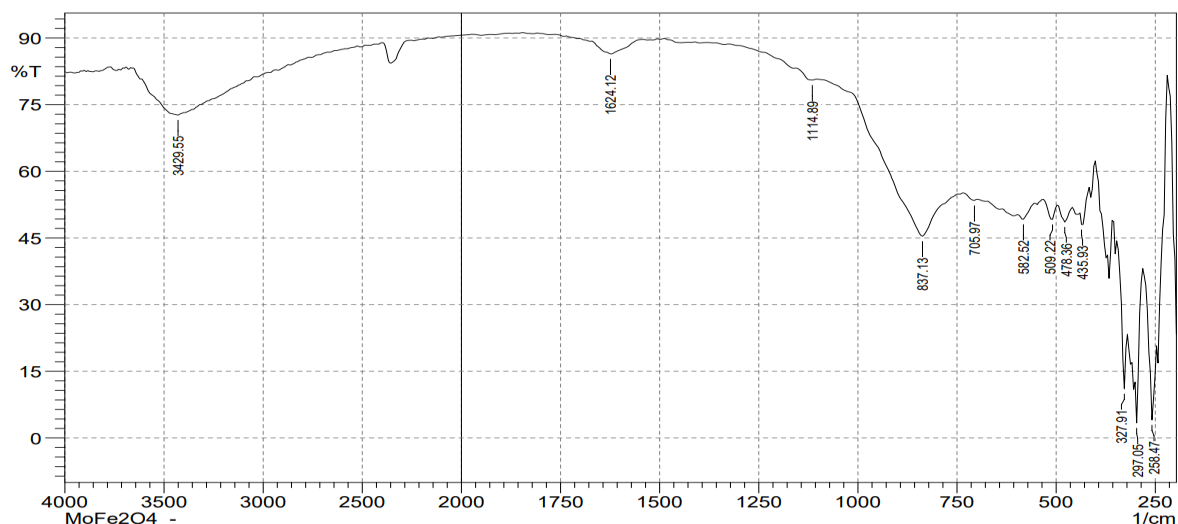


Figure (3-1). FT-IR spectrum of the spinal MoFe_2O_4 Nanoparticles in presence the SDS-Surfactant.

Figure (3-2) explains the spectrum of synthesis Al_2O_3 , Al-O-Al stretching vibrations can be attributed to the peaks at 644.25 and 678.97 cm^{-1} . Al-O-Al bending is responsible for the band at 597.95 cm^{-1} [120], and Al-O also displayed a band nearly at 1150 cm^{-1} , were resulted from non-bridging Al-O terminal group [121].

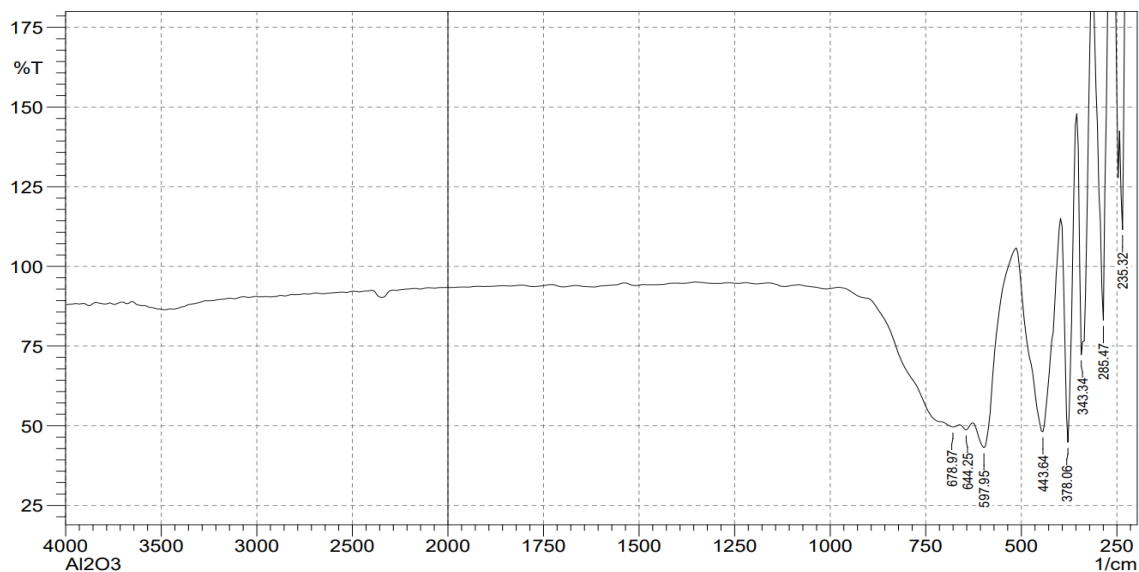


Figure (3-2). FT-IR spectrum of Al₂O₃ synthesis.

FT-IR analysis was used to identify the different bonds present in the Nanocomposites, based on the vibrational transition of bonds figure (3-3). In Nanocomposites, the peak denoting (Metal-Oxides) for Mo-O, Al-O, and Fe-O, Al-O are noted at 594.10 to 648.10 cm⁻¹ and 447.50 cm⁻¹ respectively [93] [122]. The wide peak observed at 1620.26 cm⁻¹ was ascribed to stretching Al-O, were resulted from the non-bridging Al-O terminal group. However, Low wavenumber peaks were caused by the M-O bond [121].

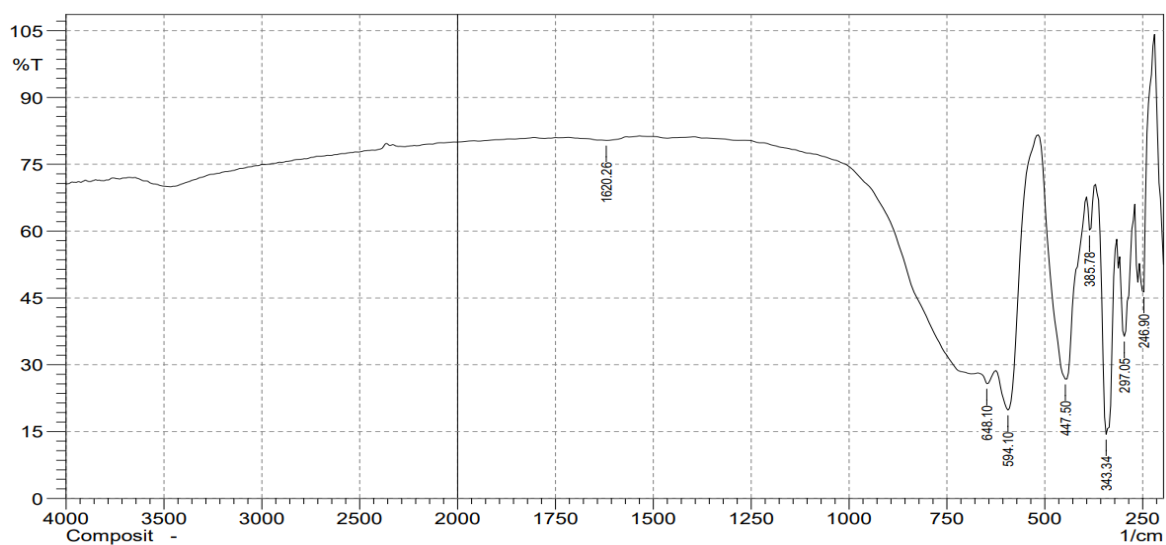


Figure (3-3). FT-IR spectrum of Nanocomposites in presence the SDS-Surfactant.

Figure (3-4), the FT-IR analysis was used to investigate the surface structure and gain insights into chemical bonds. The recorded spectrum range was (4000–250) cm^{-1} . Displays the FT-IR spectrum of MoFe_2O_4 . The distinctive band at 3291 cm^{-1} can be attributed to the stretching of the O-H band caused by the nanoparticles' surface hydroxyl group. The vibration band located at 2226.38 cm^{-1} is evidence for the C–H stretching of carbon, which was formed by the carbon residues at the material surfaces that had arisen from the combustion process. The strong and broadband peaks that were positioned around (850–842) cm^{-1} can be assigned to the tetrahedral species of Mo in MoFe_2O_4 . The vibration band, which pointed in the (816–860 cm^{-1}) area, revealed the presence of the Mo-O-Mo bond [123].

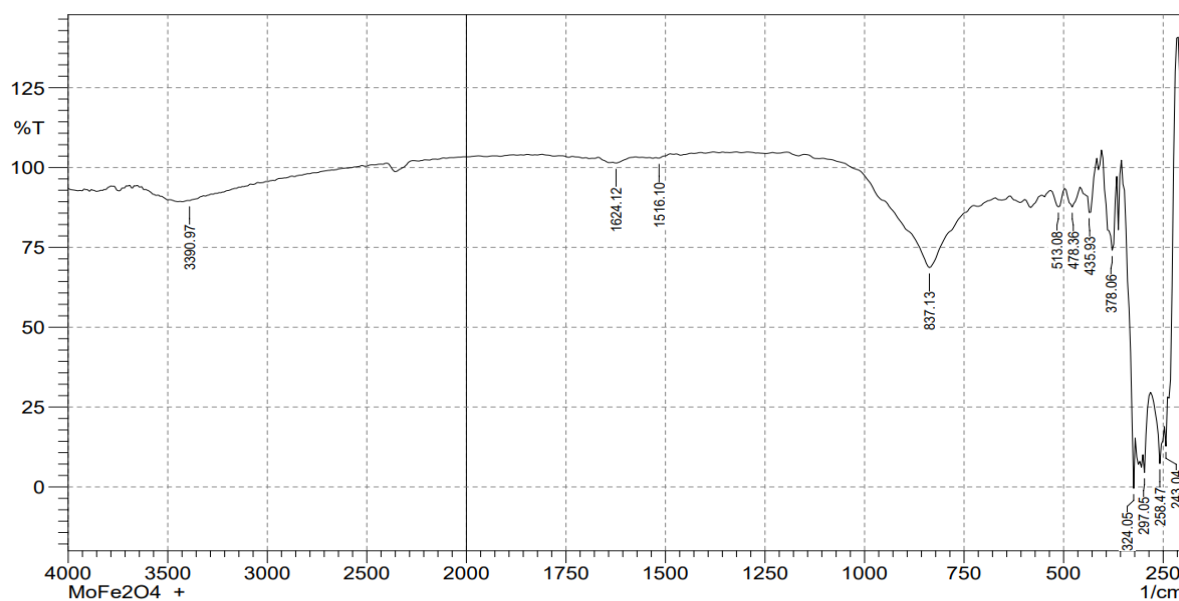


Figure (3-4). FT-IR spectrum of the spinal MoFe_2O_4 Nanoparticles in presence the CT-Surfactant.

Figure (3-5) shows the FT-IR spectra of Nanocomposites in the presence CT-Surfactant. The coupling relationship between oxygen and molybdenum was confirmed by the vibration band at a distance of 824.14 cm^{-1} . The Mo-O asymmetrical stretching band was discovered at 541.53 cm^{-1} . The weak band at (456–486 cm^{-1}) is caused by the Fe-O-Mo stretching vibration mode [124]. Also,

a weak adsorption band around 722 cm^{-1} is related to the Al–O bond [125]. Table (3-1) shows how the vibration bands are assigned together with their wavenumber.

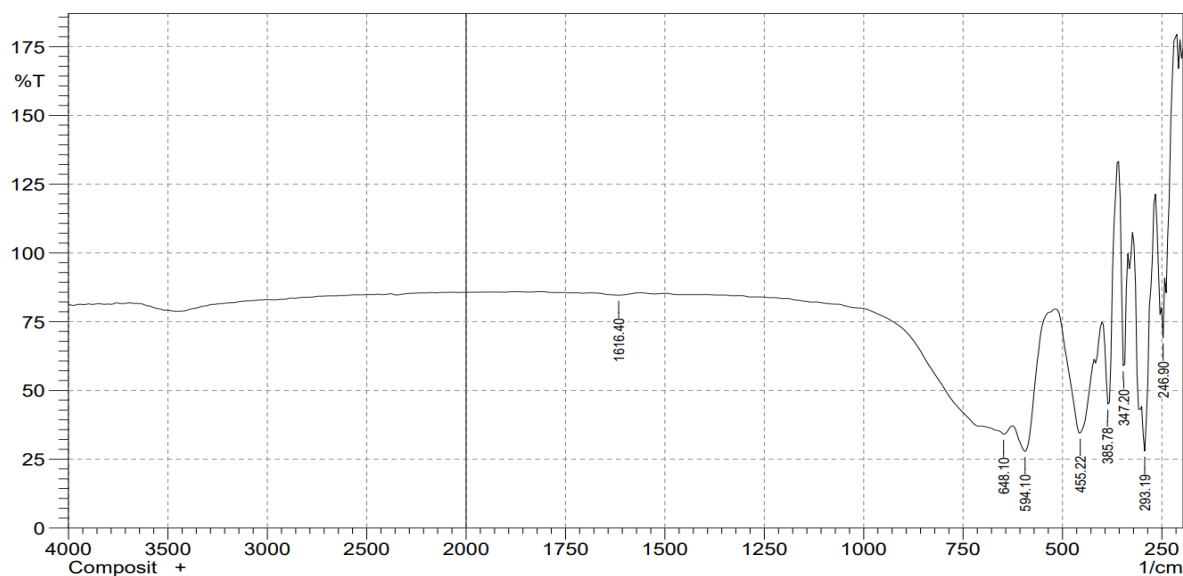


Figure (3-5). FT-IR spectrum of Nanocomposites in presence the CT-Surfactant.

Table(3-1). FT-IR spectra are used to assign bands and their corresponding wavenumbers.

FT-IR (cm^{-1})	Corresponding bands
456 - 486	Fe–O–Mo stretching vibration
594.1 - 648.1	O–Al–O stretching
541.5	Mo–O Asymmetrical Stretching in MoO_4
824.1	Coupling bond between oxygen and molybdenum (O–Mo)
816 - 860	Mo–O–Mo bond
850 - 842	Tetrahedral species of Mo in MoFe_2O_4
2226.3	C–H stretching
3293.1	O–H stretching
293.19 - 385.78	Fe–O–Fe bonding

3.2.2. X-ray diffraction Patterns (XRD) analysis

Synthesized Nanophotocatalysts require the proper crystal structure, and XRD is one of the finest methods for assessing a crystal's molecular structure. According to Figure (3-6), all synthesis and synthetic samples of MoFe_2O_4 , Nanocomposites, and Al_2O_3 underwent XRD analysis.

The XRD spectra of the Synthesized Nanophotocatalyst samples, the three samples show the different diffraction characteristics clearly shows the appearance of several patterns related to its basic components, where observed the presence of peaks located at 14.127° , 15.403° , 16.554° , 19.589° , 20.541° , 21.851° , 22.966° , 25.806° , 27.579° , 30.288° and 34.118° which are attributed to the indexed plants (210), (003), (020), (31-2), (311), (022), (202), (022), (212), (122) and (042) respectively, proving the formation of the and can be well-indexed to the monoclinic structure of molybdenum ferrite, these results are in line with (JCPDS card No. 83-1701) [96]. And, the intensities of the XRD patterns suggested that the sample was highly crystalline. No other diffraction peaks were observed, which shows the high purity of the as-prepared MoFe_2O_4 in the presence SDS-Surfactant.

The synthesis of the Al_2O_3 phase is supported by the observed diffraction peaks at 25.606° , 35.176° , 37.799° , 43.377° , 52.567° , 57.516° , and 68.22° , which are connected to the (311), (400), (511), (440), (444), (731), and (840) reflections, respectively. The samples' whole range of diffraction peaks agrees with the data from data (JCPDS card 10-0425) [126].

When the MoFe_2O_4 and Al_2O_3 upon incorporated as a nanocomposites, some crucial peaks are moved the high 2θ from 21.851° MoFe_2O_4 and 25.606° Al_2O_3 to 25.724° as nanocomposites, from 22.966° MoFe_2O_4 , 35.176° Al_2O_3 to 35.282° also 27.579° of MoFe_2O_4 , and 43.377° of Al_2O_3 shifted to 43.486° for nanocomposites. However, the very high peak intensity suggests that the material is highly crystalline. The mean size of the MoFe_2O_4 in the presence the SDS-Surfactant, Al_2O_3 , Nanocomposites crystals was calculated using the

Scherrer equation (2-4) with the (202), (022) and (212). (400), (440) and (731). (202), (440), and (731) respectively peaks [127], [128]. Scherrer's equation (2-3) was used to determine the mean crystallite sizes (L) in nm based on the XRD data, the mean size of MoFe_2O_4 in the presence the SDS-Surfactant was about 23.83 nm, while the size of Al_2O_3 and Nanocomposites was about 43.44 nm and 47.84 nm respectively. The increase in the size of the nanocomposites crystals is attributed to the successful combination of alumina with molybdenum ferrite in the presence of SDS surfactant.

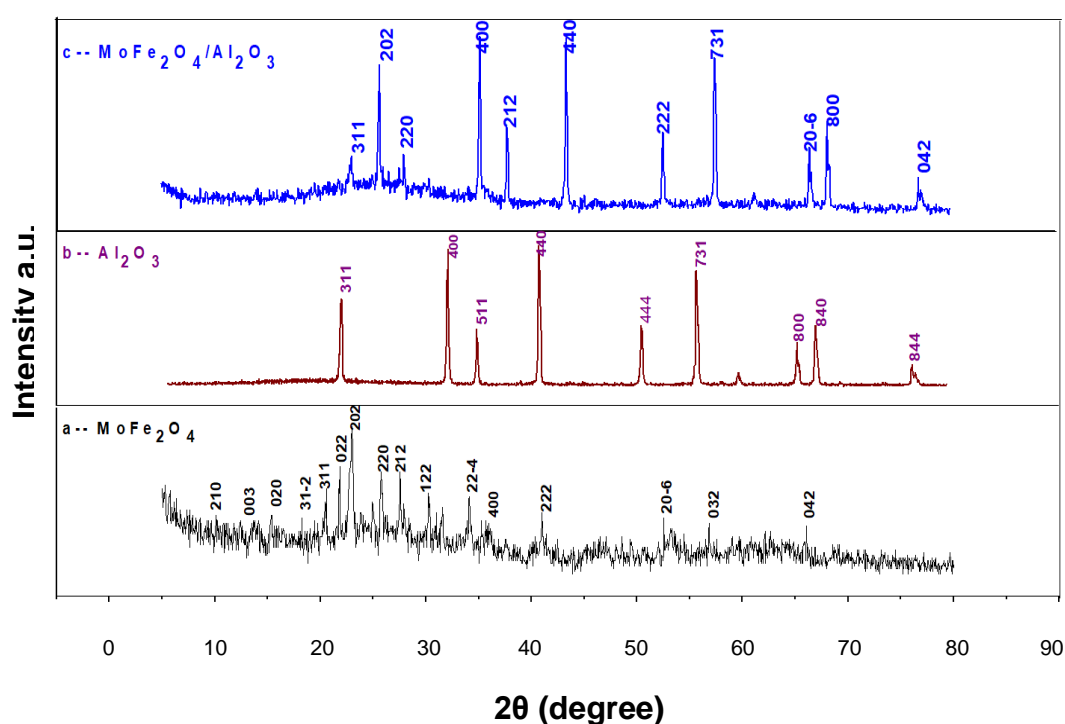


Figure (3-6). XRD pattern of (a) MoFe_2O_4 (b) Al_2O_3 (c) Nanocomposites prepared in presence the SDS-Surfactant.

After indexing, it was discovered that the crystalline peaks were in good accord with the standard monoclinic structure of MoFe_2O_4 [129], [130]. Figure (3-7), the essential diffraction peaks of monoclinic MoFe_2O_4 appear at $2\theta = 18.36^\circ, 18.91^\circ, 19.60^\circ, 20.56^\circ, 21.20^\circ, 21.86^\circ, 23.01^\circ, 25.79^\circ$ and 27.54° , with miller indicates (200), (220), (-123), (212), (122), (-105), (224), (400) and (503) respectively, the stronger intensity at 2θ for 23.01, 25.79, and 27.54 of the reflection peaks of (224), (400) and (503) which is in good agreement with the

literature values (JCPDS 35-0183) [126]. However, the Al_2O_3 peaks appear at diffractions (311), (400), (511), (440), (444), (731) and (800) with 2θ positions are 35.17° , 43.37° , 52.56° , 57.51° , 66.53° , 68.22° and 76.88° respectively, These results are consistent with the typical diffraction data (JCPDS card 10-0425) [31]. When the MoFe_2O_4 and Al_2O_3 upon incorporation as a nanocomposites, some crucial peaks are moved the high 2θ from 23.01° MoFe_2O_4 and 43.37° Al_2O_3 to 43.52° , from 52.56° Al_2O_3 to 52.71° , from 25.79° MoFe_2O_4 to 27.54° [131]. The very high peak intensity suggests that the material is highly crystalline. This shift in the position of peaks indicates to metallic bond form and incorporates MoFe_2O_4 with Al_2O_3 as a Nanocomposites composite.

The average crystallite size of the MoFe_2O_4 , Al_2O_3 , and Nanocomposites samples was calculated using the Debye Scherrer formula given in Eq. (2-4). [127], [132]. The average crystallite sizes of MoFe_2O_4 particles, synthesis Al_2O_3 , and Nanocomposites as a nanocomposites were found to be 23.97 nm, 43.44 nm, and 47.41 nm respectively. The value of the lattice parameter depends on the disparity between the ionic radii of Fe^{3+} and Mo^{5+} ions. While the octahedral ionic radius of Mo^{5+} ions (0.61 Å) is larger than the octahedral ionic radius of Fe^{3+} ions (0.55 Å) and Al^{3+} (0.535 Å), Mo^{5+} ions' tetrahedral ionic radius (0.46 Å) is smaller than that of Fe^{3+} ions and Al^{3+} [36]. That mentality causes a metallic bond to form between two metals.

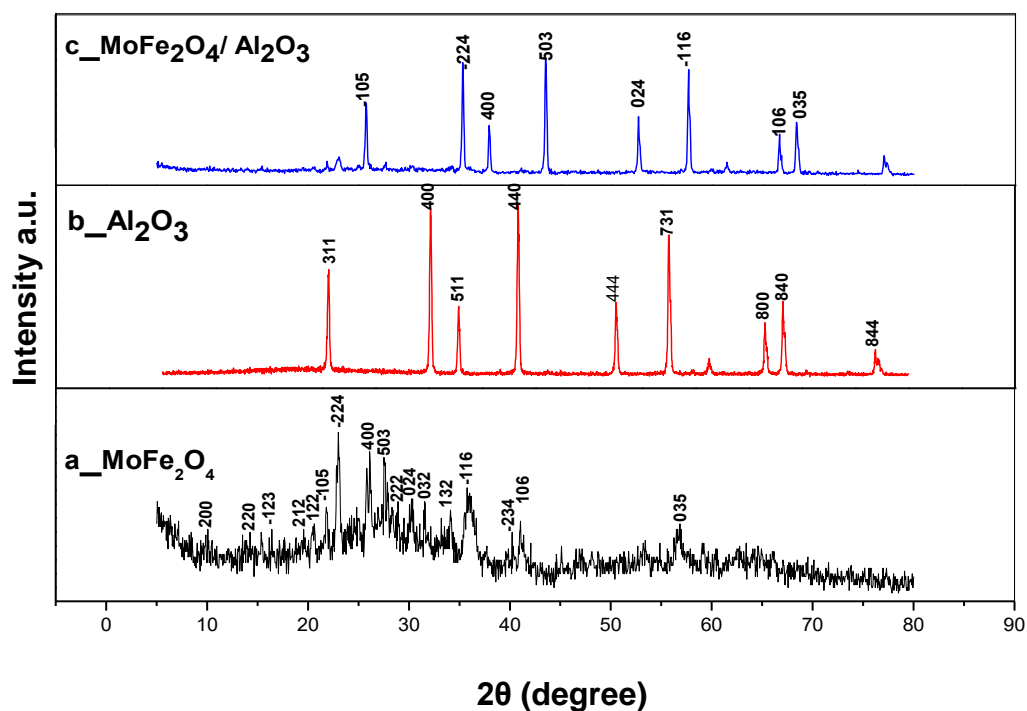


Figure (3-7). XRD pattern of (a) $MoFe_2O_4$ (b) Al_2O_3 (c) Nanocomposites prepared in presence the CT-Surfactant.

3.2.3. SEM Analysis

The scanning electron microscope (SEM) has long been the preferred technology for determining the surface shape and fundamental physical characteristics of materials. This technique determines the particle shape and size distribution of the substance. The spinel $MoFe_2O_4$, Al_2O_3 , and Nanocomposites composite SEM spectra were used, to examine the surface morphology of the materials. The $MoFe_2O_4$ with the presence SDS-Surfactant sample in Figure (3-8) shows a compressed order of homogenous nanoparticles with a form that is approximately spherical granules and has aggregated into a like-caviar nanoparticle structure.

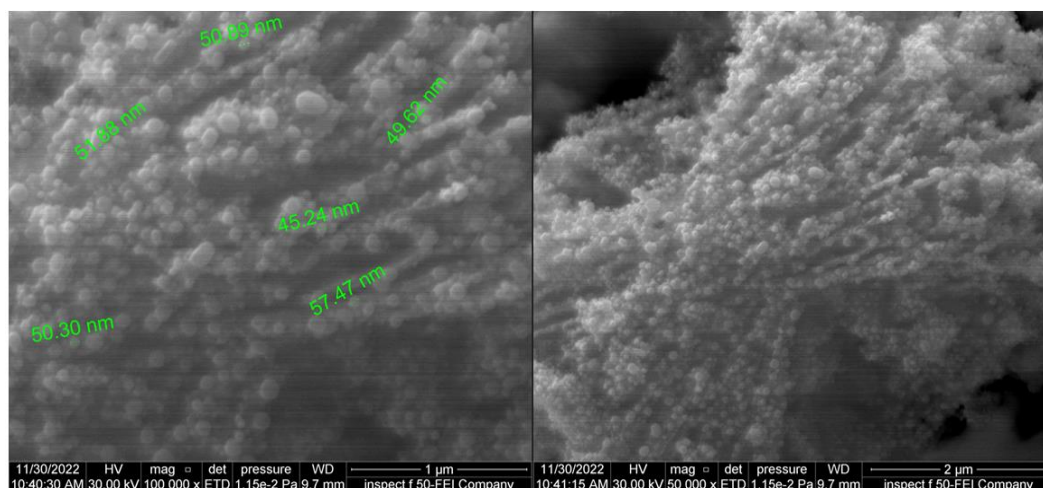


Figure (3-8). SEM Images of MoFe₂O₄ nanoparticles in presence the SDS-Surfactant.

The particle size is 50.9 nm, which is more significant than the average crystal size [133], [134]. As a result of the majority of particles being constructed as polycrystalline. This effect might be explained by the nanoparticles' tiny size and high density [127]. The MoFe₂O₄ nanoparticles are described as proof that the structure is polycrystalline.

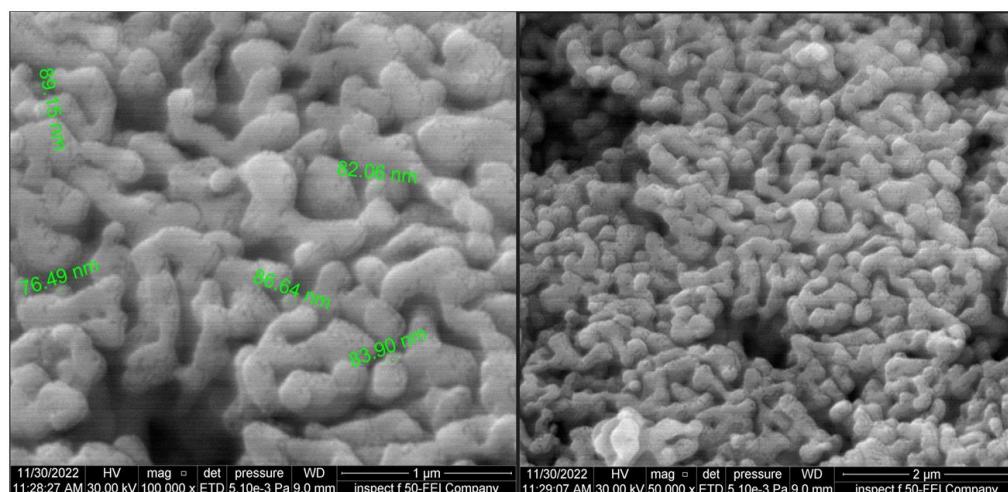


Figure (3-9). SEM Images of synthesis Al₂O₃.

In figures (3-9) and (3-10) the Al₂O₃, had the appearance of brain cells, and the MoFe₂O₄ when it is coupled with Al₂O₃ appeared highly agglomerated sub-micron sized particles with nanograin-like secondary particles on the surface,

because of the high proportion of Al_2O_3 in comparison to spinel MoFe_2O_4 , which is used to make spinel MoFe_2O_4 more lightweight during the Synthesis of the nanocomposites, they can act as a Synthesized Nanophotocatalyst to improve their optical characteristics. The spheres average 83.64 nm, for Al_2O_3 and Nanocomposites, is 55.22 nm [133], due to the high percentage of Al_2O_3 in comparison to spinel MoFe_2O_4 , increased the size of nanocomposites, which is employed to make spinel MoFe_2O_4 in presence SDS-surfactant more lightweight when nanocomposites s are created Nanocomposites surfaces Al_2O_3 and Nanocomposites surfaces feature what seems to be a homogeneous distribution of spherical particles with a crystals structure; these spheres have relatively smooth surfaces. MoFe_2O_4 and its composite partial sizes are not subject to the nano-size restrictions that apply to polycrystalline materials.

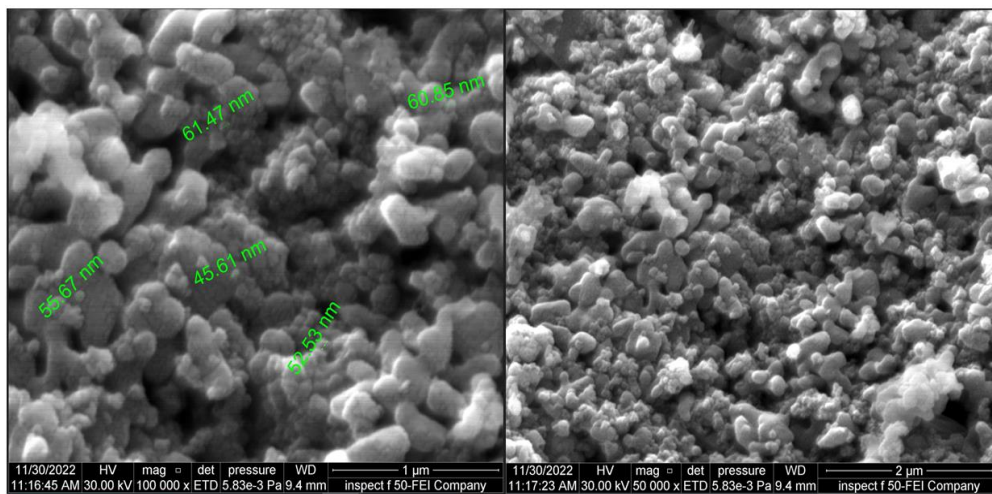


Figure (3-10). SEM Images of Nanocomposites in presence the SDS-Surfactant.

According to figure (3-11) (a,b) for the SEM study, find that the shape of the synthesis MoFe_2O_4 is Nano-plates. While an incorporation of the spinel MoFe_2O_4 with Al_2O_3 the shape resembles a like-Popcorn shape. all samples nanoparticles are aggregated into larger particles and the average particle size of

MoFe₂O₄ Nanoparticles, Al₂O₃, and Nanocomposites was shown the average have the following: (41.81 nm), (45.53 nm), and (83.64 nm) respectively. which leads to an increase in the prepared MoFe₂O₄ particle size in the nanocomposites, which is attributed to the Al₂O₃ big particle size, which ranges from (76.49 – 89.15) nm as shown above in figure (3-9), and Al is more ionic radius than the ionic radius of Mo and Fe [5], [102], [135].

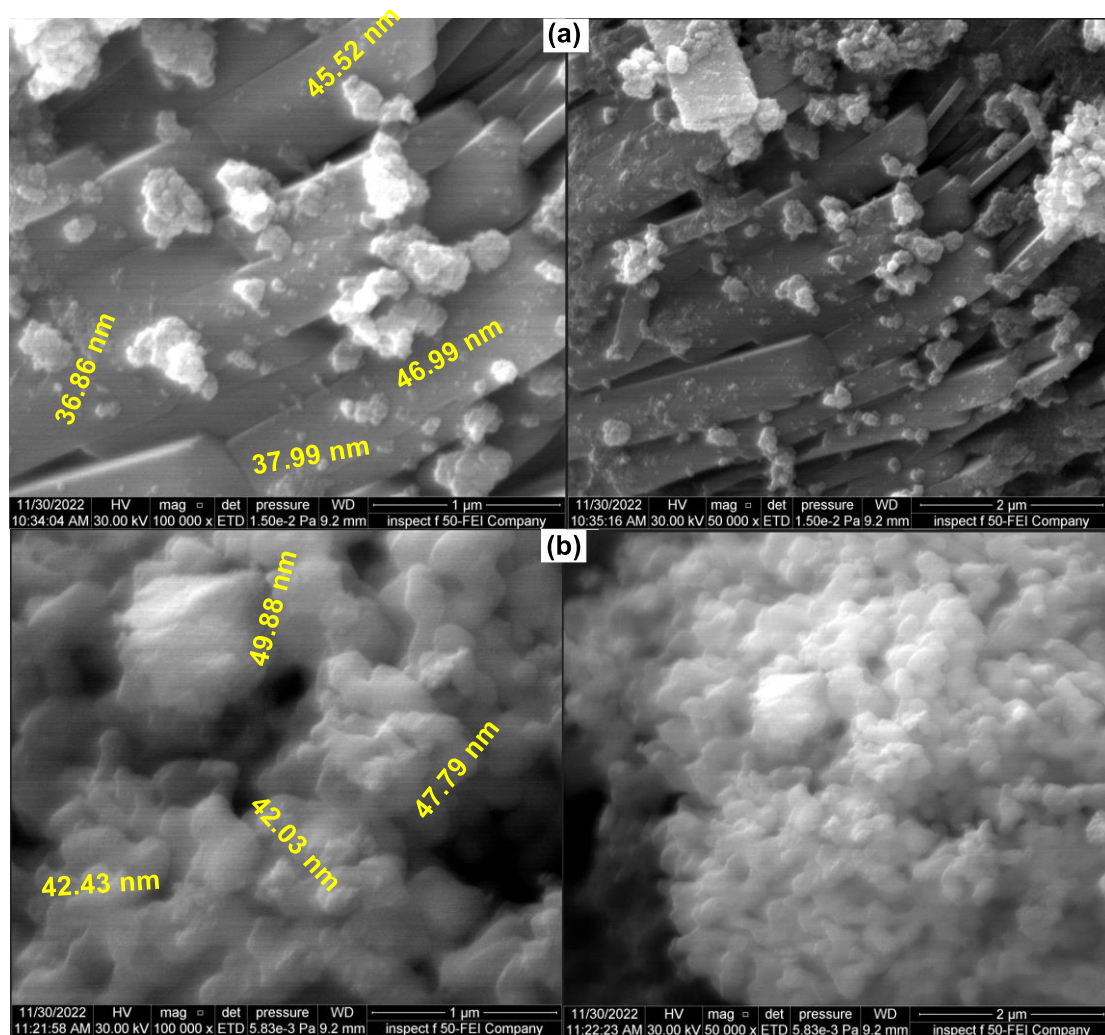
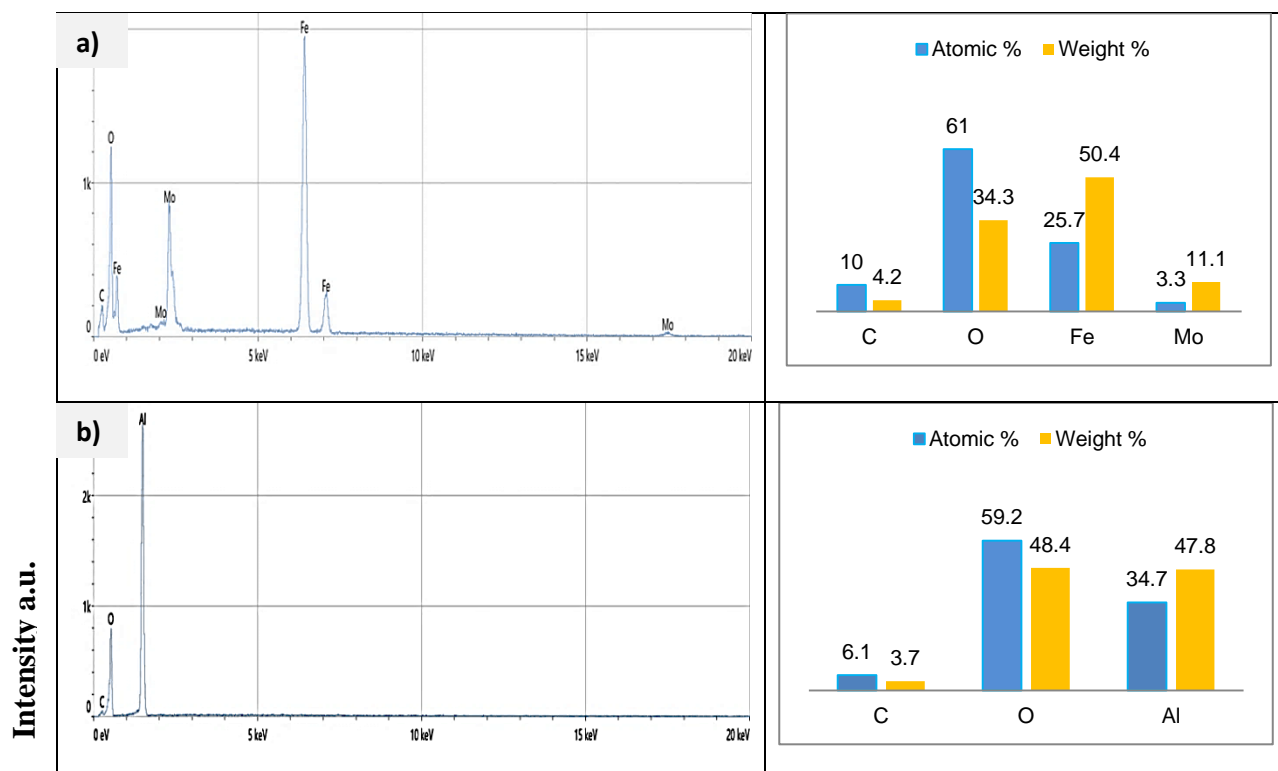


Figure (3-11). SEM images of a) MoFe₂O₄ Nanoparticles b) Nanocomposites in presence the CT-Surfactant.

3.2.4 EDX Analysis

The elemental compositions of the as-synthesized materials were confirmed by energy dispersive X-ray (EDX) analysis MoFe_2O_4 , Al_2O_3 , and nanocomposites with the presence of SDS, CT-surfactants as shown in Figures (3-12) and (3-13) (a-c), respectively. The findings showed that all of the compounds Fe, Mo, Al, and O were present. That demonstrated that MoFe_2O_4 and its nanocomposites were formed without the presence of any contaminants (C serves as a substrate) [136]. The Mo, Fe, Al, and O signals are well-defined, showing the active processing of metal oxides involving iron, molybdenum, and aluminum. The peak strength of Al has grown for samples generated using larger Al precursor ratios, which is in good accord with the Synthesis procedure's stoichiometry Synthesis ratio (2:1) [137].



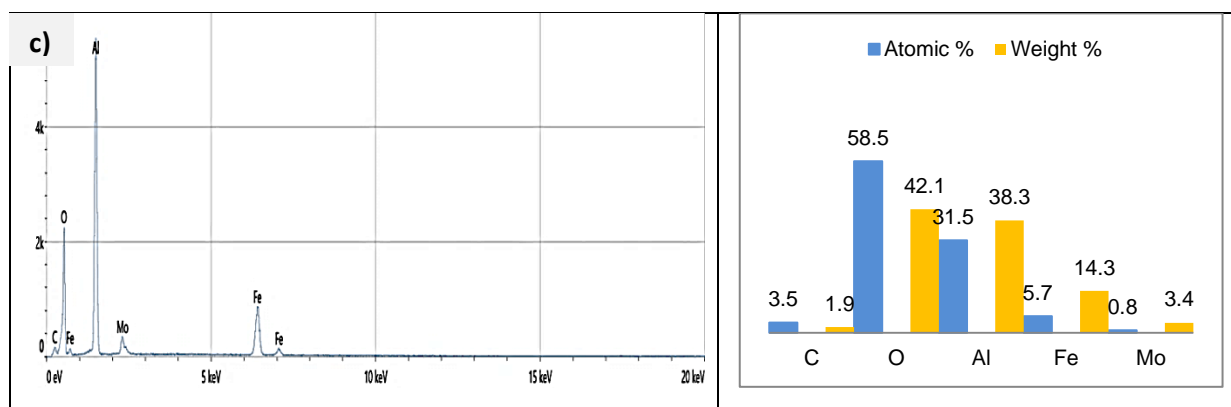


Figure (3-12). EDX spectra of (a) MoFe_2O_4 Nanoparticles, (b) Al_2O_3 and (c) Nanocomposites with presence the SDS-surfactant.

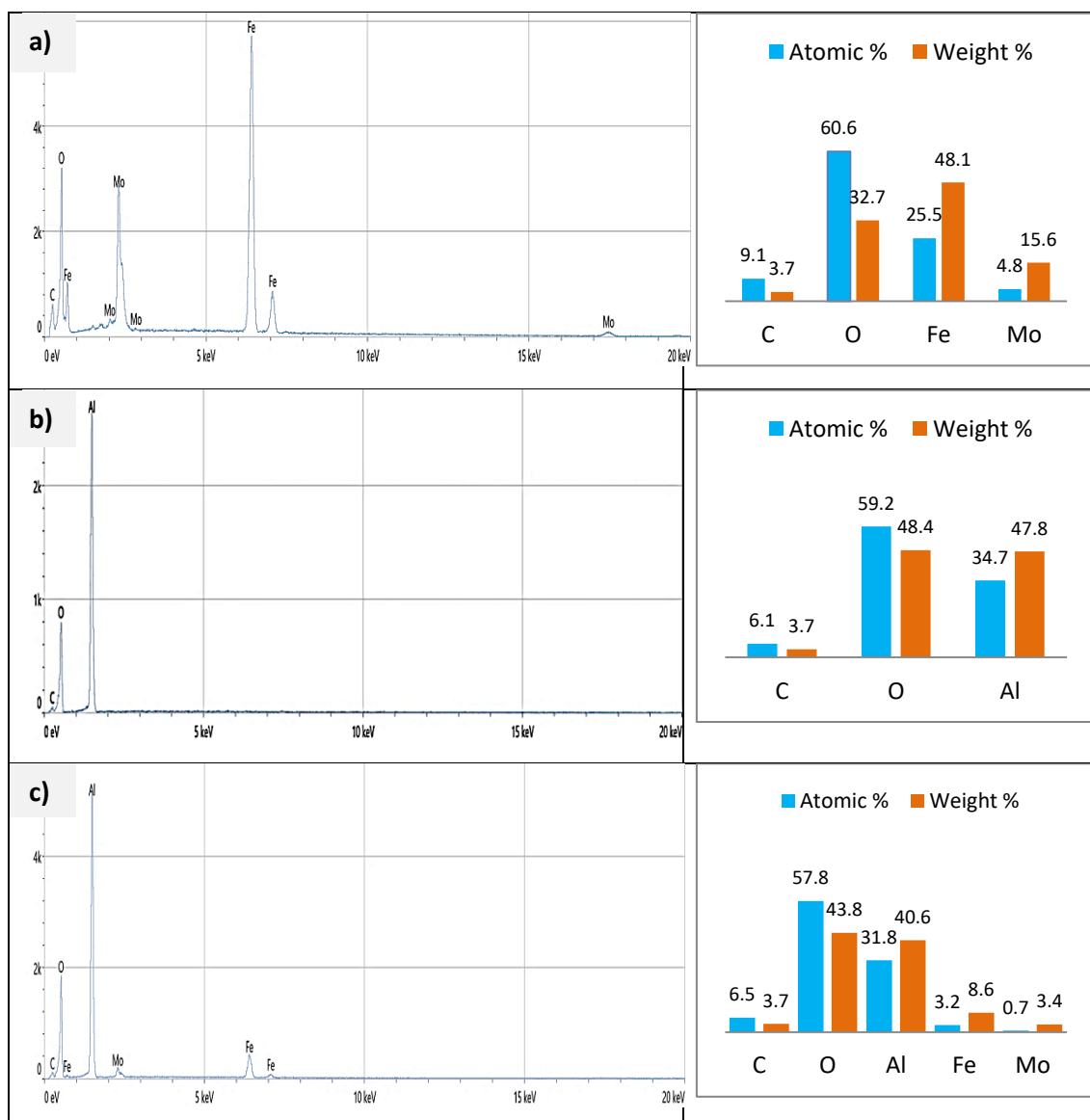


Figure (3-13). EDX spectra of (a) MoFe_2O_4 Nanoparticles, (b) Al_2O_3 and (c) Nanocomposites with presence the CT-surfactant.

3.2.5. Measurement of Band Gap Energy

Based on equations (2-5) and (2-6) of the Tauc system [138], [139], the band gap (E_g) value for each Synthesized Nanophotocatalyst sample was calculated using information regarding the material's potential as a Synthesized Nanophotocatalyst. The plotted Tauc equation in figures (3-14) and (3-15), that observed the band gap for MoFe_2O_4 is direct [129], and equal to 2.78 eV (445.986nm), while it is an indirect band gap for the $\alpha\text{-Al}_2\text{O}_3$, and $\text{MoF}_2\text{O}_4/\text{Al}_2\text{O}_3$ nanocomposites with magnitudes equal to 4.44 eV (279.243nm), and 4.05 eV (306.133nm) respectively, in the presence of CT-surfactant. While in the presence of the SDS-surfactant, the band gap for MoFe_2O_4 is direct is 2.95 (445.986 nm), and Nanocomposites it is an indirect band gap of 3.45 eV (306.133nm) respectively. The coupling $\alpha\text{-Al}_2\text{O}_3$ during the production of a composite is useful due to raising the lightness of spinel MoFe_2O_4 , this vital step to improves, when utilized as a Synthesized Nanophotocatalyst, they retain their optical characteristics. Because the spinel MoFe_2O_4 has a small band gap that may be increase the recombination process the coupling process will decline *via* an increase in the charge separation and increase the hydroxyl radical life [5], [139].

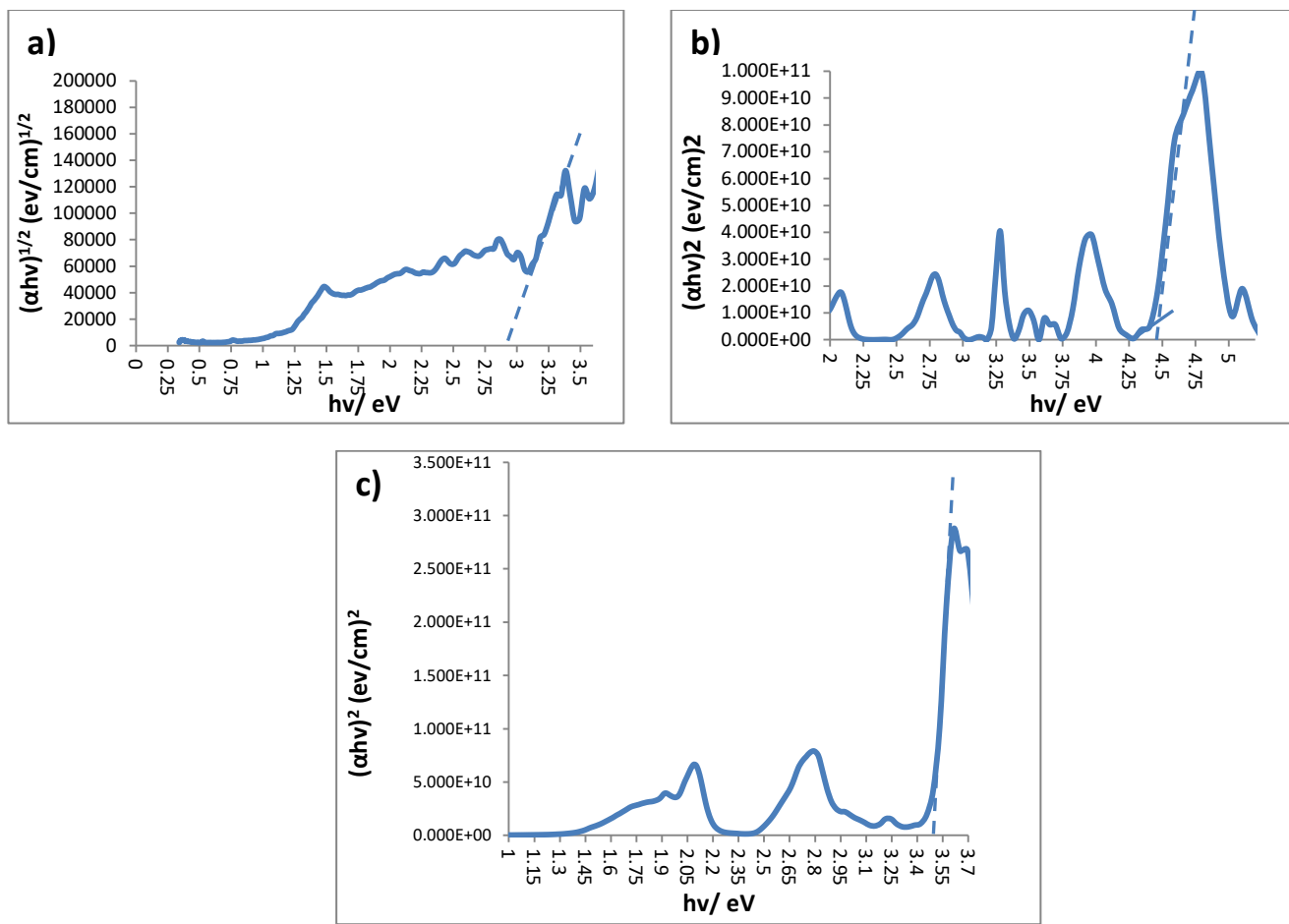
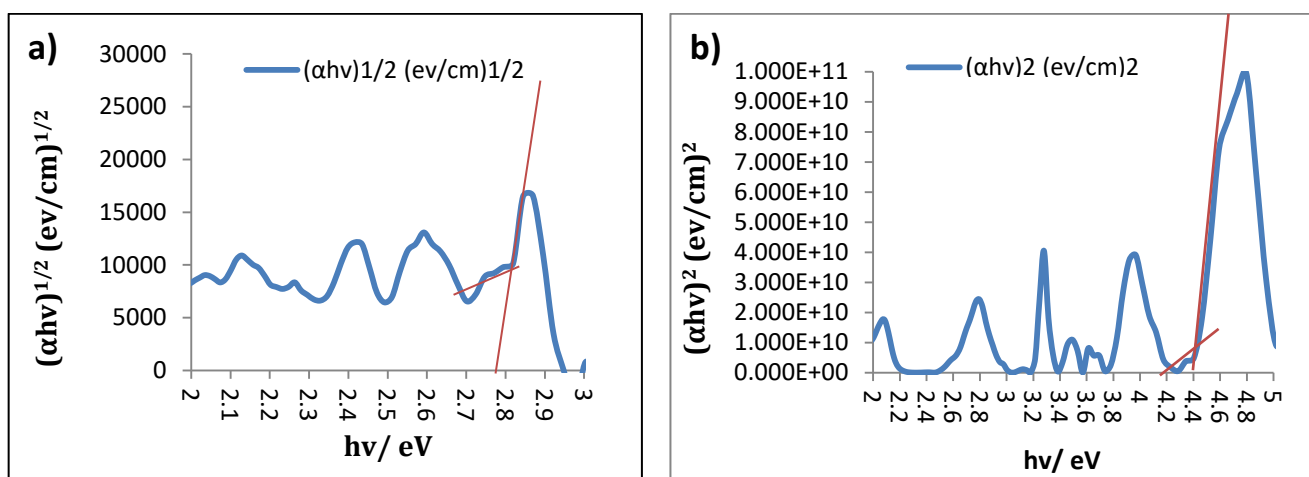


Figure (3-14). The band gap as an direct a) The spinal MoFe_2O_4 Nanoparticles (b) Al_2O_3 Synthesis and (c) Nanocomposites as an indirect in presence the SDS-surfactant.



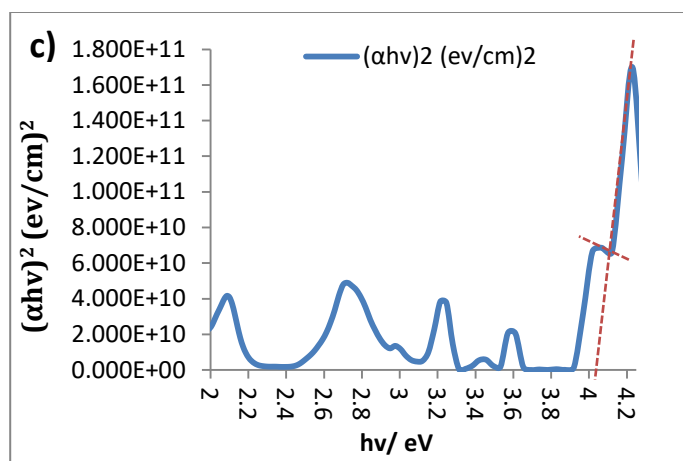


Figure (3-15). The bandgap as an direct a) The spinal MoFe_2O_4 Nanoparticles (b) Al_2O_3 Synthesis and (c) Nanocomposites as an indirect in presence the CT-surfactant.

3.2.6. The pH Point of zero charge (pH_{pzc})

The initial pH of a solution is critical in photocatalytic decolorization because it influences the surface charge of the catalyst. The type of pollutant and the pH zero point charges (pH_{pzc}) are the two factors that have the biggest effects on the optimal pH. The term pH zero point charges (pH_{pzc}), which refers to a situation when the surface is neutrally charged, is used to describe the point where the pH curve and the titration curve cross. Finding the point of zero of the nanocomposites is essential for figuring out how much photocatalysis is occurring at a specific pH. The appropriate pH settings for the photodecolorization process are estimated by the pH_{pzc} data. Since H^+ ions prefer to remain on surfaces at low pH rather than in solutions, MoFe_2O_4 to cationically charged, a property that at low pH will readily adsorb anions. However, at high pH, H^+ ions prefer to be in solution rather than in the material, therefore the anionically charged MoFe_2O_4 surface will readily adsorb cations [140].

Based on table (3-2) and figures (3-16) to (3-17) the pH_{pzc} values 2.9-3.6, 2.3-5.4, and 4.2-5.9 is obtained of MoFe_2O_4 in the presence of SDS,

Nanocomposites, and Al_2O_3 respectively. While the pH_{pzc} of MoFe_2O_4 is equal to 1.6-2.8 and Nanocomposites is 3.2-5.2 in the presence of CT- surfactant. This result shows that MoFe_2O_4 and Nanocomposites have a low pH_{pzc} , which allows them to quickly adsorb the IC dye (an anion dye) [141], [142]. The pH_{pzc} value is used to determine an effective pH for photocatalytic decolorization. The optimum pH is dependent on the kind of pollution and pH_{pzc} . Specifically for anion dyes like indigo carmine, a pH value of 5.3 was found. This demonstrates that although anion dyes have a pH value of < 7 , which is acidic (+), while any cation dyes have a pH value > 7 , which is alkaline (-) [142].

Table (3-2). Estimation of the pH_{pzc} for MoFe_2O_4 Nanoparticles and their nanocomposites in the presence of CT, SDS-surfactant, using simplified "Titration Method"

No.	Samples	(pH_{pzc})	Surfactant
1.	MoFe_2O_4	1.6 - 2.8	Cetrimide (CT)
2.	Nanocomposites	3.2 - 5.2	Cetrimide (CT)
3.	Al_2O_3	4.2- 5.9	Non- Surfactant
4.	MoFe_2O_4	2.9 - 3.6	sodium dodecyl sulfate (SDS)
5.	Nanocomposites	2.3 - 5.4	sodium dodecyl sulfate (SDS)

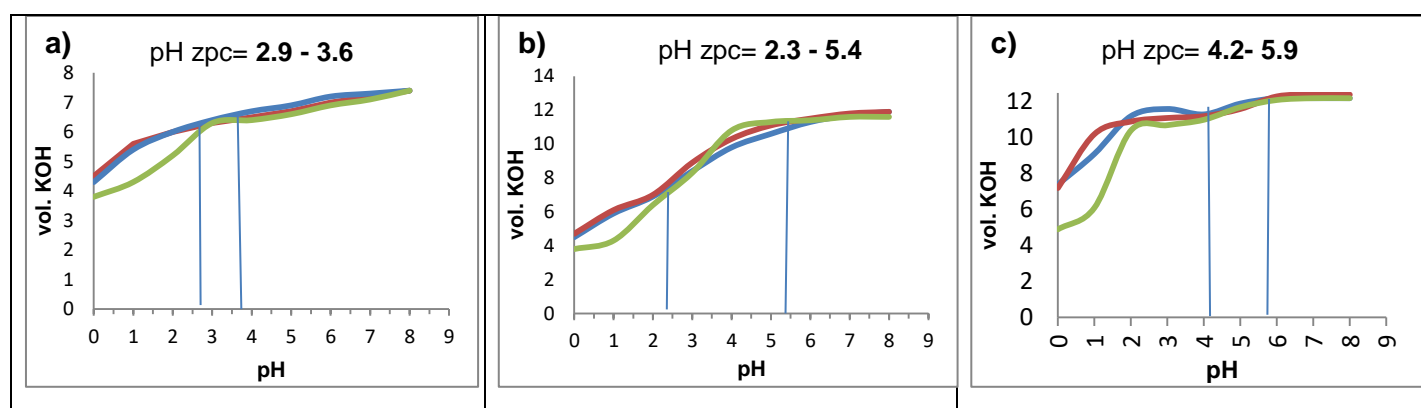


Figure (3-16). The pH_{PZC} of (a) MoFe_2O_4 (b) Nanocomposites (c) Al_2O_3 at different pH values in presence the SDS-surfactant.

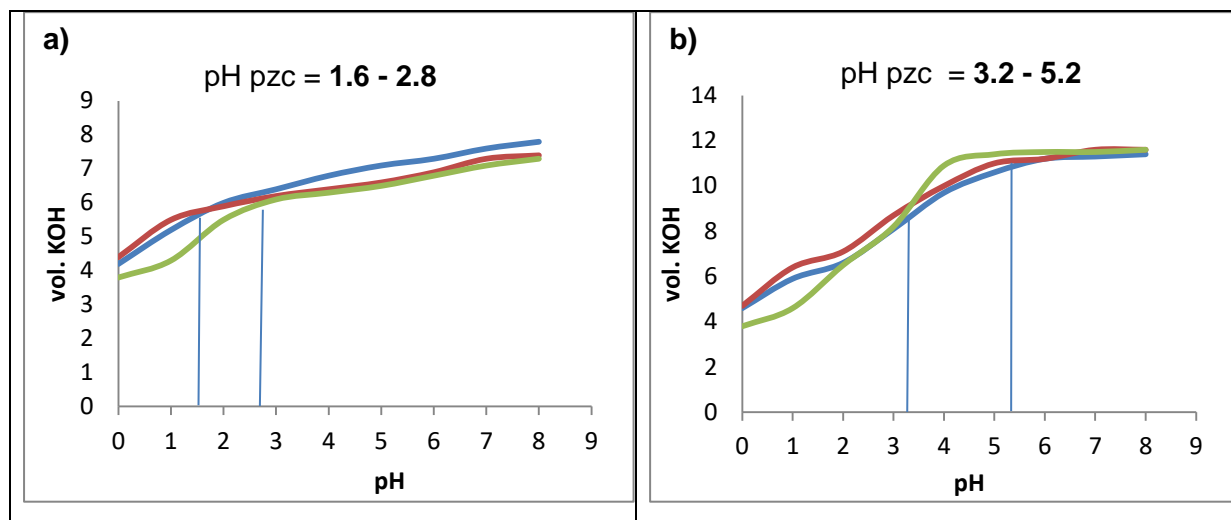


Figure (3-17). The pH_{PZC} of (a) MoFe₂O₄ (b) Nanocomposites at different pH values in presence the CT-surfactant.

3.3. The photocatalytic reaction of Indigo Carmine IC dye

Following the success of the prepared spinel MoFe₂O₄ Nanoparticles, their nanocomposites, and Al₂O₃ synthesis with the presence of SDS, CT-surfactant had been established, these samples were employed to photo-decolorize the Indigo Carmine IC dye. In order to do that, and by taking the amount of weight from the Synthesized Nanophotocatalyst, use it at various temperatures to determine the thermodynamic functions, alter the dye's initial pH to see how that affects the course of the reaction, and calculate the point of zero charge for the surfaces of all samples. All photoreaction studies were conducted with a light intensity of (3.195×10^{-7} Einstein.s⁻¹).

3.3.1. The parameters effect of on photocatalytic reaction of de-colorization of Indigo Carmine IC dye

3.3.1.1 The effect of nanophotocatalyst doses

This effect is vital studied to detect if this work is economy or no. This parameter was performed using 0.05 g, 0.1 g, 0.2g and 0.3 g in 100 mL of 25

ppm of IC dye solution and found the 0.05g is given low responsible because low active site but 0.1 g is demonstrates a best activity. Moreover, the used doses more than 0.1 g of samples are caused low activity also because the screen effect that prevent reach the light to surface of nanophotocatalyst.

3.3.1.2. The effect of Initial pH

1. The effect of initial pH of IC dye solution Nanophotocatalyst Studies with the presence of the CT-surfactant

The effect of initial pH was studied in the following conditions: 25 ppm dye concentration in 100mL at 293.15 K, 0.1 g dose of synthesis Al_2O_3 , spinal MoFe_2O_4 , and Nanocomposites in the presence of the CT and the SDS-surfactant, all at the same light intensity.

Tables (3-3) to (3-8) and figures (3-17) to (3-20) exhibit the findings demonstrate that these photo reactions' efficiency and rate constant rose as the dye's starting pH, which was determined to be 5.3, was raised. This occurs as a result of the acidic composition of the dye increasing the attraction force between the catalyst surface and the dye molecule. Additionally, the amount of hydroxyl radicals $\bullet\text{OH}$ in the solution rises, which results in increased photocatalytic activity throughout the decolorization process [143], [144]. The efficacy of decolorization was found to diminish with an increase in pH between 7 and 9, which indicated that the indigo carmine IC dye cannot decolorize in an alkaline environment.

The initial pH of the solution will typically have an impact on the ionization state, the acid-base property of the Synthesized Nanophotocatalyst surface, and the reactant dye [145], [146]. The lower value of the initial pH of the dye solution (pH = 5.3) gives the maximum decolorization of IC. Because the dye has an acidic nature. The percentages of photo decolorization (PDE) of IC were obtained at 293.15 K for 50 min and equal to 76.47%, 93.27% and 89.91% using spinal MoFe_2O_4 , synthesis Al_2O_3 , Nanocomposites respectively. It can be

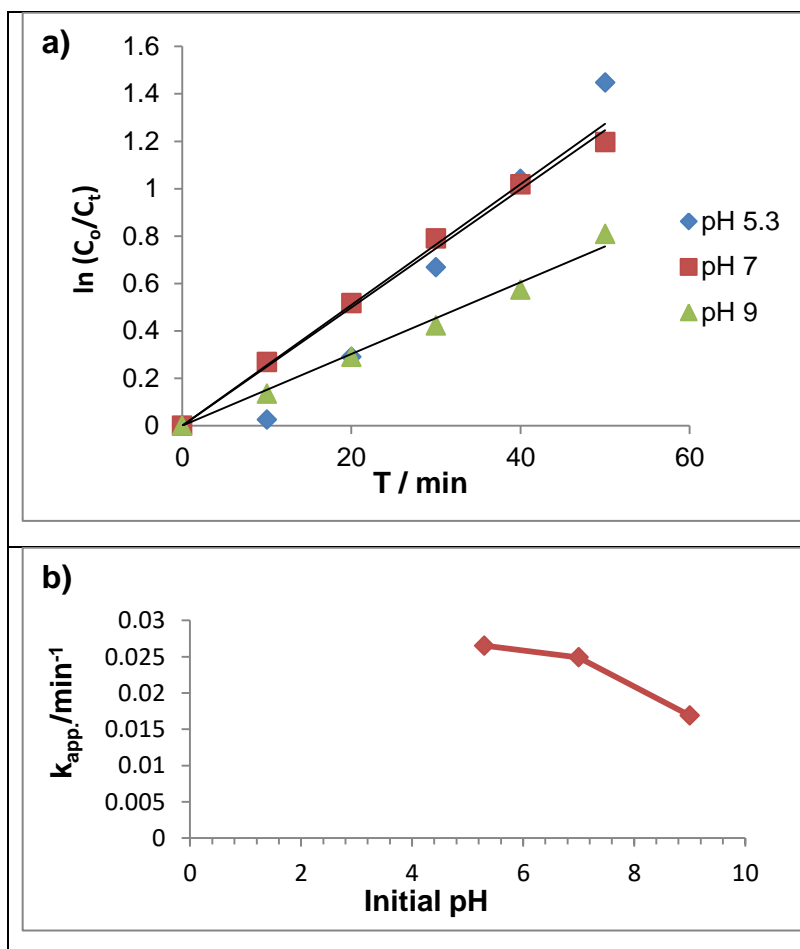
explained by the solid acid characteristics of MoFe_2O_4 , which are proved by both the low point of zero charge (pH_{PZC}) and the presence of strong acid sites. The (pH_{PZC}) of MoFe_2O_4 is 1.6-2.8, beyond this deprotonation occurs and an acidic microenvironment is formed on the surface of MoFe_2O_4 particles [105]. Also, the using of CT as a cationic surfactant gives the best photo decolorization results which is due to the acidity of the dye so the attractive forces will increase on MoFe_2O_4 Nanoparticles, which was prepared in the presence of the CT-surfactant [147]. Moreover, by increasing the pH of the solution, more protons are subtracted from the surface of the MoFe_2O_4 Nanoparticles in the presence of the CT, leading to a more acidic medium. It compensates for the anionic influence due to an increase in solution pH. In this case, the surface of spinal MoFe_2O_4 Nanoparticles in the presence of the CT plays an acid–base buffering role. However, the current study found that when the solution pH is elevated more than 5.3, 7 to 9, the photocatalysis activity appears to decline. The description of a strongly alkaline situation that results from $\cdot\text{OH}$ reduced capacity to oxidize could provide evidence for this occurrence [148].

Table (3-3). The change of the $\ln(C_0/C_t)$ with irradiation time at pH of Indigo Carmine IC dye by MoFe_2O_4 with presence the CT-surfactant

<i>Time</i> (minutes)	<i>pH</i>	<i>ln(C₀/C_t) MoFe₂O₄</i>		
		5.3	7	9
0		0	0	0
10		0.0255	0.2682	0.1347
20		0.2904	0.5164	0.2904
30		0.6682	0.7901	0.4224
40		1.0414	1.0179	0.5744
50		1.4469	1.1956	0.8088
$k_{app} \text{ min}^{-1}$		0.0265	0.0249	0.0169

Table (3-4). The variation of (PDE%) with times Irradiation at different initial pH of Indigo Carmine IC dye by MoFe_2O_4 with the presence the CT-surfactant.

Time (minutes)	pH	PDE% MoF_2O_4		
		5.3	7	9
0		0	0	0
10		2.5210	23.5294	12.6050
20		25.210	30.2520	25.2100
30		48.739	39.4957	34.4537
40		64.705	47.0588	43.6974
50		76.470	63.8655	55.4621



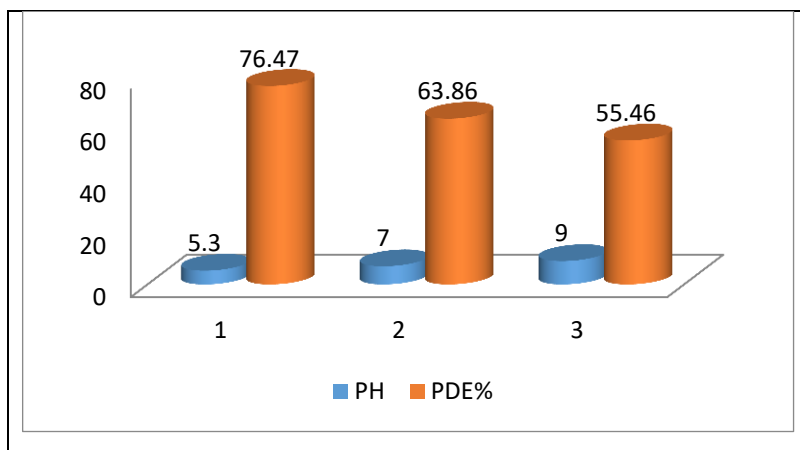


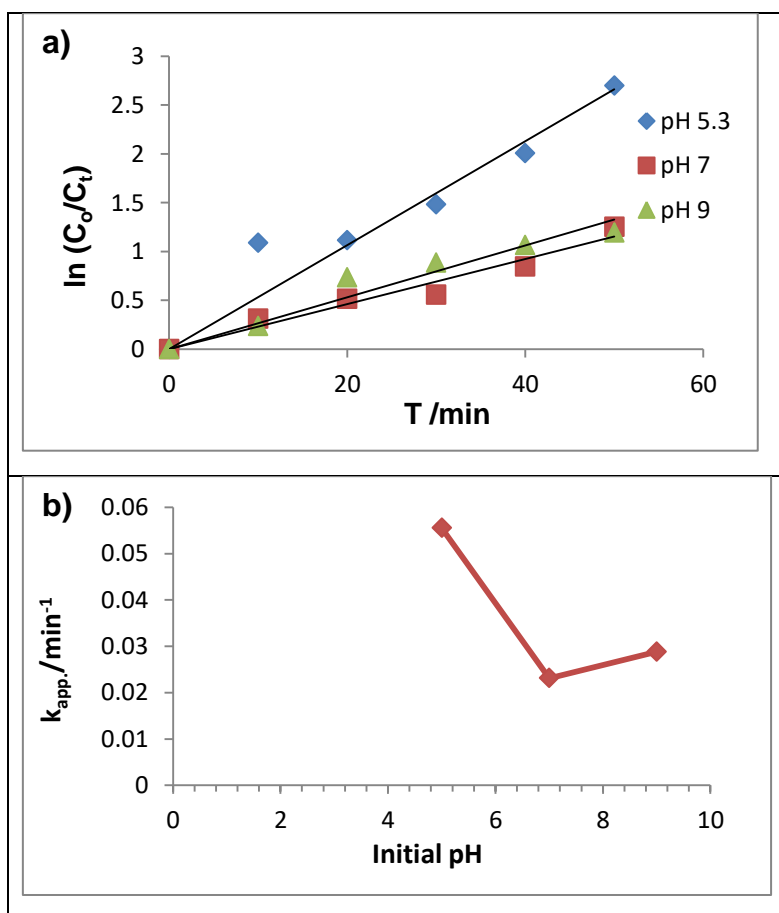
Figure (3-18). (a) The change of the $\ln(C_0/C_t)$ with irradiation time at pH solutions of spinal MoFe_2O_4 , (b) Relationship between the (k_{app}) and the different pH solution of spinal MoFe_2O_4 , (c) Effect the different pH solution of spinal MoFe_2O_4 on (PDE%) with the presence of CT-surfactant.

Table (3-5). The change of the $\ln(C_0/C_t)$ with irradiation time at different initial pH of IC dye by Synthesis Al_2O_3 .

Time (minutes)	pH	$\ln(C_0/C_t)$ Al_2O_3		
		5.3	7	9
0		0	0	0
10		1.0902	0.3132	0.2358
20		1.1155	0.5164	0.7360
30		1.4832	0.5596	0.8873
40		2.0065	0.8472	1.0655
50		2.6996	1.2527	1.1956
	$k_{app} \text{ min}^{-1}$	0.0555	0.0231	0.0288

Table (3-6). The variation of (PDE%) with times Irradiation at different initial pH of IC dye by Synthesis Al_2O_3 .

Time (minutes)	pH	PDE% Al_2O_3		
		5.3	7	9
0		0	0	0
10		66.3865	26.8907	21.0083
20		67.2268	40.3361	52.1008
30		77.3109	42.8571	58.8235
40		86.5546	57.1428	65.5462
50		93.2773	71.4285	69.7478



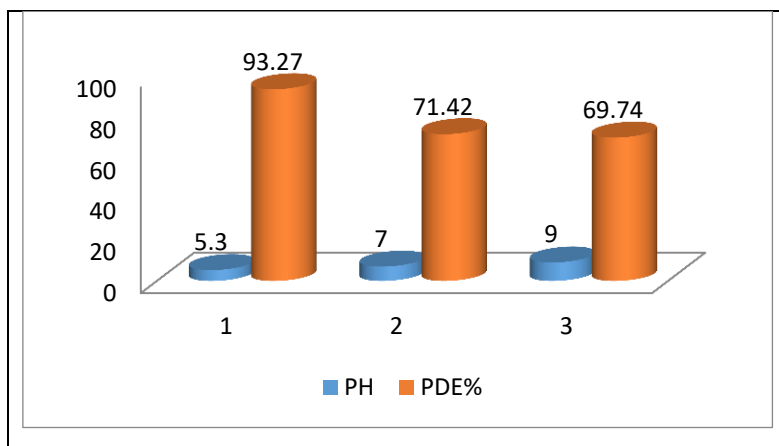


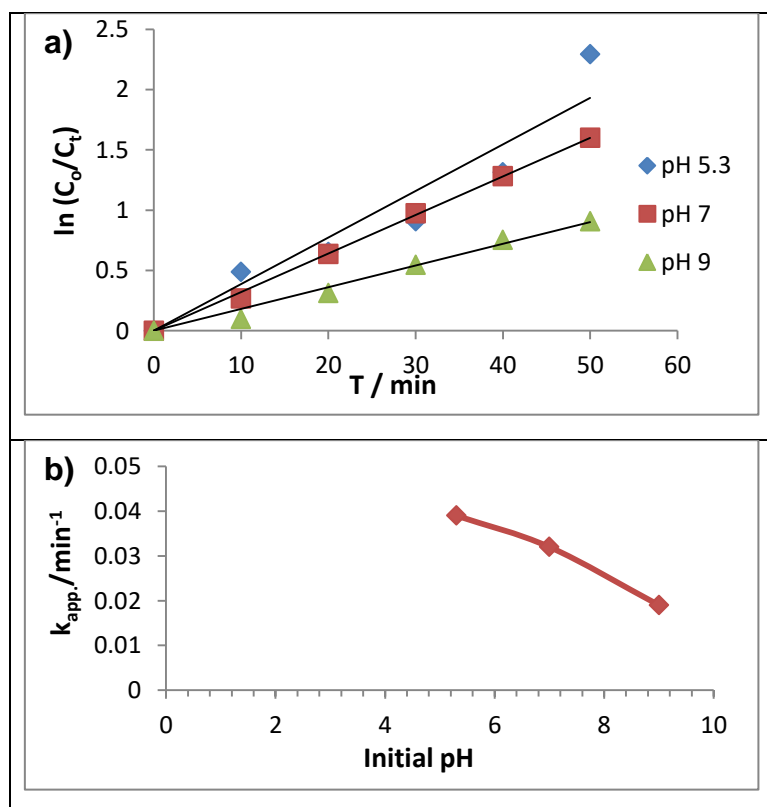
Figure (3-19). (a) The change of the $\ln(C_0/C_t)$ with irradiation time at pH solutions of Synthesis Al_2O_3 , (b). Relationship between the (k_{app}) and the different pH solution of Synthesis Al_2O_3 , (c) Effect the different pH solution of spinal MoFe_2O_4 on (PDE%).

Table (3-7). The change of the $\ln(C_0/C_t)$ with irradiation time at pH of IC dye by Nanocomposites with the presence of the CT-surfactant

Time (minutes)	pH	$\ln(C_0/C_t)$ Nanocomposites		
		5.3	7	9
0		0	0	0
10		0.4886	0.2682	0.0969
20		0.6519	0.6359	0.3132
30		0.9079	0.9724	0.5450
40		1.3133	1.2826	0.7537
50		2.2942	1.6010	0.9079
	$k_{app} \text{ min}^{-1}$	0.039	0.032	0.019

Table (3-8). The variation of (PDE%) with times Irradiation at different initial pH of IC dye by Nanocomposites with the presence of the CT-surfactant.

Time (minutes)	pH	PDE% Nanocomposites		
		5.3	7	9
0		0	0	0
10		38.6554	23.5294	9.2436
20		47.8991	47.0588	26.890
30		59.6638	62.1848	42.016
40		73.1092	72.2689	52.941
50		89.9159	79.8319	59.663



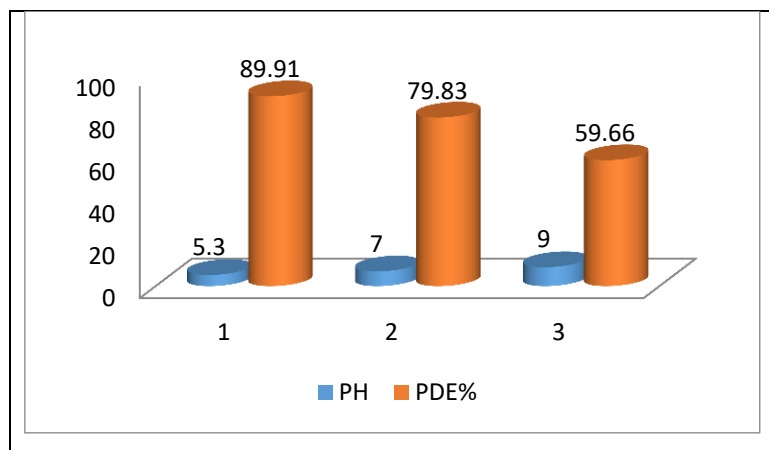


Figure (3-20). (a) The change of the $\ln(C_0/C_t)$ with irradiation time at pH solution of Nanocomposites ,(b) Relationship between the (k_{app}) and the different pH solution of Nanocomposites , (c) Effect the different pH solution of Nanocomposites on (PDE%) with the presence of CT-surfactant.

2. The effect of initial pH of IC dye solution Nanophotocatalyst Studies with the presence of the SDS-surfactant

Exhibit the findings demonstrate in tables (3-9) to (3-12) and figures (3-21) to (3-22). It was shown that the level reduction of indigo carmine IC dye was influenced by the pH of the solution. At a lower initial pH of the dye solution (pH = 5.3), the decolorization of IC takes place most thoroughly. because of the dye's naturally acidic makeup. At a pH of solution = pH_{pzc} , the Nanocomposites Synthesized Nanophotocatalyst contains SDS-surfactant and is cationicly charged [140]. Additionally, cationic and anionic ions are drawn to one another since IC is an ionic dye that becomes anionicly charged when dissolved in water. When the pH ranges of the IC solution declined, the decolorization intensified at pH 5.3 and achieved a considerable decolorized state. Under neutral and acidic conditions, the catalyst surface and the IC are both cationicly and anionicly charged, creating an attractive force that increases the decolorization of the IC dye because they can supply the hydroxyl groups needed to produce hydroxyl radicals. However, in an alkaline environment, the anionicly charged surfaces of the catalyst and IC reject one another, which

reduces photocatalytic activity because they are unable to create hydroxyl groups and IC dye decolorization.

Table (3-9). (a) $\ln(C_0/C_t)$ varying with times irradiation at various initial pH of IC dye by MoFe_2O_4 with the presence of the SDS-surfactant

Time (minutes)	pH	$\ln(C_0/C_t) \text{ MoFe}_2\text{O}_4$		
		5.3	7	9
0		0	0	0
10		0.1156	0.2682	0.0517
20		0.3017	0.3602	0.3602
30		0.5596	0.5024	0.3724
40		1.0655	0.6359	0.4886
50		1.4832	1.0179	0.6682
$K_{app} \text{ min}^{-1}$		0.0263	0.0168	0.0148

Table (3-10). The variation of (PDE%) with times Irradiation at different initial pH of IC dye by MoFe_2O_4 with the presence of the SDS-surfactant.

Time (minutes)	pH	PDE% MoF_2O_4		
		5.3	7	9
0		0	0	0
10		10.9243	23.5294	5.0420
20		26.0504	30.2520	30.2520
30		42.8571	39.4957	31.0924
40		65.5462	47.0588	38.6554
50		77.3109	63.8655	48.7394

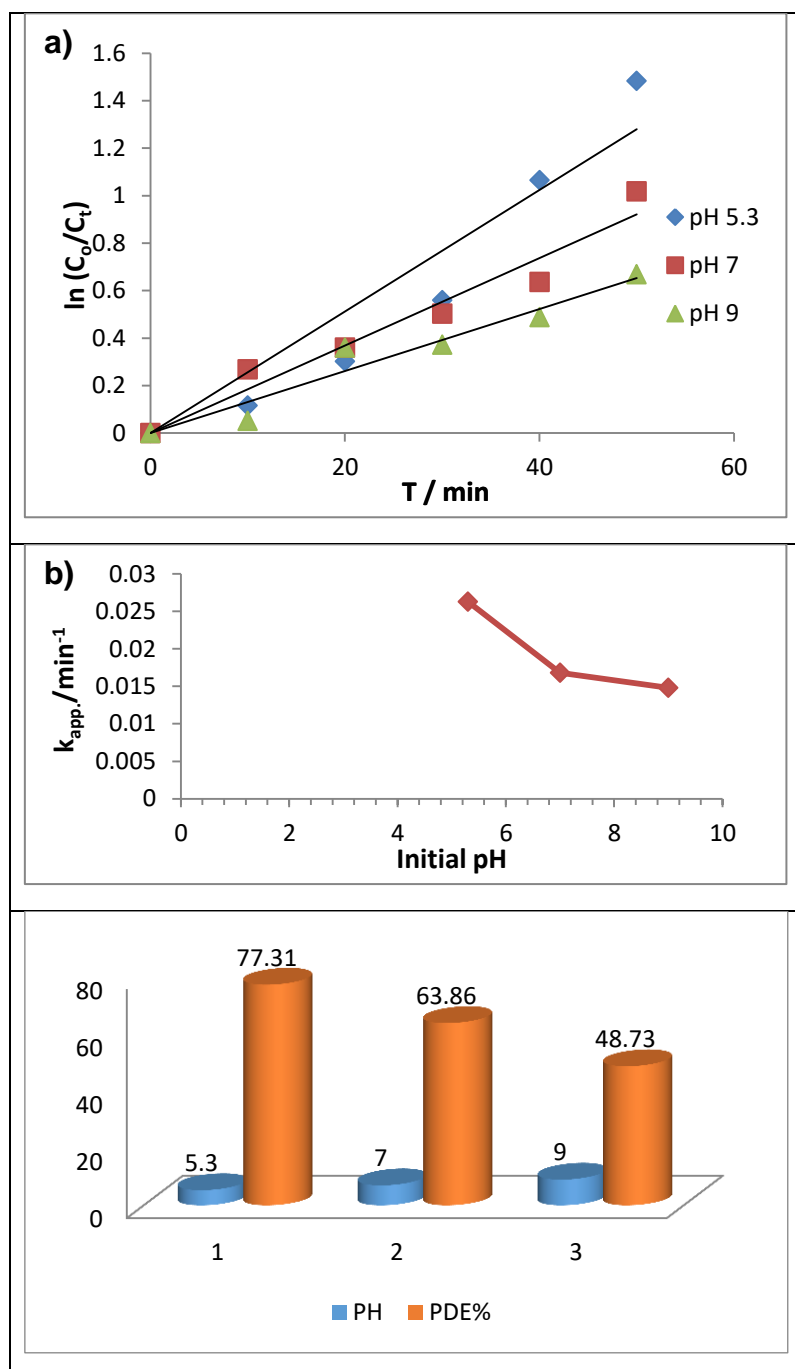


Figure (3-21). (a) The $\ln(C_0/C_t)$ variation with Irradiation time at various pH solutions of spinal MoFe_2O_4 , (b) Relationship between the (k_{app}) and the different pH solution of spinal MoFe_2O_4 , (c) Effect the different pH solution of spinal MoFe_2O_4 on (PDE%) with the presence of SDS-surfactant.

Table (3-11). The change of the $\ln(C_0/C_t)$ with irradiation time at pH of IC dye by Nanocomposites with the presence of the SDS-surfactant

<i>Time</i> (minutes)	<i>pH</i>	<i>ln(C₀/C_t) Nanocomposites</i>		
		5.3	7	9
0		0	0	0
10		0.3017	0.1541	0.0969
20		0.4886	0.2793	0.2358
30		0.8278	0.4483	0.2358
40		1.3451	0.5744	0.4096
50		1.8346	1.1415	0.5744
k_{app} min⁻¹		0.0347	0.0175	0.0128

Table (3-12). The variation of (PDE%) with times Irradiation at different initial pH of IC dye by Nanocomposites with the presence of the SDS-surfactant.

<i>Time</i> (minutes)	<i>pH</i>	<i>PDE% Nanocomposites -SDS</i>		
		5.3	7	9
0		0	0	0
10		26.0504	14.2857	9.2436
20		38.6554	24.3697	21.008
30		56.3025	36.1344	21.008
40		73.9495	43.6974	33.613
50		84.0336	68.0672	43.697

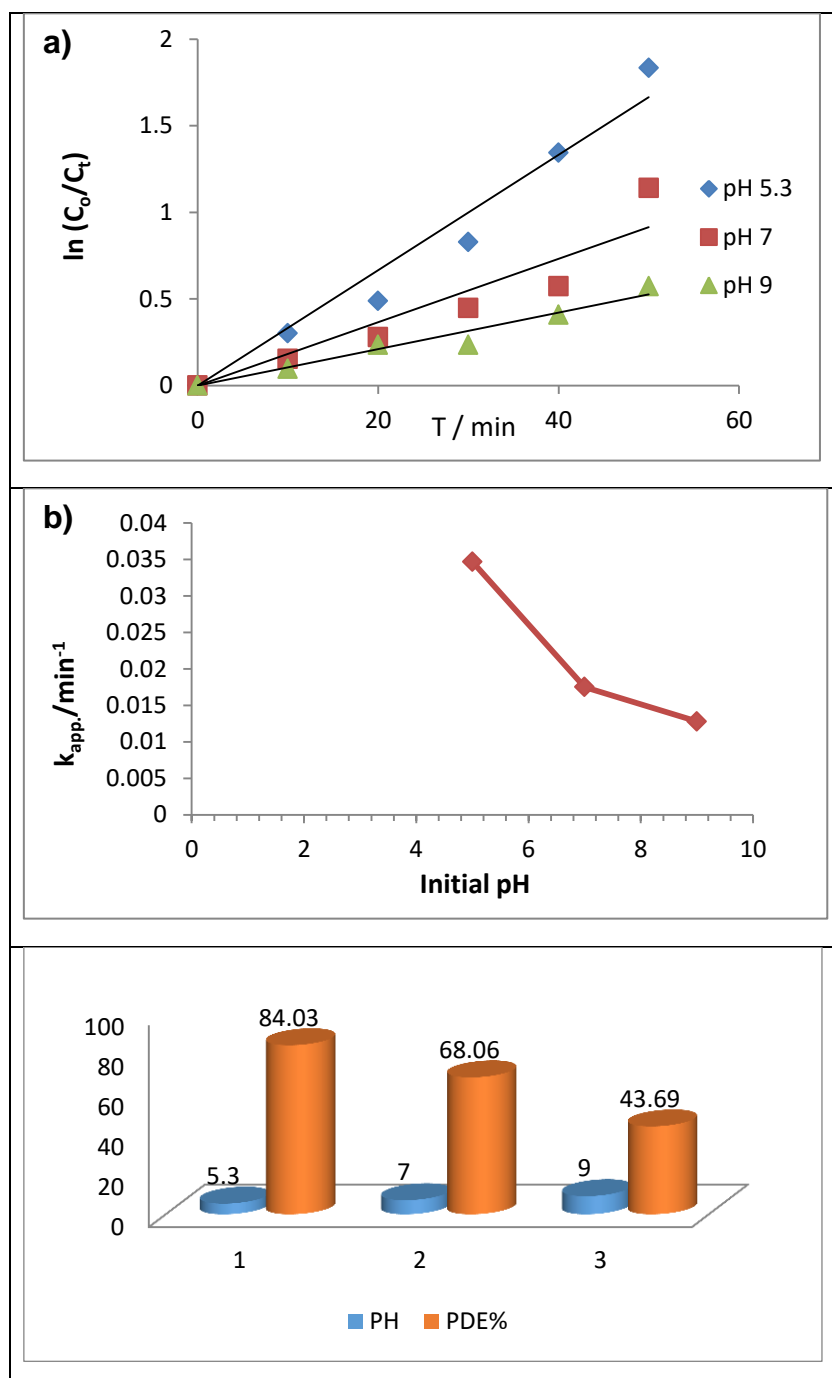


Figure (3-22). (a) The $\ln(C_0/C_t)$ variation with Irradiation time at various pH solution of Nanocomposites ,(b) Relationship between the (k_{app}) and the different pH solution of Nanocomposites , (c) Effect the different pH solution of Nanocomposites on (PDE%) with the presence of SDS-surfactant.

3.3.1.2. The effect of temperature

Temperature's effect on photocatalytic dye decolorization has been studied at various temperatures (from 283.15 to 298.15 K). Using an ice-filled water bath, temperatures were kept within the prescribed range.

1- Effect of temperature using MoFe₂O₄, Al₂O₃ and Nanocomposites with the presence of the CT-surfactant

Tables (3-13) to (3-19) and figures (3-23), were observed that the photo decolorization values decrease with increasing the temperature from 283.15 K to 25 °C, In the period from 10 to 50 minutes, due the photoreaction is exothermic and this is agreement with results that reported in literature [149]. By this behavior, oxygen molecules (O₂) will chemisorb on the surface of MoFe₂O₄ and will capture free electrons from the MoFe₂O₄ conduction band to ionize into oxygen ions such as O²⁻, O²⁻, and O⁻ depending on the temperature. In contrast to Al₂O₃, the decrease in electron concentration on the surface of MoFe₂O₄ results in the formation of an electron depletion layer on the surface [150].

Table (3-13) Activation energies and thermodynamic functions for decoloration IC dye Calculated the spinal MoFe₂O₄ in the presence of CT-surfactant, Al₂O₃ synthesis, and Nanocomposites.

<i>Parameters</i>	<i>E_a[*]</i> <i>(kJ.mol⁻¹)</i>	<i>ΔH[*]</i> <i>(kJ.mol⁻¹)</i>	<i>ΔS[*]</i> <i>(Jk⁻¹.mol⁻¹)</i>	<i>ΔG[*]</i> <i>(kJ.mol⁻¹)</i>
MoFe ₂ O ₄ -CT	-38.96772	-41.383	-6.0309	-39.628
Al ₂ O ₃	-11.3395	-13.755	-4.5935	-12
Nanocomposites	-26.3928	-26.125	-5.3931	-24.37

According to the activation energy values, Al_2O_3 has a high activation energy because of its large bandgap (the activation energy exceeds the energy required to move an electron from the valance band to the conductive band). Spinel MoFe_2O_4 is mixed with it. While the decrease in activation energy is noticeable [151]. The spinel MoFe_2O_4 surface activation energies before and after incorporation of Al_2O_3 were found to be anionic values. It might mean that the photoreaction will take place in several steps, One of which may be exothermic and then convert at extremely low cationic activation energy through a number of chain reactions [152]. As a result, a quick binding step may occur on the Fe^{3+} location in the crystal lattice, whereas a slower step (having an extremely low activation energy value) may occur on the Mo^{6+} a position. The spinel structure is studied in this behavior, which involves Fe^{3+} in tetrahedral hybridization and Mo^{6+} in octahedral hybridization. This condition results in anionic enthalpy values when spinel and related compounds are used [153].

According to the anionic value of entropy, the transition state produced by the breakdown of this dye has less structural freedom than the reactant (dye molecule). According to discovered thermodynamic theories, photoreaction is exothermic and spontaneous. The entropy (ΔS^*) is also anionic due to depressing in randomness at the solid-solution interface *via* the (IC) decolorization, and indicates that some structural exchange occurs among the active sites of the dye and ions [154].

Table (3-14). The change of the $\ln(C_0/C_t)$ with irradiation time at temperatures of spinal MoFe_2O_4 with the presence of the CT-surfactant *via* Synthesized Nanophotocatalyst de-colorization of IC dye.

Time (minutes)	T/k	$\ln(C_0/C_t) \text{ MoFe}_2\text{O}_4$			
		283.15	288.15	293.15	298.15
0		0	0	0	0
10		0.5760	0.3209	0.3119	0.1835
20		0.9699	0.5195	0.5531	0.3718
30		1.5040	0.7129	0.8257	0.5705
40		1.9859	0.9529	1.0986	0.7246
50		2.3913	1.2237	1.2017	0.9705
$k_{app} \text{ min}^{-1}$		0.049	0.0245	0.0262	0.0189

Table (3-15). The variation of (PDE%) with times Irradiation at different temperatures of spinal MoFe_2O_4 with the presence of the CT-surfactant *via* Synthesized Nanophotocatalyst de-colorization of IC dye.

Time (minutes)	T /k	PDE% MoF_2O_4			
		283.15	288.15	293.15	298.15
0		0	0	0	0
10		43.7908	27.4509	26.7973	16.7701
20		62.0915	40.5228	42.4836	31.0559
30		77.7777	50.9803	56.2091	43.4782
40		86.2745	61.4379	66.6666	51.5527
50		90.1960	70.5882	69.9346	62.1118

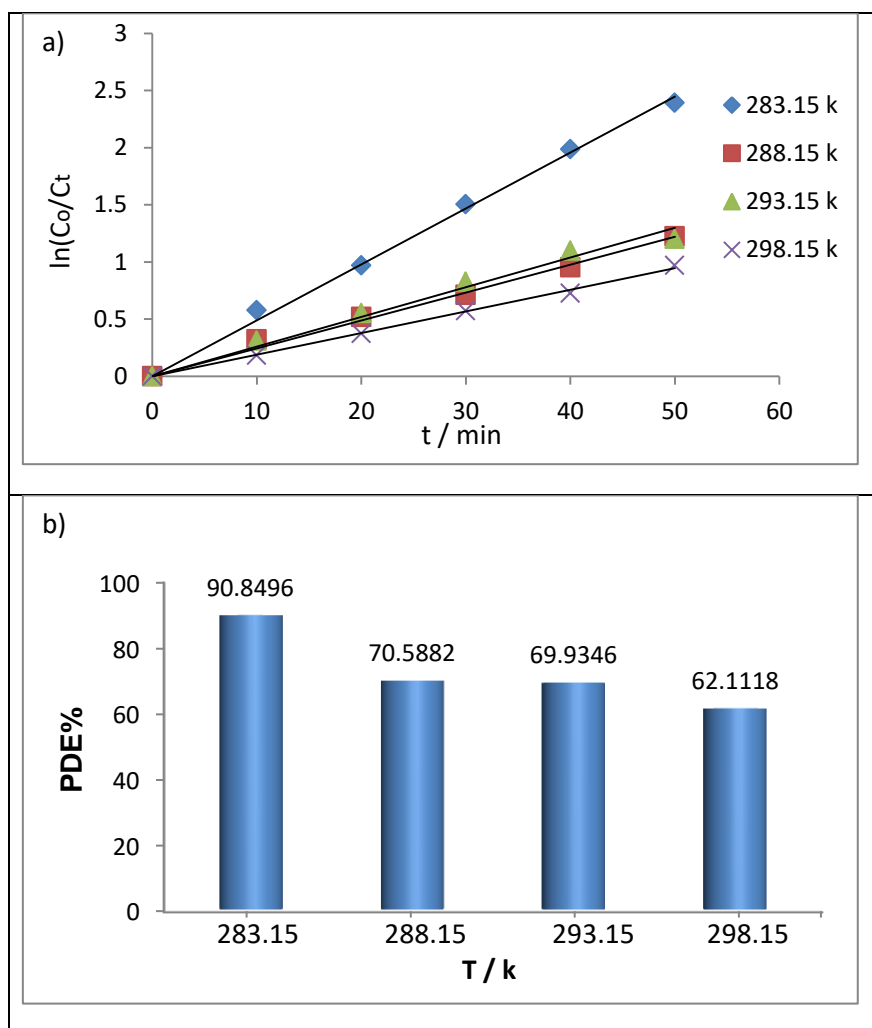


Figure (3-23). (a) The $\ln(C_0/C_t)$ variation with Irradiation time at various temperatures of spinal MoFe_2O_4 (b) Effect of the different temperature of spinal MoFe_2O_4 on (PDE%) with the presence of CT-surfactant.

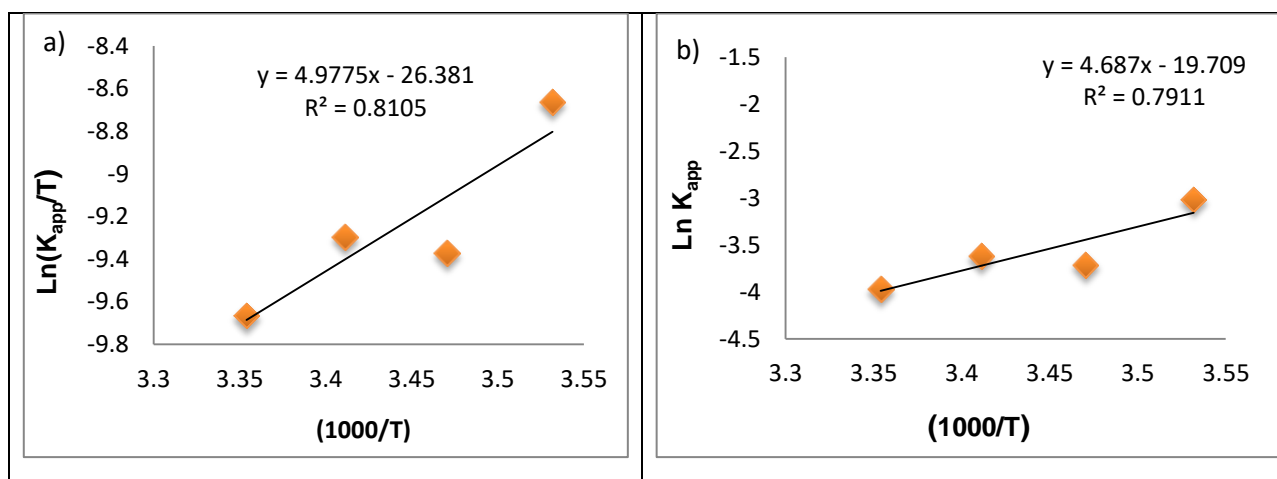


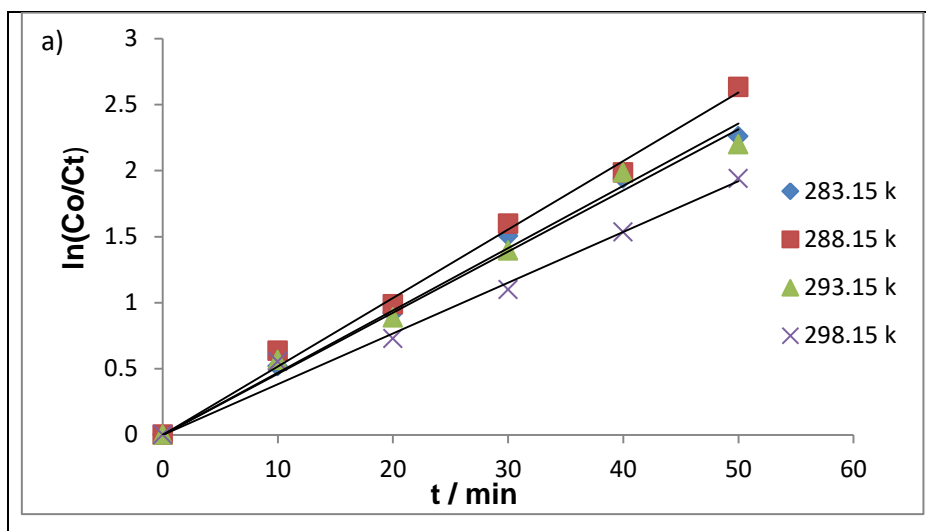
Figure (3-24). (a) Eyring–Polanyi plot $\ln(k_{app}/T)$ VS. $1000/T$ (b) Arrhenius plot by spinal MoFe_2O_4 via Synthesized Nanophotocatalyst de-colorization of IC dye.

Table (3-16). The $\ln(C_0/C_t)$ variation with times Irradiation at various temperatures of Synthesis Al_2O_3 via Synthesized Nanophotocatalyst de-colorization of IC dye.

<i>t / k</i> <i>Time</i> <i>(minutes)</i>	<i>ln(C₀/C_t) Al₂O₃</i>			
	283.15	288.15	293.15	298.15
0	0	0	0	0
10	0.5195	0.6359	0.5645	0.5531
20	0.9195	0.9873	0.8873	0.7263
30	1.5040	1.5964	1.3928	1.0986
40	1.9393	1.9859	1.9859	1.5339
50	2.2578	2.6325	2.1972	1.9393
<i>k_{app}</i> min⁻¹	0.0471	0.0518	0.0463	0.039

Table (3-17). The variation of (PDE%) with times Irradiation at different temperatures of Synthesis Al_2O_3 via Synthesized Nanophotocatalyst decolorization of IC dye.

Time (minutes)	T /k	PDE% Al_2O_3			
		283.15	288.15	293.15	298.15
0		0	0	0	0
10		40.5228	47.0588	43.1372	42.4836
20		60.1307	62.7450	58.8235	51.6339
30		79.7385	79.7385	75.1633	66.6666
40		85.6209	86.2745	86.2745	78.4313
50		89.5424	92.8104	88.8888	85.6209



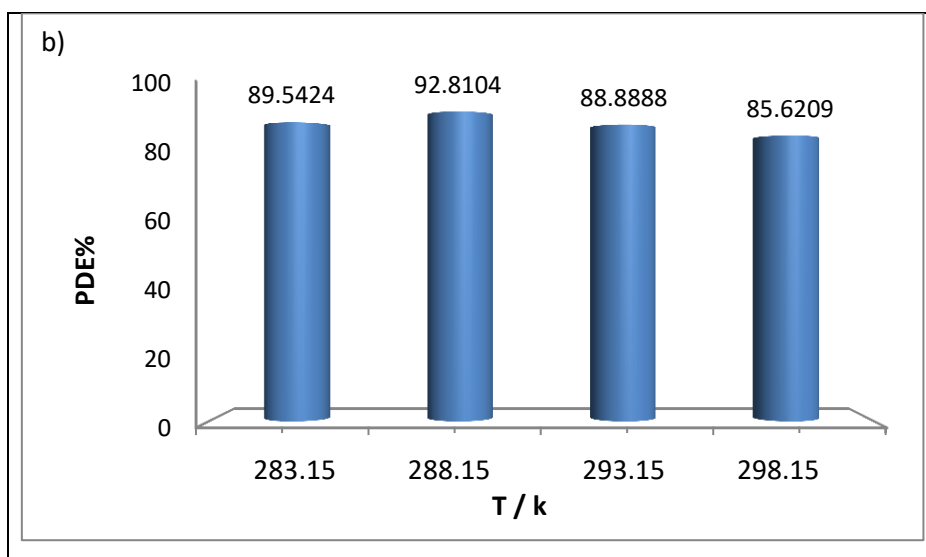


Figure (3-25). (a) The $\ln(C_0/C_t)$ variation with Irradiation time at various temperatures of Synthesis Al_2O_3 (b) Effect of the different temperature of Synthesis Al_2O_3 on (PDE%).

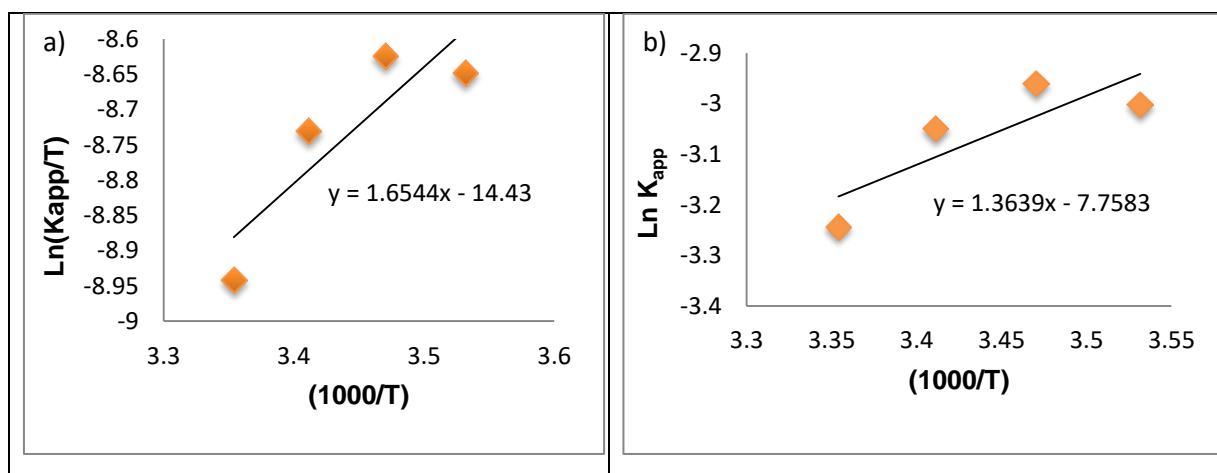


Figure (3-26). (a) Eyring–Polanyi plot $\ln(k_{app}/T)$ VS. $1000/T$ (b) Arrhenius plot by Synthesis Al_2O_3 via Synthesized Nanophotocatalyst de-colorization of IC dye.

Table (3-18). The change of the $\ln(C_0/C_t)$ with irradiation time at temperatures of Nanocomposites with the presence of CT-surfactant *via* Synthesized Nanophotocatalyst de-colorization of IC dye.

<i>Time</i> (minutes)	<i>T/k</i>	<i>ln(C₀/C_t) Nanocomposites</i>			
		283.15	288.15	293.15	298.15
0		0	0	0	0
10		0.6115	0.2768	0.8109	0.2660
20		1.0231	0.5418	1.0050	0.3661
30		1.5040	0.8407	1.1592	0.5255
40		1.9393	1.0986	1.2237	0.7303
50		2.4654	1.3928	1.3168	1.0487
k_{app} min⁻¹		0.0496	0.0265	0.0299	0.02

Table (3-19). The variation of (PDE%) with times Irradiation at different temperatures of Nanocomposites with the presence of the CT-surfactant *via* Synthesized Nanophotocatalyst de-colorization of IC dye.

<i>Time</i> (minutes)	<i>T /k</i>	<i>PDE% Nanocomposites</i>			
		283.15	288.15	293.15	298.15
0		0	0	0	0
10		45.7516	24.1830	55.5555	23.3576
20		64.0522	41.8300	63.3986	30.6569
30		78.4313	56.8627	68.6274	40.8759
40		85.6209	66.6666	70.5882	51.8248
50		91.5032	75.1633	73.2026	64.9635

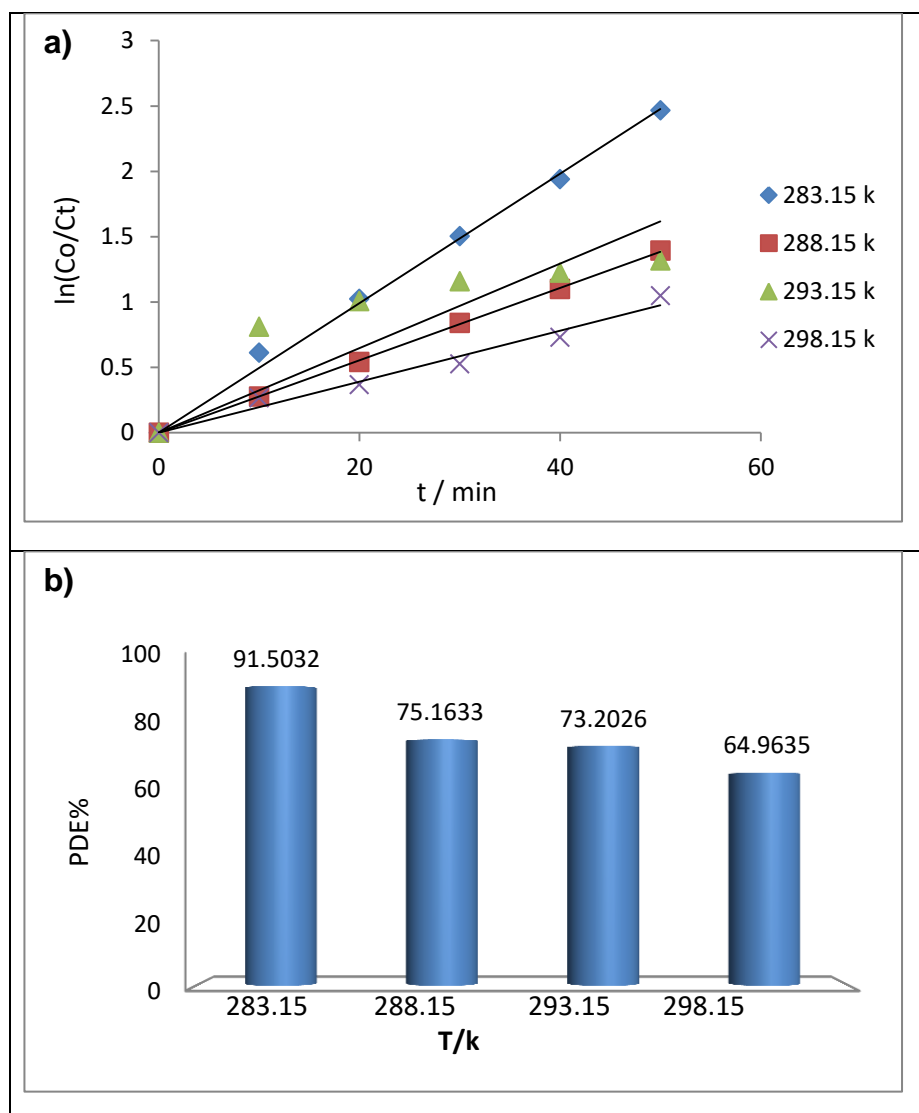


Figure (3-27). (a) The $\ln(C_0/C_t)$ variation with Irradiation time at various temperatures of Nanocomposites (b) Effect of the different temperature of Nanocomposites on (PDE%) with the presence of CT-surfactant.

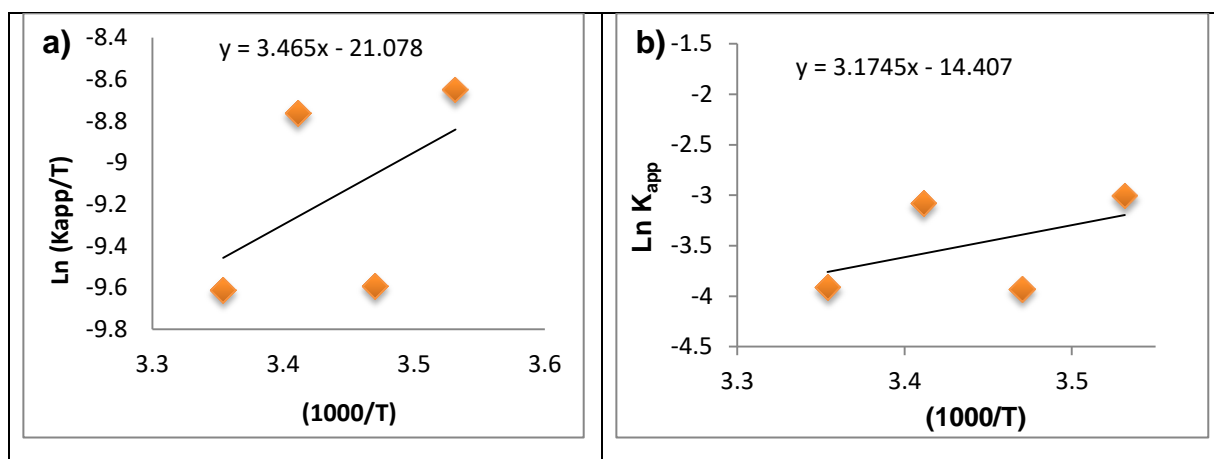


Figure (3-28). (a) Eyring–Polanyi plot $\ln (k_{app}/T)$ VS. $1000/T$ (b) Arrhenius plot by Nanocomposites with the presence of SDS-surfactant *via* Synthesized Nanophotocatalyst de-colorization of IC dye.

2- Effect of temperature using MoFe_2O_4 , Al_2O_3 and Nanocomposites with the presence of the SDS-surfactant

Table (3-20) Calculated the spinal MoFe_2O_4 in the presence of SDS-surfactant, Al_2O_3 synthesis, and Nanocomposites, activation energies and thermodynamic functions for decolorizing IC dye.

<i>Parameters</i>	Ea^* (kJ.mol^{-1})	ΔH^* (kJ.mol^{-1})	ΔS^* ($\text{Jk}^{-1}.\text{mol}^{-1}$)	ΔG^* (kJ.mol^{-1})
MoFe_2O_4 -SDS	174.460	172.049	4.714	173.847
Al_2O_3	-11.339	-13.755	-4.593	-12
Nanocomposites	-36.520	-60.199	-6.972	-58.455

Based on the results reported in Tables (3-20) to (3-24) and figures (3-29) to (3-32), by using MoFe_2O_4 Nanoparticles and their nanocomposites with the presence of the SDS-surfactant, found that the decrease in the temperature reduced the photocatalytic decolorization of Indigo Carmine IC dye. The

removal rate increased as the temperature climbed to 298.15 K because the reaction is endothermic, indicating a positive value of (ΔH^*). Furthermore, the change in enthalpies (ΔH^*) and Gibbs free energy (ΔG^*) are both positive, indicating that the reaction happens nonspontaneously when the solvated intermediate between dye and hydroxide radical $\cdot\text{OH}$ exists [155]. However, after mixing with alumina, the activation energies of molybdenum ferrite in the presence of the SDS-surfactant altered to become ($-36.520 \text{ kJ mol}^{-1}$) for composite, where the reaction was spontaneous after incorporation of Al_2O_3 with MoFe_2O_4 . These results are consistent with those published in references. [156], [157]. Furthermore, the low activation energy values ensure that this photoreaction is quick, and the photoreaction employing Nanocomposites is faster than the other prepared Synthesized Nanophotocatalyst with pseudo-first order kinetics.

Table (3-21). The change of the $\ln(C_0/C_t)$ with irradiation time at temperatures of spinal MoFe_2O_4 with the presence of the SDS-surfactant via Synthesized Nanophotocatalyst de-colorization of IC dye.

<i>Time</i> (minutes)	<i>T/k</i>	<i>ln(C₀/C_t) MoFe₂O₄</i>			
		283.15	288.15	293.15	298.15
0		0	0	0	0
10		0.51957	0.2855	0.5877	0.3101
20		0.79633	0.3957	0.6609	0.3610
30		0.91956	0.5996	0.8560	0.6751
40		1.06014	0.7399	1.1386	0.9470
50		1.26923	1.3168	1.3928	2.6210
$k_{app} \text{ min}^{-1}$		0.0281	0.0223	0.0285	1.7146

Table (3-22). The variation of (PDE%) with times Irradiation at different temperatures of spinal MoFe_2O_4 with the presence of the SDS-surfactant via photocatalytic de-colorization of IC dye.

Time (minutes)	T /k	PDE% MoF_2O_4			
		283.15	288.15	293.15	298.15
0		0	0	0	0
10		40.5228	24.8365	44.4444	26.6666
20		54.9019	32.6797	48.3660	30.3030
30		60.1307	45.0980	57.5163	49.0909
40		65.3594	52.2875	67.9738	61.2121
50		71.8954	73.2026	75.1633	92.7272

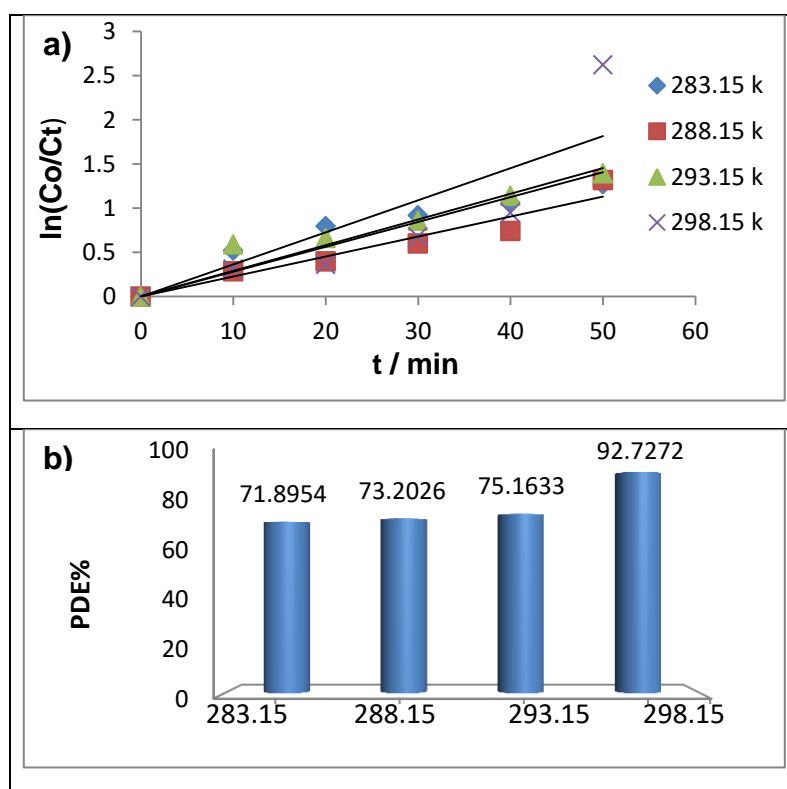


Figure (3-29). (a) The $\ln(C_0/C_t)$ variation with Irradiation time at various temperatures of spinal MoFe_2O_4 (b) Effect of the different temperature of spinal MoFe_2O_4 on (PDE%) with the presence of SDS-surfactant.

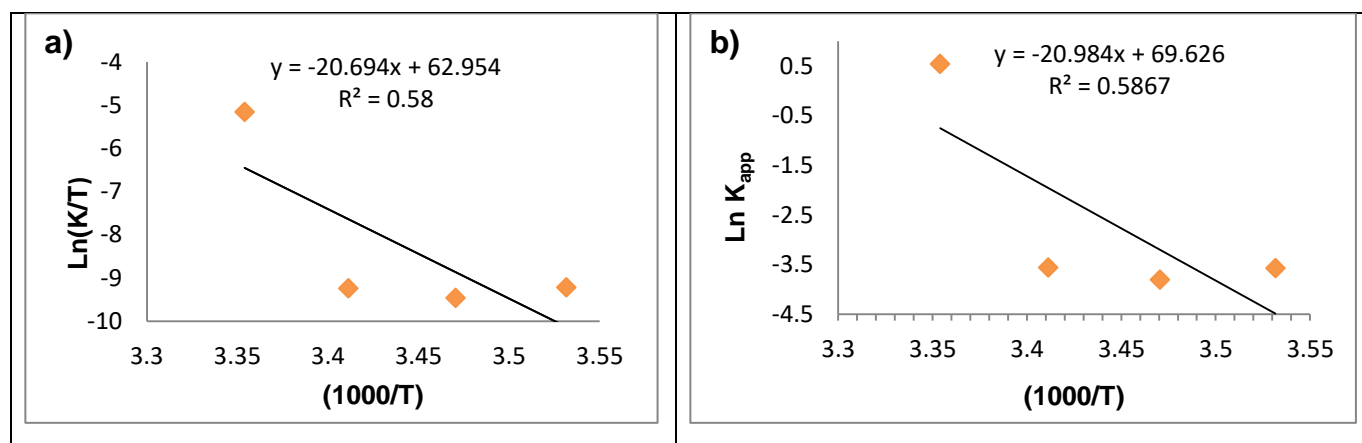


Figure (3-30). (a) Eyring–Polanyi plot $\ln(k_{app}/T)$ VS. $1000/T$ (b) Arrhenius plot by spinal MoFe_2O_4 via Synthesized Nanophotocatalyst de-colorization of IC dye.

Table (3-23). The change of the $\ln(C_0/C_t)$ with irradiation time at temperatures Nanocomposites with the presence of the SDS-surfactant via photocatalytic de-colorization of IC dye.

Time (minutes)	T /k	$\ln(C_0/C_t)$ Nanocomposites			
		283.15	288.15	293.15	298.15
0		0	0	0	0
10		0.6115	0.2346	0.4454	0.1476
20		1.2017	0.3483	0.7263	0.2346
30		1.6982	0.5195	0.9529	0.3764
40		2.2578	0.8407	1.2462	0.7263
50		2.7278	1.2692	1.5964	1.0791
$k_{app} \text{ min}^{-1}$		0.056	0.0226	0.0323	0.0212

Table (3-24). The variation of (PDE%) with times Irradiation at different temperatures of Nanocomposites in the presence of SDS-surfactant by photocatalytic de-colorization of IC dye.

<i>Time</i> (minutes)	<i>T /k</i>	<i>PDE% Nanocomposites</i>			
		283.15	288.15	293.15	298.15
0		0	0	0	0
10		45.7516	20.9150	35.9477	13.7254
20		69.9346	29.4117	51.6339	20.9150
30		81.6993	40.5228	61.4379	31.3725
40		89.5424	56.8627	71.2418	51.6339
50		93.4640	71.8954	79.7385	66.0130

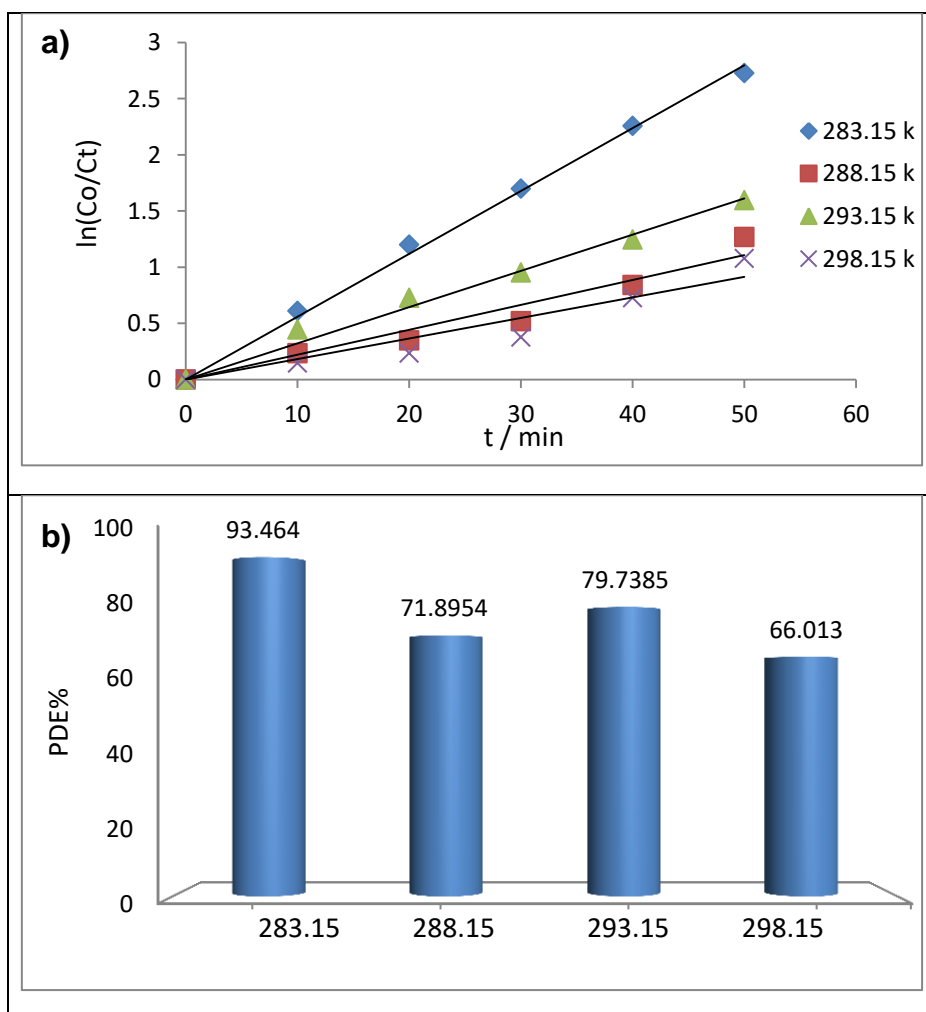


Figure (3-31). (a) The $\ln(C_0/C_t)$ variation with Irradiation time at various temperatures of Nanocomposites (b) Effect of the different temperature of Nanocomposites on (PDE%) with the presence of SDS-surfactant.

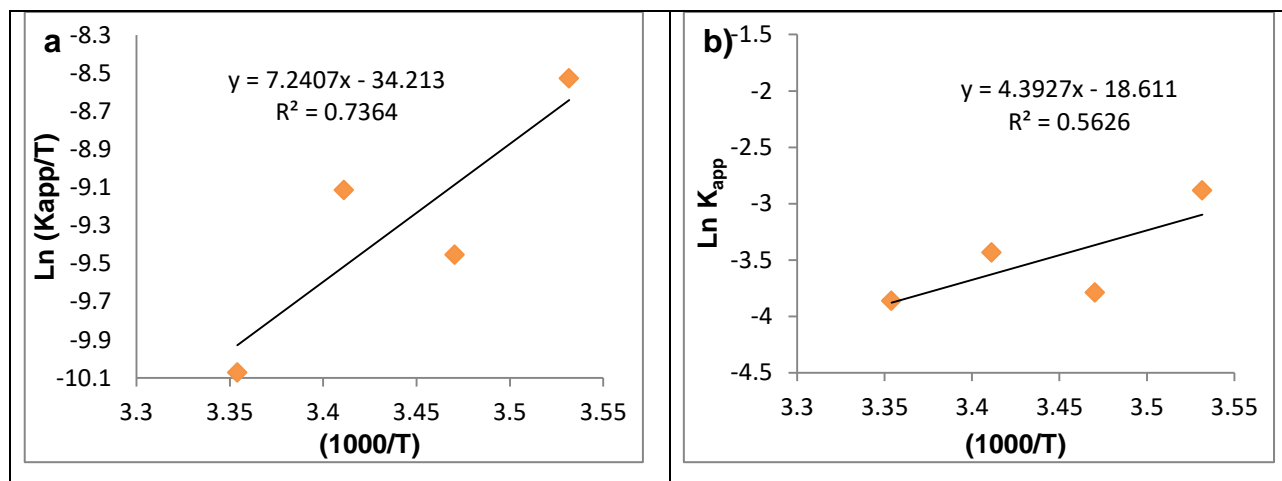


Figure (3-32). (a) Eyring–Polanyi Equation plot $\ln(k_{app}/T)$ VS. $1000/T$ (b) Arrhenius Equation plot by Nanocomposites with the presence of SDS-surfactant *via* Synthesized Nanophotocatalyst de-colorization of IC dye.

3.4. Quantum yield of Photo-decolorization of IC Dye

Table (3-24) and figures (3-33) to (3-34), summarize the quantum yields of all Synthesized Nanophotocatalysts for decolorization of Indigo Carmine IC dye and by using equation (2-18) to calculate Φ . Where the Quantum yield of IC dye de-colorization is increased as the following:

Φ using synthesis $Al_2O_3 > \Phi$ Nanocomposites $> \Phi$ $MoFe_2O_4$ Nanoparticles with the presence of the SDS-surfactant, showed quantum yield of 1.35, 0.669 and 0.644 respectively. While the presence of the CT-surfactant was Nanocomposites ($\Phi = 0.943$) was seen to have the highest than $MoFe_2O_4$ Nanoparticles ($\Phi = 0.527$). These low values of quantum yields value (less than 1) that may be attitudes to photophysical deactivation processes (ISC and IC process), quenching materials, and dye molecule dimerization as a result of

recombination processes that trigger reversible reactions [158], [159]. Where, the quantum yield of MoFe_2O_4 Nanoparticles is low compared to its combination with Al_2O_3 , as the efficiency ratio of the nanocomposites improved, due to the separation of charges and the increase in surface acidity, which leads to the formation of $\cdot\text{OH}$ for $\cdot\text{OH}$ adsorption.

Table (3-25). Values quantum yields of all Synthesized Nanophotocatalysts for decolorization IC dye.

Samples Synthesized Nanophotocatalysts	Type surfactant	Quantum yield Φ
MoFe_2O_4	SDS	0.644
Al_2O_3	Non.surf..	1.35
Nanocomposites	SDS	0.669
MoFe_2O_4	CT	0.527
Nanocomposites	CT	0.943

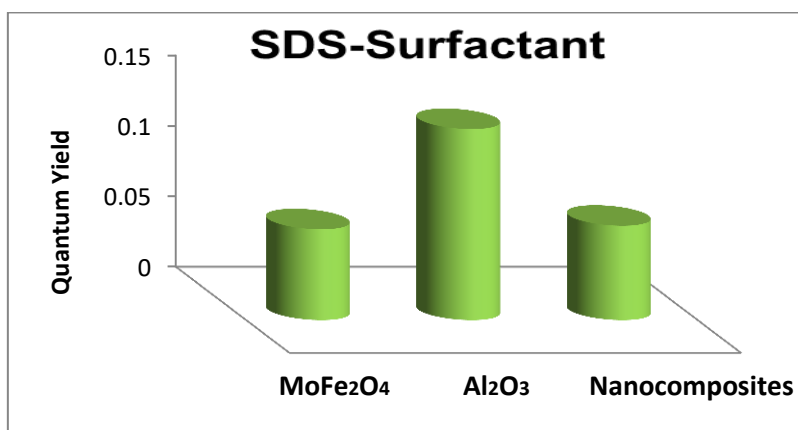


Figure (3-33). The relation of the quantum yield of IC dye photo-decolorization with samples studied in the presence of SDS-surfactant at pH 5.3, temperature 293.15 K.

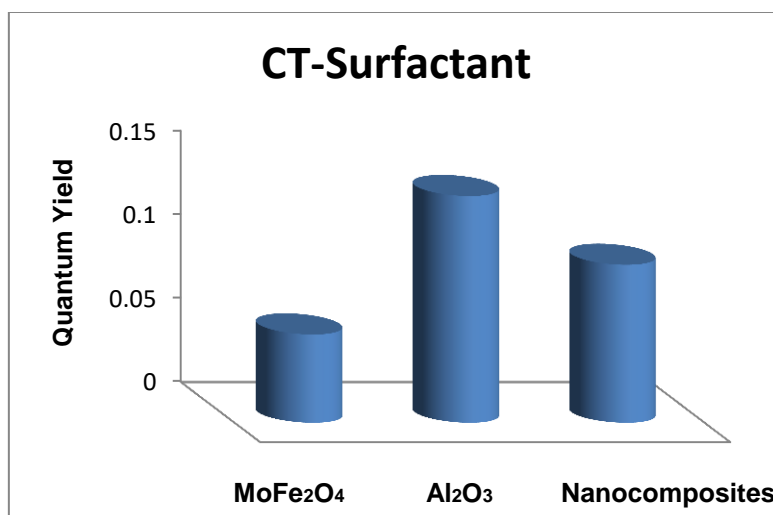


Figure (3-34). The relation of the quantum yield of IC dye photo-decolorization with samples studied in the presence of CT-surfactant at pH 5.3, temperature 293.15 K.

3.5. Suggested Decolorization Mechanism of IC Dye

The products of the active species, such as superoxide anion, peroxide radical, and hydroxyl radical, in solution or on the surface of the Synthesized Nanophotocatalyst, are essentially what determines any postulated mechanism for a photocatalytic process [115], [160]. The ability of these species to dissolve and decolorize any organically colored materials has been changed. The hydroxyl radical works as a potent oxidant to damage the dye molecules because it is a more active species in an aqueous solution with 2.8 V [135], [161], [162]. Similar studies on the decolorization of indigo carmine propose that the isatin 5-sulfonic acid, the main aromatic component, was produced as a result of the C=C bond being broken by hydroxyl radicals attacking the compound's C(1) and C(10) positions. Oxidation of the two sulfonic groups in the starting molecule results in indigo, which then undergoes the loss of two sulfonic groups to become isatin. Further decolorization of isatin 5 sulfonic acid, which also releases the sulfonic group and isatin, results in the production of oxalic and oxamic acid. An almost complete mineralization is brought on by

these carboxylic acids. Based on these observations, they applied the same degrading procedure as in (Figure (3-35) [163]–[165]).

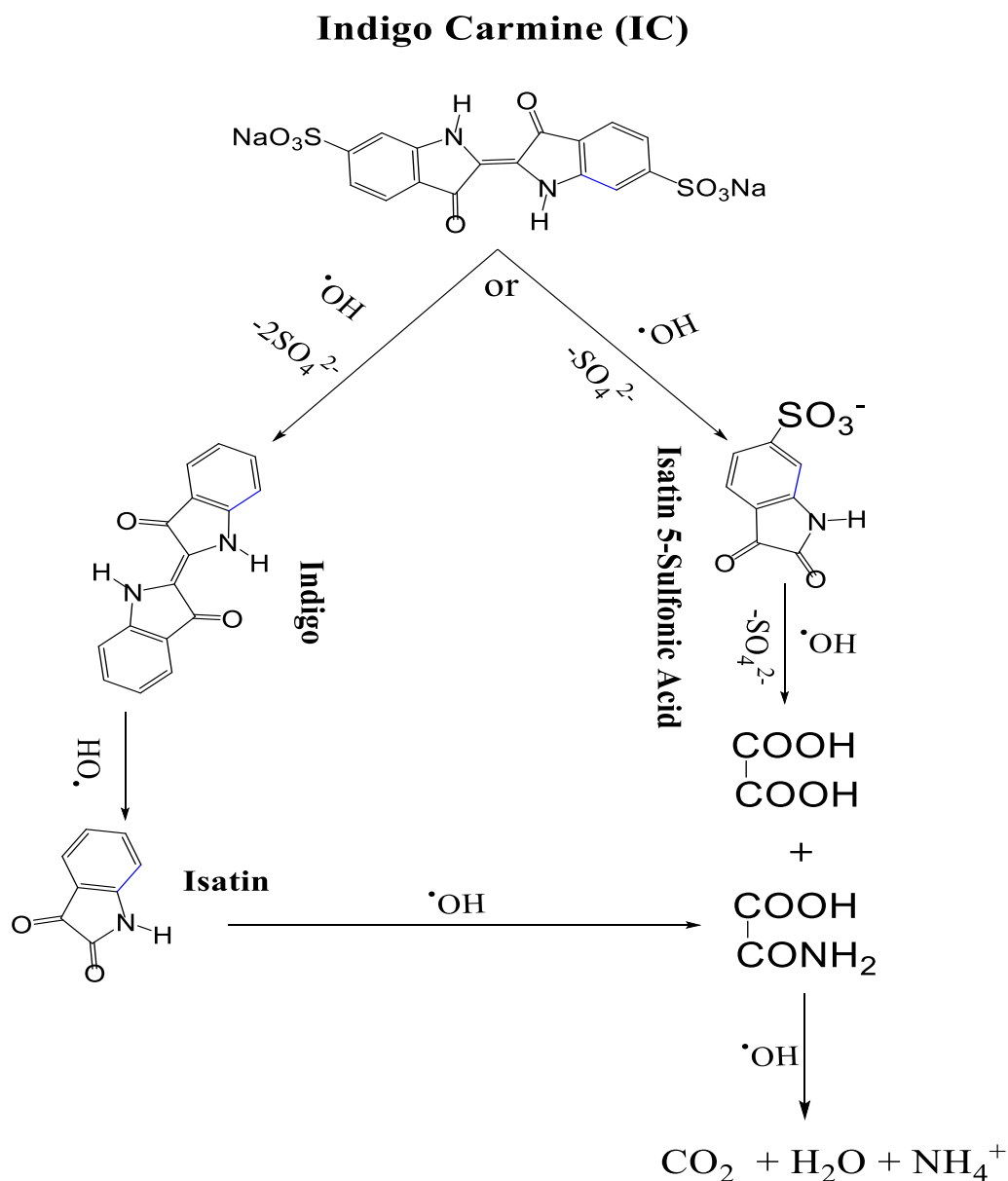


Figure (3-35). Schematic diagram of the photocatalytic system, hydroxyl radical-mediated to decolorization and degradation of IC dye.

3.6. Conclusion

This study focused on nanoparticle catalysts that were prepared with Hydrothermal technology, the nanocomposites were produced from using 1:2 w/w ratio from MoFe_2O_4 to Alumina using the Ultrasonic method. They were then tested for dye decolorization effectiveness as a Synthesized Nanophotocatalyst using Indigo Carmine IC dye solution. Based on this research, the following results were obtained:

1. The spinel MoFe_2O_4 in the presence of the SDS-surfactant and normal spinel MoFe_2O_4 in the presence of the CT-surfactant as nanoparticle different shapes and sizes by hydrothermal method were successfully Prepared.
2. Using surfactants (SDS and CT) as a template in hydrothermal technique, and a stabilizer agent at the same time.
3. The synthesis of Nanocomposites was successfully produced from incorporated of MoFe_2O_4 with Al_2O_3 , in aqueous solutions, an ultrasonic technique is used.
4. The FT-IR spectra occurred, the tetrahedral site position (lowest frequency band ν_2), and octahedral site position (highest frequency band ν_1) were found for prepared spinel and their composites. The spinel MoFe_2O_4 with SDS-surfactant, is found to be normal, while, the spinel MoFe_2O_4 with CT-surfactant, is found to be inverse.
5. The mean crystallite sizes of MoFe_2O_4 with SDS and CT-surfactant, were calculated depending on the XRD data. The mean crystallite sizes and crystallite sizes of both MoFe_2O_4 with SDS and CT-surfactant increased after being incorporated with Al_2O_3 , due to high aggregation.
6. SEM images revealed that the morphologies of MoFe_2O_4 with SDS-surfactant as Nano-grain, while in the presence of CT-surfactant is have Nano-plates shape. Additionally, this suggests that the spherical forms of

Al_2O_3 and its nanocomposites . due to the large amount of Al_2O_3 binding and dispersive with MoFe_2O_4 .

7. The Tauc result showed that the band gap of MoFe_2O_4 Nanoparticles in the presence of SDS, and CT-surfactants is direct, while indirect after incorporation with synthesis Al_2O_3 as a nanocomposites and to be low band gaps.
8. Coupling of alumina with molybdenum ferrite the bandgap decrease and thus excited the electron–hole pair with visible light.
9. Pairing alumina with molybdenum ferrite decreased the recombination rate of the electron–hole pair thereby enhancing photocatalytic efficiency. Also, the optical properties of the catalyst were increased.
10. The photoactivity of MoFe_2O_4 with SDS, CT-surfactant, and their composites was done with 0.025 g in 100mL of Indigo Carmine IC Dye solution at 293.15 K at pH = 5.3. The photoreaction obeyed pseudo-first order exothermic reaction of kinetic with low activation energy of MoFe_2O_4 with CT-surfactant with all their composites, except for MoFe_2O_4 with SDS-surfactant is endothermic reaction.
11. The point of zero charge(pH_{pzc}) point produced the most activity was achieved. Where the activity of the catalyst changed when the pH changed.
12. The quantum yields are low values of IC dye decolorization in the following sequence: Φ synthesis Al_2O_3 > Φ Nanocomposites > Φ MoFe_2O_4 Nanoparticles in the presence of CT or SDS-surfactant.

3.6. Future Works

1. Synthesis of MoFe_2O_4 replacing D.W. solvent as the solvent for the precursor materials ($\text{Na}_2\text{MoO}_4 \cdot 2\text{H}_2\text{O}$) and ($\text{Fe}(\text{NO}_3)_3 \cdot 9\text{H}_2\text{O}$), in the autoclaving step, using a Hydrothermal method, to modify the obtained MoFe_2O_4 and Nanocomposites' shape and optical characteristics.
2. Calcination process for prepared MoFe_2O_4 Nanoparticles and Nanocomposites to obtain a new crystal size.
3. Altering the temperature, solvent, phase and pH to increase the quantum yield Φ .
4. Improved the properties of MoFe_2O_4 by loading different types of certain transition metals such as TiO_2 and SiO_2 on the surface of MoFe_2O_4 , then studied the nanoparticle's characterizations and compared the photo-decolorization efficiency.
5. Application of the different conditions such as varied catalyst dosages and the Fenton reaction, to determine the optimum conditions using the MoFe_2O_4 Nanoparticles.
6. The use of these catalysts as a gas sensor. These catalysts can be used as an anode in solar cells.

References

- [1] H. M. Mohammad, S. I. Saeed, and L. M. Ahmed, "Broccoli-like Iron Oxide Nanoparticles Synthesis in Presence of Surfactants and Using Them in the Removal of Water-Colored Contamination," *J. Nanostructures*, vol. 12, no. 4, pp. 1034–1048, 2022.
- [2] R. A. Alattar, H. M. Saleh, J. A. Al-Hilifi, and L. M. Ahmed, "Influence the addition of Fe^{2+} and H_2O_2 on removal and decolorization of textile dye (dispersive yellow 42 dye)," *Egypt. J. Chem.*, vol. 63, no. 9, pp. 3453–3463, 2020.
- [3] S. I. Saeed, B. H. Taresh, L. M. Ahmed, Z. F. Haboob, S. A. Hassan, and A. A. A. Jassim, "Insight into the Oxidant Agents Effect of Removal and Photo-decolorization of Vitamin B12 Solution in Drug Tablets using ZrO_2 ," *J. Chem. Heal. Risks*, vol. 11, no. 4, pp. 393–402, 2021.
- [4] A. A. Marhoon, S. I. Saeed, and L. M. Ahmed, "Application of some effects on the Degradation of the aqueous solution of Fuchsine dye by photolysis," *J. Glob. Pharma Technol.*, vol. 11, no. 9, pp. 76–81, 2019.
- [5] H. Kadhim, L. Ahmed, and M. AL-Hachamii, "Facile Synthesis of Spinel CoCr_2O_4 and Its Nanocomposite with ZrO_2 : Employing in Photo-catalytic Decolorization of Fe (II)-(luminol-Tyrosine) Complex.," *Egypt. J. Chem.*, vol. 65, no. 1, pp. 481–488, 2022.
- [6] R. A. Alattar, Z. M. Hassan, S. K. Abass, and L. M. Ahmad, "Synthesis, characterization and study the photodecolorization of Schiff base Fe (III) complex in $\text{ZnO}/\text{Uv-A}$ light system," in *AIP Conference Proceedings*, AIP Publishing LLC, 2020, p. 30032.
- [7] F. Ghanbari and M. Moradi, "Application of peroxymonosulfate and its activation methods for degradation of environmental organic pollutants," *Chem. Eng. J.*, vol. 310, pp. 41–62, 2017.
- [8] Li, X., Xia, J., Zhu, W., Di, J., Wang, B., Yin, S., ... & Li, H. (2016). Facile synthesis of few-layered MoS_2 modified BiOI with enhanced visible-light photocatalytic activity. *Colloids and Surfaces A*:

- Physicochemical and Engineering Aspects*, 511, 1-7.
- [9] Zhang, S., Gu, P., Ma, R., Luo, C., Wen, T., Zhao, G., ... & Wang, X. (2019). Recent developments in fabrication and structure regulation of visible-light-driven g-C₃N₄-based photocatalysts towards water purification: a critical review. *Catalysis Today*, 335, 65-77.
- [10] Jiang, L., Yuan, X., Zeng, G., Wu, Z., Liang, J., Chen, X., ... & Wang, H. (2018). Metal-free efficient photocatalyst for stable visible-light photocatalytic degradation of refractory pollutant. *Applied Catalysis B: Environmental*, 221, 715-725.
- [11] S. Choudhury, J. Baeg, N. Park, and R. K. Yadav, "A photocatalyst/enzyme couple that uses solar energy in the asymmetric reduction of acetophenones," *Angew. Chemie Int. Ed.*, vol. 51, no. 46, pp. 11624–11628, 2012.
- [12] Zhao, Y., Zhang, X., Wang, C., Zhao, Y., Zhou, H., Li, J., & Jin, H. (2017). The synthesis of hierarchical nanostructured MoS₂/Graphene composites with enhanced visible-light photo-degradation property. *Applied Surface Science*, 412, 207-213.
- [13] N. Khalifaoui, H. Boutoumi, H. Khalaf, N. Oturan, and M. A Oturan, "Electrochemical oxidation of the xanthene dye Rhodamine 6G by electrochemical advanced oxidation using Pt and BDD anodes," *Curr. Org. Chem.*, vol. 16, no. 18, pp. 2083–2090, 2012.
- [14] Z. S. Seddigi, "Removal of alizarin yellow dye from water using zinc doped WO₃ catalyst," *Bull. Environ. Contam. Toxicol.*, vol. 84, pp. 564–567, 2010.
- [15] M. A. Gondal, M. N. Sayeed, and Z. Seddigi, "Laser enhanced photocatalytic removal of phenol from water using p-type NiO semiconductor catalyst," *J. Hazard. Mater.*, vol. 155, no. 1–2, pp. 83–89, 2008.
- [16] M. A. Rauf and S. S. Ashraf, "Radiation induced degradation of dyes—an overview," *J. Hazard. Mater.*, vol. 166, no. 1, pp. 6–16, 2009.

- [17] L. M. Ahmed, "Bulk and nanocatalysts applications in Advanced Oxidation Processes," in *Oxidoreductase*, IntechOpen, 2020.
- [18] Ullah, S., Noman, M., Ali, K. S., Siddique, M., Sahak, K., Hashmi, S. K., ... & Khan, F. (2021). Treatment of Industrial Wastewater (IWW) and Reuse through Advanced Oxidation Processes (AOPs): A Comprehensive Overview. *IOSR Journal of Environmental Science, Toxicology and Food Technology*, 15(1), 04-14.
- [19] A. K. Biń and S. Sobera-Madej, "Comparison of the advanced oxidation processes (UV, UV/H₂O₂ and O₃) for the removal of antibiotic substances during wastewater treatment," *Ozone Sci. Eng.*, vol. 34, no. 2, pp. 136–139, 2012.
- [20] B. Ning, N. Graham, Y. Zhang, M. Nakonechny, and M. Gamal El-Din, "Degradation of endocrine disrupting chemicals by ozone/AOPs," *Ozone Sci. Eng.*, vol. 29, no. 3, pp. 153–176, 2007.
- [21] I. Oller, S. Malato, and Ja. Sánchez-Pérez, "Combination of advanced oxidation processes and biological treatments for wastewater decontamination—a review," *Sci. Total Environ.*, vol. 409, no. 20, pp. 4141–4166, 2011.
- [22] L. M. A. Al Rihaymee, "Enhanced Photocatalytic Activity of Titanium Dioxide Nanoparticles by Metal Deposition," *Univ. Babylon-College Sci.*, 2013.
- [23] Youssef, L., Roualdes, S., Bassil, J., Zakhour, M., Rouessac, V., Lamy, C., & Nakhl, M. (2019). Effect of plasma power on the semiconducting behavior of low-frequency PECVD TiO₂ and nitrogen-doped TiO₂ anodic thin coatings: photo-electrochemical studies in a single compartment cell for hydrogen generation by solar water splitting. *Journal of Applied Electrochemistry*, 49, 135-150.
- [24] Z. H. Jabbar and S. E. Ebrahim, "Recent advances in nano-semiconductors photocatalysis for degrading organic contaminants and

- microbial disinfection in wastewater: A comprehensive review,” *Environ. Nanotechnology, Monit. Manag.*, vol. 17, p. 100666, 2022.
- [25] T. Van Gerven, G. Mul, J. Moulijn, and A. Stankiewicz, “A review of intensification of photocatalytic processes,” *Chem. Eng. Process. Process Intensif.*, vol. 46, no. 9, pp. 781–789, 2007.
- [26] Y. Liang, H. Wang, H. Sanchez Casalongue, Z. Chen, and H. Dai, “TiO₂ nanocrystals grown on graphene as advanced photocatalytic hybrid materials. *Nano Res.* 3 (10): 701-705.” 2010.
- [27] S. Anandan, N. Ohashi, and M. Miyauchi, “ZnO-based visible-light photocatalyst: Band-gap engineering and multi-electron reduction by co-catalyst,” *Appl. Catal. B Environ.*, vol. 100, no. 3–4, pp. 502–509, 2010.
- [28] A. S. Patil, A. V Patil, C. G. Dighavkar, V. A. Adole, and U. J. Tupe, “Synthesis techniques and applications of rare earth metal oxides semiconductors: A review,” *Chem. Phys. Lett.*, p. 139555, 2022.
- [29] O. M. Darwesh, M. S. Mahmoud, K. M. Barakat, A. Abuellil, and M. S. Ahmad, “Improving the bioremediation technology of contaminated wastewater using biosurfactants produced by novel bacillus isolates,” *Heliyon*, vol. 7, no. 12, p. e08616, 2021.
- [30] S. H. Ammar, A. I. Elaibi, and I. S. Mohammed, “Core/shell Fe₃O₄@ Al₂O₃-PMo magnetic nanocatalyst for photocatalytic degradation of organic pollutants in an internal loop airlift reactor,” *J. Water Process Eng.*, vol. 37, p. 101240, 2020.
- [31] M. D. Hernández-Alonso, F. Fresno, S. Suárez, and J. M. Coronado, “Development of alternative photocatalysts to TiO₂: challenges and opportunities,” *Energy Environ. Sci.*, vol. 2, no. 12, pp. 1231–1257, 2009.
- [32] G. Liu, L. Wang, H. G. Yang, H.-M. Cheng, and G. Q. M. Lu, “Titania-based photocatalysts—crystal growth, doping and heterostructuring,” *J. Mater. Chem.*, vol. 20, no. 5, pp. 831–843, 2010.
- [33] L. Tian, X. Guan, S. Zong, A. Dai, and J. Qu, “Cocatalysts for

- Photocatalytic Overall Water Splitting: A Mini Review,” *Catalysts*, vol. 13, no. 2, p. 355, 2023.
- [34] S. K. Jesudoss *et al.*, “Studies on the efficient dual performance of $Mn_{1-x}Ni_xFe_2O_4$ spinel nanoparticles in photodegradation and antibacterial activity,” *J. Photochem. Photobiol. B Biol.*, vol. 165, pp. 121–132, 2016, doi: <https://doi.org/10.1016/j.jphotobiol.2016.10.004>.
- [35] A. R. Chavan, S. B. Somvanshi, P. P. Khirade, and K. M. Jadhav, “Influence of trivalent Cr ion substitution on the physicochemical, optical, electrical, and dielectric properties of sprayed $NiFe_2O_4$ spinel-magnetic thin films,” *RSC Adv.*, vol. 10, no. 42, pp. 25143–25154, 2020.
- [36] P. B. Kharat, S. B. Somvanshi, J. S. Kounsalye, S. S. Deshmukh, P. P. Khirade, and K. M. Jadhav, “Temperature dependent viscosity of cobalt ferrite/ethylene glycol ferrofluids,” in *AIP conference proceedings*, AIP Publishing LLC, 2018, p. 50044.
- [37] H. J. Kardile, S. B. Somvanshi, A. R. Chavan, A. A. Pandit, and K. M. Jadhav, “Effect of Cd^{2+} doping on structural, morphological, optical, magnetic and wettability properties of nickel ferrite thin films,” *Optik (Stuttg.)*, vol. 207, p. 164462, 2020.
- [38] D. Tripathy, A. O. Adeyeye, C. B. Boothroyd, and S. N. Piramanayagam, “Magnetic and transport properties of Co-doped Fe_3O_4 films,” *J. Appl. Phys.*, vol. 101, no. 1, p. 13904, 2007.
- [39] M. Seki, H. Tabata, H. Ohta, K. Inaba, and S. Kobayashi, “Epitaxial thin films of p-type spinel ferrite grown by pulsed laser deposition,” *Appl. Phys. Lett.*, vol. 99, no. 24, p. 242504, 2011.
- [40] P. T. Barton *et al.*, “Structural distortion below the Néel temperature in spinel $GeCo_2O_4$,” *Phys. Rev. B*, vol. 90, no. 6, p. 64105, 2014.
- [41] T. Katayama *et al.*, “P-type conductivity and room-temperature ferrimagnetism in spinel $MoFe_2O_4$ epitaxial thin film,” *Cryst. Growth Des.*, vol. 19, no. 2, pp. 902–906, 2018.

- [42] S. A. Jadhav, S. B. Somvanshi, M. V Khedkar, S. R. Patade, and K. M. Jadhav, "Magneto-structural and photocatalytic behavior of mixed Ni–Zn nano-spinel ferrites: visible light-enabled active photodegradation of rhodamine B," *J. Mater. Sci. Mater. Electron.*, vol. 31, pp. 11352–11365, 2020.
- [43] S. R. Patade, D. D. Andhare, S. B. Somvanshi, P. B. Kharat, and K. M. Jadhav, "Effect of zinc doping on water-based manganese ferrite nanofluids for magnetic hyperthermia application," in *AIP Conference Proceedings*, AIP Publishing LLC, 2020, p. 30557.
- [44] S. S. Rathore, M. M. Salve, and V. V Dabhade, "Effect of molybdenum addition on the mechanical properties of sinter-forged Fe–Cu–C alloys," *J. Alloys Compd.*, vol. 649, pp. 988–995, 2015.
- [45] M. Monnot, V. Roche, R. Estevez, M. Mantel, and R. P. Nogueira, "Molybdenum effect on the sulfide stress corrosion of a super martensitic stainless steel in sour environment highlighted by electrochemical impedance spectroscopy," *Electrochim. Acta*, vol. 252, pp. 58–66, 2017.
- [46] A. A. Ismail, S. Z. Alsheheri, S. M. Albukhari, and M. H. H. Mahmoud, "Facile synthesis of visible-light-induced mesoporous $\text{Ag}_2\text{O}/\text{Fe}_2(\text{MoO}_4)_3$ photocatalysts for degradation of tetracycline," *Opt. Mater. (Amst.)*, vol. 121, p. 111505, 2021.
- [47] X. Liu, T. Zhu, Q. Lv, Y. Li, and D. Che, "Simultaneous removal of NO_x and SO_2 from coal-fired flue gas based on the catalytic decomposition of H_2O_2 over $\text{Fe}_2(\text{MoO}_4)_3$," *Chem. Eng. J.*, vol. 371, pp. 486–499, 2019.
- [48] A. Muzaffar and M. B. Ahamed, "Iron molybdate and manganese dioxide microrods as a hybrid structure for high-performance supercapacitor applications," *Ceram. Int.*, vol. 45, no. 3, pp. 4009–4015, 2019.
- [49] L. Chen, W. Yang, Y. Wang, Z. Liang, Q. Zhao, and Q. Lu, "Investigation on the NO removal from simulated flue gas by using H_2O_2 vapor over $\text{Fe}_2(\text{MoO}_4)_3$," *Energy & Fuels*, vol. 32, no. 8, pp. 8605–8613, 2018.

- [50] Ahmad, M. Z., Bhatti, I. A., Qureshi, K., Ahmad, N., Nisar, J., Zuber, M., ... & Iqbal, M. (2020). Graphene oxide supported $\text{Fe}_2(\text{MoO}_4)_3$ nano rods assembled round-ball fabrication via hydrothermal route and photocatalytic degradation of nonsteroidal anti-inflammatory drug. *Journal of Molecular Liquids*, 301, 112343.
- [51] F. Jiao and P. G. Bruce, “Two-and three-dimensional mesoporous iron oxides with microporous walls,” *Angew. Chemie*, vol. 116, no. 44, pp. 6084–6087, 2004.
- [52] J. Miao, T. Ren, L. Dong, J. Zhu, and H. Chen, “Double-Template Synthesis of CdS Nanotubes with Strong Electrogenenerated Chemiluminescence,” *Small*, vol. 1, no. 8-9, pp. 802–805, 2005.
- [53] W. T. A. Harrison, “Crystal structures of paraelastic aluminum molybdate and ferric molybdate, $\beta\text{-Al}_2(\text{MoO}_4)_3$ and $\beta\text{-Fe}_2(\text{MoO}_4)_3$,” *Mater. Res. Bull.*, vol. 30, no. 11, pp. 1325–1331, 1995.
- [54] H. Chen, “The crystal structure and twinning behavior of ferric molybdate, $\text{Fe}_2(\text{MoO}_4)_3$,” *Mater. Res. Bull.*, vol. 14, no. 12, pp. 1583–1590, 1979.
- [55] G. Giester, D. Talla, and M. Wildner, “Contributions to the stereochemistry of zirconium oxysalts—part III: syntheses and crystal structures of $\text{M}^{2+} \text{Zr}(\text{SO}_4)_3$ with $\text{M} = \text{Mg}, \text{Mn}, \text{Co}, \text{Ni}, \text{Zn}$ and Cd , and a note on $(\text{Fe}^{3+}, ^{2+}, \text{Zr}) 2(\text{SO}_4)_3$ and $\text{Fe}_2(\text{SO}_4)_3$,” *Monatshefte für Chemie-Chemical Mon.*, vol. 150, pp. 1877–1892, 2019.
- [56] Z. Wang, C. Li, and K. Domen, “Recent developments in heterogeneous photocatalysts for solar-driven overall water splitting,” *Chem. Soc. Rev.*, vol. 48, no. 7, pp. 2109–2125, 2019.
- [57] J. Li, Y. Pan, C. Xiang, Q. Ge, and J. Guo, “Low temperature synthesis of ultrafine $\alpha\text{-Al}_2\text{O}_3$ powder by a simple aqueous sol–gel process,” *Ceram. Int.*, vol. 32, no. 5, pp. 587–591, 2006.
- [58] Y. K. Park, E. H. Tadd, M. Zubris, and R. Tannenbaum, “Size-controlled

- synthesis of alumina nanoparticles from aluminum alkoxides,” *Mater. Res. Bull.*, vol. 40, no. 9, pp. 1506–1512, 2005.
- [59] B. Shin, J. R. Weber, R. D. Long, P. K. Hurley, C. G. Van de Walle, and P. C. McIntyre, “Origin and passivation of fixed charge in atomic layer deposited aluminum oxide gate insulators on chemically treated InGaAs substrates,” *Appl. Phys. Lett.*, vol. 96, no. 15, p. 152908, 2010.
- [60] W. M. Mullins and B. L. Averbach, “The electronic structure of anodized and etched aluminum alloy surfaces,” *Surf. Sci.*, vol. 206, no. 1–2, pp. 52–60, 1988.
- [61] I. Levin and D. Brandon, “Metastable alumina polymorphs: crystal structures and transition sequences,” *J. Am. Ceram. Soc.*, vol. 81, no. 8, pp. 1995–2012, 1998.
- [62] E. Husson and Y. Repelin, “Structural studies of transition aluminas. Theta alumina,” *Eur. J. solid state Inorg. Chem.*, vol. 33, no. 11, pp. 1223–1231, 1996.
- [63] B. Xu, H. Stokes, and J. Dong, “First-principles calculation of kinetic barriers and metastability for the corundum-to-Rh₂O₃ (II) transition in Al₂O₃,” *J. Phys. Condens. Matter*, vol. 22, no. 31, p. 315403, 2010.
- [64] Zhang, N., Wang, L., Wang, H., Cao, R., Wang, J., Bai, F., & Fan, H. (2018). Self-assembled one-dimensional porphyrin nanostructures with enhanced photocatalytic hydrogen generation. *Nano letters*, 18(1), 560-566.
- [65] H. Li, Y. Sun, Z. Yuan, Y. Zhu, and T. Ma, “Titanium phosphonate based metal–organic frameworks with hierarchical porosity for enhanced photocatalytic hydrogen evolution,” *Angew. Chemie Int. Ed.*, vol. 57, no. 12, pp. 3222–3227, 2018.
- [66] M. S. Bakshi, “How surfactants control crystal growth of nanomaterials,” *Cryst. Growth Des.*, vol. 16, no. 2, pp. 1104–1133, 2016.
- [67] P. V Ananthapadmanabhan, K. P. Sreekumar, N. Venkatramani, P. K.

- Sinha, and P. R. Taylor, "Characterization of plasma-synthesized alumina," *J. Alloys Compd.*, vol. 244, no. 1–2, pp. 70–74, 1996.
- [68] Xu, X., Gao, Z., Cui, Z., Liang, Y., Li, Z., Zhu, S., ... & Ma, J. (2016). Synthesis of Cu₂O octadecahedron/TiO₂ quantum dot heterojunctions with high visible light photocatalytic activity and high stability. *ACS applied materials & interfaces*, 8(1), 91-101.
- [69] K. Zinovjev and I. Tuñón, "Reaction coordinates and transition states in enzymatic catalysis," *Wiley Interdiscip. Rev. Comput. Mol. Sci.*, vol. 8, no. 1, p. e1329, 2018.
- [70] Cheng, M., Zeng, G., Huang, D., Yang, C., Lai, C., Zhang, C., & Liu, Y. (2018). Tween 80 surfactant-enhanced bioremediation: toward a solution to the soil contamination by hydrophobic organic compounds. *Critical reviews in biotechnology*, 38(1), 17-30.
- [71] Liang, Q., Liu, X., Zeng, G., Liu, Z., Tang, L., Shao, B., ... & Gong, S. (2019). Surfactant-assisted synthesis of photocatalysts: Mechanism, synthesis, recent advances and environmental application. *Chemical engineering journal*, 372, 429-451.
- [72] A. Wołowicz and K. Staszak, "Study of surface properties of aqueous solutions of sodium dodecyl sulfate in the presence of hydrochloric acid and heavy metal ions," *J. Mol. Liq.*, vol. 299, p. 112170, 2020.
- [73] Yadav, V. K., Khan, S. H., Choudhary, N., Tirth, V., Kumar, P., Ravi, R. K., ... & Godha, M. (2022). Nanobioremediation: A sustainable approach towards the degradation of sodium dodecyl sulfate in the environment and simulated conditions. *Journal of Basic Microbiology*, 62(3-4), 348-360.
- [74] U. Farooq, A. Ali, R. Patel, and N. A. Malik, "Self-aggregation of ionic liquid-cationic surfactant mixed micelles in water and in diethylene glycol–water mixtures: Conductometric, tensiometric, and spectroscopic studies," *J. Mol. Liq.*, vol. 234, pp. 452–462, 2017.
- [75] M. C. D. Ngaha, L. G. Djemmo, E. Njanja, and I. T. Kenfack,

- “Biosorption isotherms and kinetics studies for the removal of 2, 6-dichlorophenolindophenol using palm tree trunk (*Elaeis guineensis*),” *J. Encapsulation Adsorpt. Sci.*, vol. 8, no. 3, pp. 156–177, 2018.
- [76] H. A. Hamad, W. A. Sadik, M. M. Abd El-latif, A. B. Kashyout, and M. Y. Feteha, “Photocatalytic parameters and kinetic study for degradation of dichlorophenol-indophenol (DCPIP) dye using highly active mesoporous TiO₂ nanoparticles,” *J. Environ. Sci.*, vol. 43, pp. 26–39, 2016.
- [77] U. A. Guler, M. Ersan, E. Tuncel, and F. Dügenci, “Mono and simultaneous removal of crystal violet and safranin dyes from aqueous solutions by HDTMA-modified *Spirulina* sp.,” *Process Saf. Environ. Prot.*, vol. 99, pp. 194–206, 2016.
- [78] Punzi, M., Nilsson, F., Anbalagan, A., Svensson, B. M., Jönsson, K., Mattiasson, B., & Jonstrup, M. (2015). Combined anaerobic–ozonation process for treatment of textile wastewater: removal of acute toxicity and mutagenicity. *Journal of hazardous materials*, 292, 52-60.
- [79] C. J. Cooksey, “Quirks of dye nomenclature. 10. Eosin Y and its close relatives,” *Biotech. Histochem.*, vol. 93, no. 3, pp. 211–219, 2018.
- [80] M. Clark, *Handbook of textile and industrial dyeing: principles, processes and types of dyes*. Elsevier, 2011.
- [81] N. I. Kherada, W. Gonzalez, and C. Rosendorff, “Diuretics,” in *Side Effects of Drugs Annual*, Elsevier, 2014, pp. 289–296.
- [82] D. Li and S. Liu, *Water quality monitoring and management: Basis, technology and case studies*. Academic Press, 2018.
- [83] R. Manurung, “Perombakan Zat Warna Azo Reaktif Secara Anaerob? Aerob,” 2004.
- [84] A. N. Babu, D. S. Reddy, P. Sharma, G. S. Kumar, K. Ravindhranath, and G. V. K. Mohan, “Removal of hazardous indigo carmine dye from waste water using treated red mud,” *Mater. Today Proc.*, vol. 17, pp. 198–208, 2019.

- [85] N. Y. Donkadokula, A. K. Kola, I. Naz, and D. Saroj, "A review on advanced physico-chemical and biological textile dye wastewater treatment techniques," *Rev. Environ. Sci. bio/technology*, vol. 19, pp. 543–560, 2020.
- [86] Nindjio, G. F. K., Tagne, R. F. T., Jiokeng, S. L. Z., Fotsop, C. G., Bopda, A., Doungmo, G., ... & Tonle, I. K. (2022). Lignocellulosic-based materials from bean and pistachio pod wastes for dye-contaminated water treatment: optimization and modeling of indigo carmine sorption. *Polymers*, 14(18), 3776.
- [87] B. Jones, J. Britton, D. Mafukidze, and T. Nyokong, "Photodegradation of 4-chlorophenol using Zn and In phthalocyanines substituted with pyrrole without hetero atoms linkers and supported on polyacrylonitrile electrospun fibres," *Polyhedron*, vol. 178, p. 114329, 2020.
- [88] G. Chen, F. Liu, Y. Qiao, and B. Tao, "Photodegradation of tefuryltrione in water under UV irradiation: Identification of transformation products and elucidation of photodegradation pathway," *Chemosphere*, vol. 227, pp. 133–141, 2019.
- [89] S. M. T. H. Moghaddas, B. Elahi, and V. Javanbakht, "Biosynthesis of pure zinc oxide nanoparticles using Quince seed mucilage for photocatalytic dye degradation," *J. Alloys Compd.*, vol. 821, p. 153519, 2020.
- [90] M. H. H. Ali, K. M. Al-Qahtani, and S. M. El-Sayed, "Enhancing photodegradation of 2, 4, 6 trichlorophenol and organic pollutants in industrial effluents using nanocomposite of TiO₂ doped with reduced graphene oxide," *Egypt. J. Aquat. Res.*, vol. 45, no. 4, pp. 321–328, 2019.
- [91] H. Lin, K. Pang, Y. Ma, and J. Hu, "Photodegradation of fluazaindolizine in water under simulated sunlight irradiation: Identification of transformation products and elucidation of transformation mechanism," *Chemosphere*, vol. 214, pp. 543–552, 2019.

- [92] K. I. Predick, S. R. Archer, S. M. Aguilon, D. A. Keller, H. L. Throop, and P. W. Barnes, "UV-B radiation and shrub canopy effects on surface litter decomposition in a shrub-invaded dry grassland," *J. Arid Environ.*, vol. 157, pp. 13–21, 2018.
- [93] H. Bekakria, H. Bendjeffal, A. Djebli, H. Mamine, T. Metidji, and Z. Benrdjem, "Heterogeneous sono-photo-Fenton degradation of methyl violet 10B using $\text{Fe}_2\text{O}_3\text{-Al}_2\text{O}_3\text{-Ga}_2\text{O}_3$ as a new photocatalyst," *Inorg. Nano-Metal Chem.*, vol. 51, no. 12, pp. 1759–1774, 2021.
- [94] M. F. Chowdhury, S. Khandaker, F. Sarker, A. Islam, M. T. Rahman, and M. R. Awual, "Current treatment technologies and mechanisms for removal of indigo carmine dyes from wastewater: A review," *J. Mol. Liq.*, vol. 318, p. 114061, 2020.
- [95] Li, J., Wang, L., Liu, H., Zhao, J., Li, X., Wei, H., & Han, Y. (2017). Synthesis and enhanced toluene gas sensing properties of 1-D $\alpha\text{-MoO}_3/\text{Fe}_2(\text{MoO}_4)_3$ heterostructure. *Journal of Alloys and Compounds*, 694, 939-945.
- [96] S. Zou, J. Luo, Z. Lin, P. Fu, and Z. Chen, "Acetone gas sensor based on iron molybdate nanoparticles prepared by hydrothermal method with PVP as surfactant," *Mater. Res. Express*, vol. 5, no. 12, p. 125013, 2018.
- [97] P. Santhoshkumar *et al.*, "Bifunctional iron molybdate as highly effective heterogeneous electro-Fenton catalyst and Li-ion battery anode," *Chemosphere*, vol. 286, p. 131846, 2022.
- [98] S. Thulasi, V. Arunprasad, P. S. Karthik, G. Elatharasan, P. Senthil, and A. T. Rajamanickam, "Design and fabrication of high performance photoanode of $\text{Fe}_2(\text{MoO}_4)_3/\text{RGO}$ hybrid composites for triiodide reduction in dye-sensitized solar cells," *J. Clust. Sci.*, vol. 34, no. 1, pp. 349–357, 2023.
- [99] L. Chang, X. Xie, X. Zhang, H. Chai, and Y. Huang, "Overlooked key role of Mo(VI) in $\text{Fe}_2(\text{MoO}_4)_3$ for peroxymonosulfate activation with 1O_2

- dominated degradation pathway,” *Sep. Purif. Technol.*, p. 124360, 2023.
- [100] B. Ohtani, “Photocatalysis A to Z—What we know and what we do not know in a scientific sense,” *J. Photochem. Photobiol. C Photochem. Rev.*, vol. 11, no. 4, pp. 157–178, 2010.
- [101] A. Obaid and L. Ahmed, “One-step hydrothermal synthesis of α - MoO_3 nano-belts with ultrasonic assist for incorporating TiO_2 as a nanocomposite,” *Egypt. J. Chem.*, vol. 64, no. 10, pp. 5725–5734, 2021.
- [102] A. A. Abd Zaid, L. M. Ahmed, and R. K. Mohammad, “Synthesis of Inverse Spinel Nickel Ferrite Like-Broccoli Nanoparticle and Thermodynamic Study of Photo-decolorization of Alkali Blue 4B dye,” *J. Nanostructures*, vol. 12, no. 3, pp. 697–710, 2022.
- [103] T. M. Jawad and L. M. Ahmed, “Direct ultrasonic synthesis of WO_3/TiO_2 nanocomposites and applying them in the photo decolorization of eosin yellow dye,” *Period. Tche Quim.*, vol. 17, no. 34, pp. 621–633, 2020.
- [104] M. K. Hayawi, L. M. Ahmed, and M. M. Kareem, “Synthesis of spinel Mn_3O_4 and spinel $\text{Mn}_3\text{O}_4/\text{ZrO}_2$ nanocomposites and using them in photocatalytic decolorization of Fe (II)-(4, 5-diazafluoren-9-one 11) complex,” *Period. Tche Quim.*, vol. 17, no. 34, pp. 689–699, 2020.
- [105] F. Tsegaye, A. M. Taddesse, E. Teju, and M. Aschalew, “Preparation and sorption property study of $\text{Fe}_3\text{O}_4/\text{Al}_2\text{O}_3/\text{ZrO}_2$ composite for the removal of cadmium, lead and chromium ions from aqueous solutions,” *Bull. Chem. Soc. Ethiop.*, vol. 34, no. 1, pp. 105–121, 2020.
- [106] S. Ahmed, “Photo electrochemical study of ferrioxalate actinometry at a glassy carbon electrode,” *J. Photochem. Photobiol. A Chem.*, vol. 161, no. 2–3, pp. 151–154, 2004.
- [107] M. Montalti, A. Credi, L. Prodi, and M. T. Gandolfi, *Handbook of photochemistry*. CRC press, 2006.
- [108] A. W. Adamson, A. Vogler, H. Kunkely, and R. Wachter, “Photocalorimetry. Enthalpies of photolysis of trans-azobenzene,

- ferrioxalate and cobaltioxalate ions, chromium hexacarbonyl, and dirhenium decarbonyl,” *J. Am. Chem. Soc.*, vol. 100, no. 4, pp. 1298–1300, 1978.
- [109] S. I. Zuafuani and L. M. Ahmed, “Photocatalytic decolourization of direct orange Dye by zinc oxide under UV irradiation,” *Int. J. Chem. Sci.*, vol. 13, no. 1, pp. 187–196, 2015.
- [110] M. A. Tabbara and M. M. El Jamal, “A KINETIC STUDY OF THE DISCLOLORATION OF METHYLENE BLUE BY Na_2SO_3 , COMPARISON WITH NaOH ,” *J. Univ. Chem. Technol. Metall.*, vol. 47, no. 3, 2012.
- [111] P. Atkins, “Paula J. Atkins’ physical chemistry.” Oxford university press, 2006.
- [112] A. Talaiekhosani, S. Rezania, K.-H. Kim, R. Sanaye, and A. M. Amani, “Recent advances in photocatalytic removal of organic and inorganic pollutants in air,” *J. Clean. Prod.*, vol. 278, p. 123895, 2021.
- [113] Wang, L., Deng, J., Jiang, M., Zhen, C., Li, F., Li, S., ... & Zhu, W. (2023). Arene–perfluoroarene interactions in molecular cocrystals for enhanced photocatalytic activity. *Journal of Materials Chemistry A*, 11(21), 11235-11244.
- [114] M. Kamran, M. A. Morsy, T. A. Kandiel, and W. Iali, “Semi-automated EPR system for direct monitoring the photocatalytic activity of TiO_2 suspension using TEMPOL model compound,” *Photochem. Photobiol. Sci.*, vol. 21, no. 12, pp. 2071–2083, 2022.
- [115] L. Ahmed, “Advanced Oxidation Processes for Carmoisine (E122) Dye in UVA/ ZnO System: Influencing PH, Temperature and Oxidant Agents on Dye Solution,” *J. Glob. Pharma Technol.*, vol. 10, pp. 248–254, Sep. 2018.
- [116] A. K. Sharma and B.-K. Lee, “Surfactant-aided sol-gel synthesis of TiO_2 – MgO nanocomposite and their photocatalytic azo dye degradation

- activity,” *J. Compos. Mater.*, vol. 54, no. 12, pp. 1561–1570, 2020.
- [117] Qiu, Y., Yang, C., Zhou, H., Zang, J., Fan, Y., Dang, F., ... & Wang, W. (2022). Enriched Surface Oxygen Vacancies of $\text{Fe}_2(\text{MoO}_4)_3$ Catalysts for a PDS-Activated photoFenton System. *Molecules*, 28(1), 333.
- [118] M. M. Rashad, D. A. Rayan, and A. A. Ramadan, “Optical and magnetic properties of $\text{CuO}/\text{CuFe}_2\text{O}_4$ nanocomposites,” *J. Mater. Sci. Mater. Electron.*, vol. 24, pp. 2742–2749, 2013.
- [119] M. M. Rashad, A. A. Ibrahim, D. A. Rayan, M. M. S. Sanad, and I. M. Helmy, “Photo-Fenton-like degradation of Rhodamine B dye from waste water using iron molybdate catalyst under visible light irradiation,” *Environ. nanotechnology, Monit. Manag.*, vol. 8, pp. 175–186, 2017.
- [120] R. Prabhakar and S. R. Samadder, “Low cost and easy synthesis of aluminium oxide nanoparticles for arsenite removal from groundwater: a complete batch study,” *J. Mol. Liq.*, vol. 250, pp. 192–201, 2018.
- [121] R. Romero Toledo, V. Ruíz Santoyo, D. Moncada Sánchez, and M. Martínez Rosales, “Effect of aluminum precursor on physicochemical properties of Al_2O_3 by hydrolysis/precipitation method,” *Nov. Sci.*, vol. 10, no. 20, pp. 83–99, 2018.
- [122] B. Wang, R. Yan, D. H. Lee, Y. Zheng, H. Zhao, and C. Zheng, “Characterization and evaluation of $\text{Fe}_2\text{O}_3/\text{Al}_2\text{O}_3$ oxygen carrier prepared by sol–gel combustion synthesis,” *J. Anal. Appl. Pyrolysis*, vol. 91, no. 1, pp. 105–113, 2011.
- [123] K. Seevakan, A. Manikandan, P. Devendran, S. A. Antony, and T. Alagesan, “One-pot synthesis and characterization studies of iron molybdenum mixed metal oxide ($\text{Fe}_2(\text{MoO}_4)_3$) nano-photocatalysts,” *Adv. Sci. Eng. Med.*, vol. 8, no. 7, pp. 566–572, 2016.
- [124] F. Al-Mokdad, R. S. Hassan, and R. Awad, “Physical and dielectric properties of MnFe_2O_4 doped by Mo,” *Curr. Nanomater.*, vol. 4, no. 2, pp. 125–136, 2019.

- [125] A. Ghorbani-Choghamarani, M. Mohammadi, L. Shiri, and Z. Taherinia, “Synthesis and characterization of spinel FeAl_2O_4 (hercynite) magnetic nanoparticles and their application in multicomponent reactions,” *Res. Chem. Intermed.*, vol. 45, pp. 5705–5723, 2019.
- [126] Casillas, J. E., Campa-Molina, J., Tzompantzi, F., Carbajal Arízaga, G. G., López-Gaona, A., Ulloa-Godínez, S., ... & Barrera, A. (2020). Photocatalytic degradation of diclofenac using $\text{Al}_2\text{O}_3\text{-Nd}_2\text{O}_3$ binary oxides prepared by the sol-gel method. *Materials*, 13(6), 1345.
- [127] S. Ali, M. Ali, and L. Ahmed, “Hybrid Phosphotungstic acid-Dopamine (PTA-DA) Like-flower Nanostructure Synthesis as a Furosemide Drug Delivery System and Kinetic Study of Drug Releasing,” *Egypt. J. Chem.*, vol. 64, no. 10, pp. 5547–5553, 2021.
- [128] B. Hasan Taresh, F. Hadi Fakhri, and L. M Ahmed, “Synthesis and Characterization of CuO/CeO_2 Nanocomposites and Investigation Their Photocatalytic Activity,” *J. Nanostructures*, vol. 12, no. 3, pp. 563–570, 2022.
- [129] S. Tamilarasi, K. Balakrishnan, I. Muthuvel, T. Rajachandrasekar, K. Gowthami, and G. Thirunarayanan, “HIGHLY SOLAR ACTIVE $\text{Fe}_2(\text{MoO}_4)_3$ NANOCATALYST ASSISTED DEGRADATION OF RHODAMINE-B DYE,” *J. Adv. Sci. Res.*, vol. 11, no. 02, pp. 93–100, 2020.
- [130] S. Parveen *et al.*, “Synthesis, characterization and photocatalytic performance of iron molybdate ($\text{Fe}_2(\text{MoO}_4)_3$) for the degradation of endosulfan pesticide,” *Mater. Res. Express*, vol. 7, no. 3, p. 35016, 2020.
- [131] A. G. Kharaji, A. Shariati, and M. A. Takassi, “A novel γ -alumina supported Fe-Mo bimetallic catalyst for reverse water gas shift reaction,” *Chinese J. Chem. Eng.*, vol. 21, no. 9, pp. 1007–1014, 2013.
- [132] S. M. H. Ali, M. M. M. A. Alali, and L. M. Ahmed, “Flower-like hierarchical nanostructures synthesis of polyoxometalate-dopamine and

- loading furosemide on its surface and aging them using microwave technique,” in *AIP Conference Proceedings*, AIP Publishing LLC, 2022, p. 40010.
- [133] G. Hidalgo, M. Tonelli, L. Burel, M. Aouine, and J. M. M. Millet, “Microwave-assisted hydrothermal synthesis, characterization and catalytic performance of $\text{Fe}_2(\text{MoO}_4)_3$ in the selective oxidation of propene,” *Catal. Today*, vol. 363, pp. 36–44, 2021.
- [134] X. Gao, C. Li, Z. Yin, and Y. Chen, “Synthesis and H_2S sensing performance of $\text{MoO}_3/\text{Fe}_2(\text{MoO}_4)_3$ yolk/shell nanostructures,” *RSC Adv.*, vol. 5, no. 47, pp. 37703–37709, 2015.
- [135] T. M. Jawad and L. M. Ahmed, “Synthesis of WO_3/TiO_2 nanocomposites for Use as Photocatalysts for Eosin Yellow Dye Degradation,” in *IOP Conference Series: Materials Science and Engineering*, IOP Publishing, 2021, p. 12153.
- [136] Nisar, J., Hassan, S., Khan, M. I., Iqbal, M., Nazir, A., Sharif, A., & Ahmed, E. (2020). Hetero-structured iron molybdate nanoparticles: synthesis, characterization and photocatalytic application. *International Journal of Chemical Reactor Engineering*, 18(2), 20190123.
- [137] B. K. R. Koteru, B. Praveen Kumar, and G. Govindasamy, “Synthesis, Characterization and Evaluation of Iron-Molybdenum Oxide Catalyst for the Hydrothermal Liquefaction of Wastewater to Bio-oil,” in *Advances in Environment Engineering and Management: Proceedings of the 1st National Conference on Sustainable Management of Environment and Natural Resource Through Innovation in Science and Technology*, Springer, 2021, pp. 165–173.
- [138] T. M. Jawad, M. R AL-Lami, A. S. Hasan, J. A. Al-Hilifi, R. K. Mohammad, and L. Ahmed, “Synergistic Effect of dark and photoreactions on the removal and photo-decolorization of azo carmosine dye (E122) as food dye using Rutile- TiO_2 suspension,” *Egypt. J. Chem.*,

- vol. 64, no. 9, pp. 4857–4865, 2021.
- [139] F. H. Fakhri and L. M. Ahmed, “Incorporation CdS with ZnS as composite and using in photo-decolorization of congo red dye,” *Indones. J. Chem.*, vol. 19, no. 4, pp. 936–943, 2019.
- [140] T. E. Agustina, M. Faizal, and P. L. Hariani, “Synthesis and Characterization of ZnO/MnFe₂O₄ Nanocomposites for Degrading Cationic Dyes,” *J. Ecol. Eng.*, vol. 24, no. 4, 2023.
- [141] K. K. Kefeni and B. B. Mamba, “Photocatalytic application of spinel ferrite nanoparticles and nanocomposites in wastewater treatment,” *Sustain. Mater. Technol.*, vol. 23, p. e00140, 2020.
- [142] P. L. Hariani, M. Said, - Salni, N. Aprianti, and Y. A. L. R. Naibaho, “High Efficient Photocatalytic Degradation of Methyl Orange Dye in an Aqueous Solution by CoFe₂O₄-SiO₂-TiO₂ Magnetic Catalyst,” *J. Ecol. Eng.*, vol. 23, no. 1, pp. 118–128, 2021.
- [143] E. Marchenko, G. Baigonakova, K. Dubovikov, O. Kokorev, Y. Yasenchuk, and A. Vorozhtsov, “In Vitro Bio-Testing Comparative Analysis of NiTi Porous Alloys Modified by Heat Treatment,” *Metals (Basel)*, vol. 12, no. 6, p. 1006, 2022.
- [144] I. Prabha and S. Lathasree, “Photocatalytic Degradation of Reactive Red 198 Dye Using Zinc Oxide and Titanium Dioxide Nanocatalysts,” *Asian J. Chem.*, vol. 26, no. 9, 2014.
- [145] A. Mohmoud, S. Rakass, H. Oudghiri Hassani, F. Kooli, M. Abboudi, and S. Ben Aoun, “Iron molybdate Fe₂(MoO₄)₃ nanoparticles: Efficient sorbent for methylene blue dye removal from aqueous solutions,” *Molecules*, vol. 25, no. 21, p. 5100, 2020.
- [146] L. Liu, J. Zhao, S. Wang, B. Zhang, J. Yang, and H. Liu, “Supercritical Hydrothermal Synthesis of Nano-Zirconia: Reaction Path and Crystallization Mechanisms of Different Precursors,” in *E3S Web of Conferences*, EDP Sciences, 2023, p. 1025.

- [147] Yin, C., Li, S., Liu, L., Huang, Q., Zhu, G., Yang, X., & Wang, S. (2022). Structure-tunable trivalent Fe-Al-based bimetallic organic frameworks for arsenic removal from contaminated water. *Journal of Molecular Liquids*, 346, 117101.
- [148] B. Singh, P. Singh, S. Siddiqui, D. Singh, and M. Gupta, "Wastewater treatment using Fe-doped perovskite manganites by photocatalytic degradation of methyl orange, crystal violet and indigo carmine dyes in tungsten bulb/sunlight," *J. Rare Earths*, 2022.
- [149] M. Afkari, S. M. Masoudpanah, M. Hasheminasari, and S. Alamolhoda, "Effects of iron oxide contents on photocatalytic performance of nanocomposites based on g-C₃N₄," *Sci. Rep.*, vol. 13, no. 1, p. 6203, 2023.
- [150] H. Liu, Z. Zhang, Q. Yuan, Y. Zhou, J. Liu, and H. Yang, "New frontiers in heterogeneous Hg⁰ oxidation by O₂ over catalytic single-Fe site on boron-vacancy of h-BN: A density functional theory study," *Fuel*, vol. 333, p. 126335, 2023.
- [151] P. Vasconcelos Borges Pinho *et al.*, "Stoichiometry Driven Tuning of Physical Properties in Epitaxial Fe₃-XcrxO₄ Thin Films," *Available SSRN* 4254706.
- [152] T. K. N. Tran, V. T. Le, T. H. Nguyen, V. D. Doan, Y. Vasseghian, and H. S. Le, "Enhanced adsorption of cationic and anionic dyes using cigarette butt-based adsorbents: Insights into mechanism, kinetics, isotherms, and thermodynamics," *Korean J. Chem. Eng.*, pp. 1–11, 2023.
- [153] A. Nobakht, D. Jafari, and M. Esfandyari, "New Insights on the Adsorption of Phenol Red Dyes from Synthesized Wastewater using Activated Carbon Prepared from the Fe₂(MoO₄)₃-treated Mespilus Germanica Leaves: Equilibrium, Kinetic, and Thermodynamic Studies," 2023.
- [154] S. Fındık, "Decolorization of Direct Black 22 by Photo Fenton like Method Using UV Light and Zeolite Modified Zinc Ferrite: Kinetics and

- Thermodynamics,” *Acta Chim. Slov.*, 2022.
- [155] Zhang, X., Wu, H., Wei, J., Liu, C., Yi, Y., Chen, Z., ... & Zhou, J. Efficient Degradation of Tetracycline Through Peroxymonosulfate Activation by $\text{Fe}_2(\text{MoO}_4)_3$ as Heterogeneous Catalyst. Available at SSRN 4420983.
- [156] A. Nobakht, D. Jafari, and M. Esfandyari, “New insights on the adsorption of phenol red dyes from synthetic wastewater using activated carbon/ $\text{Fe}_2(\text{MoO}_4)_3$,” *Environ. Monit. Assess.*, vol. 195, no.5, p. 574, 2023.
- [157] G. A. Ashraf *et al.*, “Photocatalytic stimulation of peroxymonosulfate by novel $\text{MoO}_3@ \text{ZrO}_2$ with Z-scheme heterojunction for diclofenac sodium degradation,” *J. Water Process Eng.*, vol. 51, p. 103435, 2023.
- [158] L. Megatif, R. Dillert, and D. W. Bahnemann, “Determination of the quantum yield of a heterogeneous photocatalytic reaction employing a black body photoreactor,” *Catal. Today*, vol. 355, pp. 698–703, 2020.
- [159] M. Qureshi and K. Takanebe, “Insights on measuring and reporting heterogeneous photocatalysis: efficiency definitions and setup examples,” *Chem. Mater.*, vol. 29, no. 1, pp. 158–167, 2017.
- [160] L. M. Ahmed, S. I. Saaed, and A. A. Marhoon, “Effect of oxidation agents on photo-decolorization of vitamin B 12 in the presence of ZnO/UV-A system,” *Indones. J. Chem.*, vol. 18, no. 2, pp. 272–278, 2018.
- [161] Z. A. Hussein, S. K. Abbas, and L. M. Ahmed, “UV-A activated ZrO_2 via photodecolorization of methyl green dye,” *IOP Conf. Ser. Mater. Sci. Eng.*, vol. 454, no. 1, p. 12132, 2018, doi: 10.1088/1757-899X/454/1/012132.
- [162] R. A. Putri, S. Safni, N. Jamarun, U. Septiani, M.-K. Kim, and K. Zoh, “Kinetics studies on photodegradation of methyl orange in the presence of C-N-codoped TiO_2 catalyst,” *Egypt. J. Chem.*, vol. 62, no. Special Issue (Part 2) Innovation in Chemistry, pp. 563–575, 2019, doi: 10.21608/ejchem.2019.14543.1883.

- [163] K. H. Kazm and S. T. Najim, “Study Kinetic Reaction and Removal of Indigo Carmine Dye in Aqueous Solutions by Direct Electrochemical Oxidation,” *IOP Conf. Ser. Earth Environ. Sci.*, vol. 1002, no. 1, p. 12005, 2022, doi: 10.1088/1755-1315/1002/1/012005.
- [164] E. Ortiz, V. Gómez-Chávez, C. M. Cortés-Romero, H. Solís, R. Ruiz-Ramos, and S. Loera-Serna, “Degradation of indigo carmine using advanced oxidation processes: Synergy effects and toxicological study,” *J. Environ. Prot. (Irvine, Calif.)*, vol. 7, no. 12, pp. 1693–1706, 2016.
- [165] A. Zaouak, A. Noomen, and H. Jelassi, “Gamma-radiation induced decolorization and degradation on aqueous solutions of Indigo Carmine dye,” *J. Radioanal. Nucl. Chem.*, vol. 317, no. 1, pp. 37–44, 2018.

الخلاصة

يتكون هذا العمل من ثلاثة أجزاء رئيسية: الجزء الأول يوضح تصنيع جسيمات الإسبنيل الموليبدينيوم – أكاسيد الحديد النانوية (MoFe_2O_4) بالطريقة الحرارية المائية باستخدام نوعين من كبريتات دوديسيل الصوديوم (SDS) ذات الفاعلية السطحية الأنيونية والكاتيونية للسيتراميد (CT). كقالب ومثبت. تم تحضير المركبات النانوية الموليبدينيوم-أكاسيد الحديد-الألومينا ($\text{MoFe}_2\text{O}_4/\text{Al}_2\text{O}_3$) من خلال دمج الإسبنيل MoFe_2O_4 مع المخلقه Al_2O_3 بتقنية الموجات فوق الصوتية، وهي تقنية بسيطة وسريعة ومفيدة بيئياً.

يتضمن الجزء الثاني توصيف MoFe_2O_4 المحضر، والمخلقة Al_2O_3 ، ومركبات نانوية، باستخدام تقنيات FT-IR و XRD و SEM-EDX. أظهر أطياف FT-IR مواقع رباعي السطوح وثمانى السطوح للموليبدينيوم والحديد لجميع المحفزات المحضرة. أكد تحليل XRD أن الإسبنيل MoFe_2O_4 والمخلقة Al_2O_3 ومركباته النانوية قد تم تحضيرها بنجاح على أساس أحجام نانوية تبلغ 23.83 نانومتر و 43.44 نانومتر و 47.84 نانومتر في وجود الخافض للتوتر السطحي الأنوني SDS و 23.97 نانومتر و 47.41 نانومتر في وجود الخافض للتوتر السطحي الكاتيونية. ، على التوالي.

أشار تحليل SEM إلى أن شكل الإسبنيل MoFe_2O_4 المحضر في وجود مادة خافضة للتوتر السطحي أنيونية SDS وجد أنه يشبه الكافيار، وأشكال Al_2O_3 و MoFe_2O_4 عبارة عن خلايا دماغية كروية وحبيبات متشابهة، في حين أن الأشكال عبارة عن صفائح نانوية. والجسيمات النانوية المشابهة للفشار في وجود الخافض للتوتر السطحي المقطعي. كما تم إظهار وجود العناصر Fe, Mo, Al, O في العينات المنتجة بواسطة أطياف EDX. توضح فجوات النطاق (Bg) المحددة من معادلة T_{auc} أن جميع المحفزات عبارة عن محفزات ضوئية وأن MoFe_2O_4 بها فجوة نطاق مباشرة، لكن المخلقة Al_2O_3 والمركبات النانوية لها فجوات نطاق غير مباشرة بقيم 2.78 فولت و 4.44 فولت و 4.05 فولت على التوالي. ، وتم العثور على جسيمات الإسبنيل MoFe_2O_4 النانوية في وجود الخافض للتوتر السطحي الكاتيونى ومركباتها النانوية مع الألومينا بـ 2.78 و 4.05 فولت.

تم تحديد الرقم الهيدروجيني لنقطة الشحن الصفري (pH_{pzc}) لجميع العينات التي تم العثور عليها لجميع المحفزات الضوئية في وجود SDS ، ووجد أن الفاعل بالسطح الكاتيونى المحسوب أقل من الرقم الهيدروجيني الأولي. إن العوائد الكمومية (Φ) لإزالة تلويين صبغ IC باستخدام المحفزات الضوئية المدروسة منخفضة.

يركز الجزء الثالث على قدرة وتقييم فعالية Al_2O_3 و $MoFe_2O_4$ ومركباتها النانوية على إزالة تلويين صبغة IC القرمزي النيلي. تم توضيح تأثير العوامل المختلفة على إزالة اللون الضوئي لصبغة IC القرمزي النيلي باستخدام المحفزات الضوئية في وجود SDS ، CT السطحي. درجة الحرارة ودرجة الحموضة الأولية هما اثنان من هذه المعلمات.

تم حساب المعلمات الديناميكية الحرارية باستخدام معادلة Eyring-Polanyi ومعادلة Arrhenius ومعادلة Gibbs مما يثبت أن التفاعل الضوئي هذا هو تفاعل طارد للحرارة وغير عفوي وأقل عشوائية باستخدام Al_2O_3 و $MoFe_2O_4$ والمركبات النانوية في وجود CT- الخافض للتوتر السطحي بينما باستخدام $MoFe_2O_4$ في وجود SDS- الخافض للتوتر السطحي فقط، هو تفاعل ماص للحرارة وغير عفوي وأقل عشوائية.



جامعة كربلاء
كلية العلوم
قسم الكيمياء

**تحضير وتوصيف المترابك النانوي ($\text{MoFe}_2\text{O}_4 / \text{Al}_2\text{O}_3$) كمحفز ضوئي
لتكسير صبغة القرمزي النيلي**

رسالة مقدمة الى

جامعة كربلاء – مجلس كلية العلوم

وهي جزء من متطلبات نيل درجة الماجستير علوم في الكيمياء

تقدم بها

محمد علي حميد

بكالوريوس علوم في الكيمياء (2013) جامعة واسط

إشراف

أ.د. لى مجيد احمد